Microscopic investigation of intrinsic defects in transition metal dichalcogenide monolayers grown by chemical vapour deposition

Senkić, Ana

Doctoral thesis / Disertacija

2024

Degree Grantor / Ustanova koja je dodijelila akademski / stručni stupanj: **University of Rijeka / Sveučilište u Rijeci**

Permanent link / Trajna poveznica: https://urn.nsk.hr/urn:nbn:hr:194:310475

Rights / Prava: In copyright/Zaštićeno autorskim pravom.

Download date / Datum preuzimanja: **2025-03-29**

UNIVERSITY OF RIJEKA

FACULTY OF PHYSICS

Ana Senkić

MICROSCOPIC INVESTIGATION OF INTRINSIC DEFECTS IN TRANSITION METAL DICHALCOGENIDE MONOLAYERS GROWN BY CHEMICAL VAPOUR DEPOSITION

DOCTORAL THESIS

Rijeka, 2023.

UNIVERSITY OF RIJEKA

FACULTY OF PHYSICS

Ana Senkić

MICROSCOPIC INVESTIGATION OF INTRINSIC DEFECTS IN TRANSITION METAL DICHALCOGENIDE MONOLAYERS GROWN BY CHEMICAL VAPOUR DEPOSITION

DOCTORAL THESIS

Supervisors:

dr. sc. Nataša Vujičić

prof. dr. sc. Marin Karuza

Rijeka, 2023.

Mentorica rada: dr. sc. Nataša Vujičić

Komentor rada: prof. dr. sc. Marin Karuza

Doktorski rad obranjen je dana _____ u/na ____

_____, pred povjerenstvom u sastavu:

1. _____

2. _____

3. _____

4. _____

5. _____

To my family and friends: thank you for standing by me and for believing in me.

Abstract

The investigation of two-dimensional (2D) materials has attracted a great interest after the discovery of the one-atom-thick material - graphene, in 2004. Due to its semimetallic nature, graphene is not suitable for easy implementation in the semiconducting industry. On the other hand, layered semiconducting materials, such as monolayer (1L) MoS_2, have been proven to be good candidates for fabrication of various devices. Its bandgap is in the visible part of the electromagnetic spectrum, making it a good candidate for various applications: photovoltaics, solar cells, transistors, etc. The biggest obstacle in the industrialization of 2D materials is reproducible and cheap synthesis which would produce high-quality, large-area samples with small defect concentration. High-quality samples can be fabricated with the mechanical exfoliation technique, but its major drawbacks are that it is not scalable nor reproducible. On the other hand, the chemical vapour deposition (CVD) technique has all the desirable properties, but the optimization of the growth parameters is time-consuming. Not all CVD-grown samples have the same quality, since this is highly dependent on the growth parameters.

The focus of the first part of my Thesis is establishing the optimum growth parameters which yield samples with desirable properties: high-quality, large lateral size MoS_2 monocrystals with small defect concentration. Afterwards, the spatial distribution of intrinsic defects in 1L MoS_2 was determined using various non-invasive microscopic techniques. These results were correlated with the growth parameters and it was shown that the growth temperature (T_G) has a major effect on the defect concentration and type in 1L MoS_2. Even though all samples analysed in Chapter 4 have equilateral triangular shape, their optical and electronic properties differ due to different growth parameters. The final part of my Thesis involves the utilisation of intrinsic defects in 1L MoS_2. By mixing different metallic precursors in the CVD growth process, it is possible to synthesise either alloys or heterostructures. This route of defect-engineering can provide a material with completely new properties, which are not typical for the host material. In Chapter 5 preliminary all-optical analyses of monolayer $Mo_{1-x}W_xS_2$ and complex WS_2/MoS_2 heterostructure are presented.

Keywords: 2D materials, CVD synthesis, MoS_2 crystal quality, defect-engineering, TMD alloys and heterostructures

Prošireni sažetak

Istraživanje dvodimenzionalnih (2D) materijala je doživjelo procvat nakon izoliranja jednog sloja grafita - grafena. Grafen je materijal debljine jednog atoma ugljika, koji ima odličnu vodljivost te čvrstoću. Budući da je grafen polumetal, njegova primjena u poluvodičkoj industriji zahtijeva komplicirane i skupe tehnike modificiranja njegovog energijskog procijepa. S druge strane, slojeviti poluvodički materijali, poput MoS_2, su odlični kandidati za proizvodnju uređaja koji su se dosada temeljili na siliciju. Jednosloj (1L) MoS_2 ima energijski procijep u vidljivom dijelu elektromagnetskog spektra, što ga čini vrlo pogodnim materijalom za proizdvodnju raznih uređaja: solarne ćelije, tranzistore, diode itd. Najveća prepreka u industrijalizaciji 2D materijala je nepostojanje procesa sinteze koji će rezultirati s visokokvalitetnim, monokristalnim uzorcima velike površine i s niskom koncentracijom defekata. Visokokvalitetni uzorci se mogu proizvesti metodom mehaničke eksfolijacije, međutim, najveći nedostatci ove metode su nereproducibilnost i neskalabilnost. S druge strane, tehnika kemijske depozicije para (eng. *chemical vapour deposition* - CVD) ima sva poželjna svojstva te je uz to jeftina tehnika, ali je uspostavljanje idealnih parametara rasta vremenski vrlo zahtjevno. Parametri rasta bitno utječu na svojstva i kvalitetu materijala, kao i na koncentraciju te vrstu defekata. Uzorci naraštani pri idealnim parametrima rasta imaju prostorno homogena optička i elektronička svojstva na skali od $\sim 40\mu m$, ali su ta svojstva i vremenski homogena, u smislu da se ne mijenjaju značajno zbog utjecaja atmosferskih uvjeta.

Prvi dio moje doktorske disertacije odnosi se na uspostavljanje parametara rasta koji rezultiraju uzorcima poželjnih svojstava: visoko-kvalitetni, monokristalinični uzorci velike površine i niske koncentracije defekata. Nadalje, istraživala sam prostornu raspodjelu intrinzičnih defekata u 1L MoS_2 koristeći neinvazivne mikroskopske tehnike. Rezultate sam korelirala sa parametrima rasta te sam pokazala kako temperatura rasta (T_G) uvelike utječe na koncentraciju i vrstu defekata u 1L MoS_2. Iako svi uzorci analizirani u četvrtom poglavlju imaju oblik jednakostraničnog trokuta, bez vidljivih granica zrna ili drugih pukotina, njihova optička i elektronička svojstva se razlikuju upravo zbog toga što su naraštani na drugačijim T_G. Zadnji dio moje disertacije odnosi se na iskorištavanja defekata u 1L MoS_2 u svrhu poboljšavanja postojećih svojstava ili uvođenja novih. Korištenjem mješavine različitih metalnih prekursora moguće je sintetizirati legure ili heterostrukture preciznim kontroliranjem T_G tijekom procesa CVD sinteze. U petom poglavlju predstav-

ljene su preliminarne analize optičkih spektara jednoslojne $Mo_{1-x}W_xS_2$ legure i složene WS_2/MoS_2 heterostrukture.

Ključne riječi: 2D materijali, CVD sinteza, MoS_2 kristaliničnost, TMD legure i heterostrukture

Contents

List of Figures

List of Tables

Chapter 1

Introduction

Since the isolation of a single graphite sheet, known as graphene, two-dimensional (2D) materials have received considerable attention [1]. Its extraordinary properties and easy fabrication caused the incredibly fast growth of the 2D community in the last 20 years. Because graphene is a semimetal, its incorporation in the semiconducting industry is difficult since the opening of the bandgap requires high gate voltages and even then, the energy of the bandgap is around ~ 100 meV [2–4], which is not suitable for optoelectronics. The first 2D semiconductor was exfoliated in 2005 [5], and in 2011 the first field effect transistor based on a 2D semiconductor was fabricated [6], with improved performance in comparison to the silicon transistors. Apart from graphene, there are many other 2D materials, which can be divided into major three groups: 2D oxides, transition metal dichalcogenides (TMDs) and graphene-like materials [7]. The main characteristic of 2D materials is that the atoms have strong in-plane interactions, while the van der Waals interactions are formed in the out-of-plane direction. Due to the weak van der Waals interactions, many bulk crystals can be thinned to their monolayer (1L) form using Scotch tape. This allowed the cheap fabrication of 2D materials and is one of the main reasons for their popularity. One theoretical work identified over 1800 compounds that could be easily or potentially exfoliated [8], making numerous possibilities for their application in various fields.

2D materials can be synthesised using many techniques [9, 10], which can be categorized in two groups: top-down and bottom-up. The most common top-down techniques are mechanical exfoliation and exfoliation from the liquid phase, while the bottom-up techniques involve chemical vapour deposition (CVD), molecular beam epitaxy (MBE) and atomic layer deposition (ALD). Samples fabricated with the mechanical exfoliation technique tend to have a lower defect concentration than those synthesised with the CVD technique. But, on the other hand, mechanical exfoliation is not scalable, controllable nor reproducible, which makes it impossible to implement in the industry for device applications. The CVD technique is cheap, reproducible, scalable and controllable, but setting up the optimum parameters is time-consuming. In comparison to MBE and ALD, the

CVD technique does not require ultra-high vacuum conditions and can yield high-quality samples while working at atmospheric pressure. The CVD technique is also versatile when it comes to the substrate choice. The Si/SiO_2 substrate is the most common one, but once the recipe for a specific material has been ensured, other types of substrates can also be employed with the same synthesis recipe. Due to its simplicity, low cost, controllability, reproducibility and diversity of substrate choices, the CVD technique was determined to be suitable for the synthesis of all the samples analyzed in this Thesis. Detailed description of the CVD technique is given in Chapter 2.

Due to their high surface-to-volume ratio, 2D materials are highly susceptible to defects. Most common type of intrinsic defects are point defects, namely vacancies [11]. Other than point defects, the edges of monocrystalline samples represent the largest line defects. In polycrstalline samples, there are also grain boundaries, and if the sample is transferred to a rough substrate, ripples and nanopores can occur [11]. These effects have been extensively studied using atomically resolved techniques, which allow the quantification of defects in a sample. It was shown that the edges have a higher defect concentration than the interior [12–14]. Although scanning probe techniques allow the identification of defects with atomic precision, they usually cannot scan large enough areas for comprehensive device characterisation. Recently, Kiš et al. reported on a rapid and non-destructive electrical technique suitable for defect characterization in regular device architecture [15]. Understanding the influence of intrinsic point defects on electronic and optical properties in 2D materials is crucial for further development and optimization. Apart from these intrinsic defects, much attention has been turned to the defect-engineering. In this approach, research is oriented towards intentionally introducing defects in the material in order to change its properties. For 2D materials, such approach involves plasma treatment [16, 17], ion-beam bombardment[18], etching [19, 20], molecule surface functionalisation [21, 22], etc. Even though a certain number of defects are inevitably present in a material, optimization of the synthesis process may lead to a reduction in defect concentration, as will be discussed in Chapter 4.

1.1 Transition metal dichalcogenides

Transition metal dichalcogenides (TMDs) have a general formula MX_2 and their 1L form has three atomic layers: the plane of transition metal (M) atoms is sandwiched between two planes of chalcogen atoms (X). Their properties vary from topological insulators to superconductors, depending on the combination of the metal and chalcogen atoms and the crystalline phase [23]. This broad property range makes TMDs very attractive to the scientific and industrial communities due to many application possibilities.

Molybdenum disulfide (MoS_2) is one of the most investigated 2D materials [24]. This semiconductor is known in its bulk form as an efficient lubricant, but since its optical

bandgap is indirect, its application in optoelectronic devices is quite difficult, due to losses caused by phonon-assisted non-radiative recombinations. When thinned to the 1L form, the electronic structure of MoS_2 changes, the main one being the indirect-to-direct bandgap transition [25] even at room temperature. This property causes the increase of the radiative recombination probability in the 1L MoS_2, making it a promising candidate for efficient photovoltaic devices. Due to its reduced dimensionality and decreased Coulomb screening, many optical systems and processes can be investigated in 2D MoS_2 at room temperature. Some of these processes and systems will be explained in the next sections.
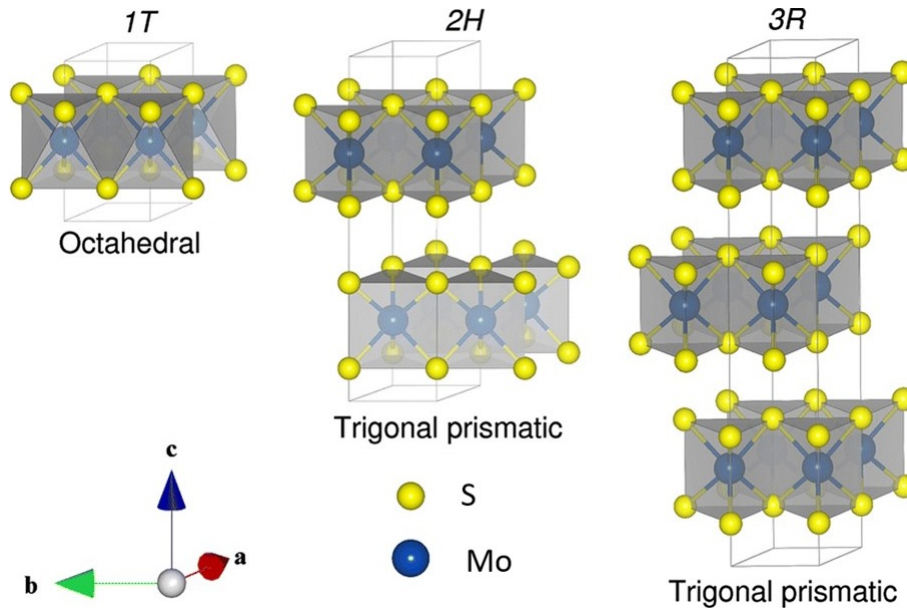
Figure 1.1: MoS_2 crystal structure: Octahedral (1T), trigonal prismatic (2H) and rhombohedral (3R) unit cell structures. Taken from [26].

The MoS_2 has a honeycomb crystal lattice, as shown in Figure 1.1. The molybdenum atom has six neighbouring sulphur atoms, and they are covalently bonded. Multilayer MoS_2 comes in two stable polytype structures: 2H and 3R. If the top layer is directly above the bottom one, then MoS_2 has a trigonal prismatic 2H semiconducting structure with D_{3h} symmetric group. In the 3R polytype, the three MoS_2 layers make a rhombohedral phase. Also, the 1L MoS_2 has a metastable metal phase, which is called 1T-MoS_2 [10]. The main distinction between the 2H and 3R polytype is that the 2H polytype is centrosymmetric only for even numbers of layers, while the 3R polytype does not have centre of inversion. The breaking of this symmetry is crucial for the observation of non-linear optical phenomena, such as second-harmonic generation (SHG) [27]. This technique allows for non-destructive investigation of grain boundaries and crystallographic orientation [28].

Bulk 2H-MoS_2 in its unit cell has 6 atoms, which yields 18 vibrational modes: 3 acoustic and 15 optical phonons. Lattice vibrations in bulk MoS_2 are given with the

following irreducible representation of D_{6h} point group: $\Gamma = A_{1g} + 2A_{2u} + B_{1u} + 2B_{2g} + E_{1g} + 2E_{1u} + E_{2u} + 2E_{2g}$ [29], where A and B represent the out-of-plane atomic vibrations and E represents in-plane atomic vibrations [30]. One A_{2u} and one E_{1u} mode are acoustic, A_{1g}, E_{1g} and E_{2g} are Raman active, while the second A_{2u} and E_{1u} are infrared active modes. Lastly, B_{2g}, B_{1u} and E_{2u} are optically inactive modes. Every E mode is actually doubly degenerate in the xy-plane [31]. Apart from the high-frequency modes, which characterize the vibration of atoms in a material (intralayer modes), in the multilayer MoS_2 there are also collective layer vibrations (interlayer modes), which have low frequencies typically below 100 cm^{-1} [32]. Low-frequency Raman modes are divided into two groups: shear and layer-breathing modes. The frequencies, spectral widths, intensities and lineshapes of all modes depend on the crystal quality and number of layers in a material. Low-frequency Raman modes can also be used for determining the stacking of multilayer materials [33].
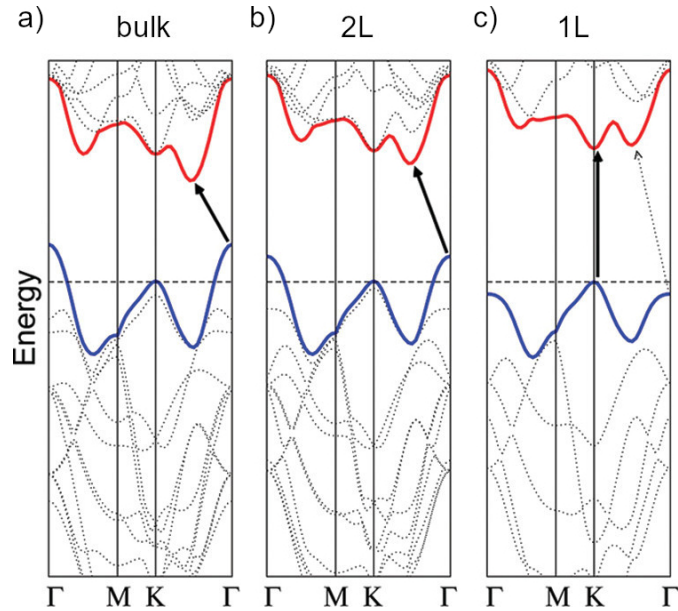
Figure 1.2: Electronic band structure of bulk, 2L and 1L MoS_2. The black arrows denote the lowest energy transitions. The red curve represents conductive band minimum, while the blue curve represents valence band maximum. Taken and adapted from [34].

Due to its honeycomb lattice, 1L-MoS_2 has conduction band minima and valence band maxima in the corners of the first Brillouin zone. In general, these corners, or K and K' valleys, are related with the time reversal operator and have the opposite z-component of the angular momentum (L_z) [10]. The electronic structures of 1L, 2L and bulk MoS_2 are shown in Figure 1.2. In the bulk MoS_2 the lowest energy transition is indirect, while in the 1L MoS_2 the bandgap becomes direct, which is the main reason for the substantial increase in photoluminescence (PL) emission intensity. Another change is that the bandgap decreases (redshifts) with the increasing number of layers.

Giant valence band spin-orbit splitting at K and K' valleys, shown in Figure 1.3, exists because the electrons in the heavy metallic atom have a large spin-orbit coupling (SOC)
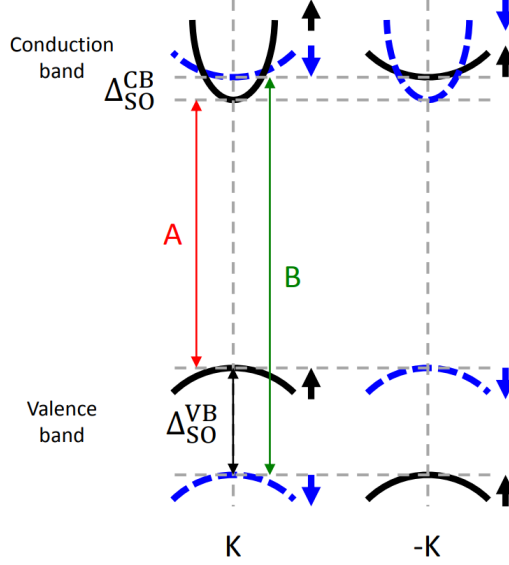
Figure 1.3: Spin-orbit coupling at K and K' points of the Brillouin zone for the MoS_2. Black (blue) lines denote the spin-up (spin-down) states. Δ_{SO}^{CB} and Δ_{SO}^{VB} are the conduction- and valence-band spin splittings. Red and green arrows denote the optically bright A and B transitions, respectively. Taken from [35].

to the nucleus. The magnitude of the spin-orbit splitting depends on the mass of the metallic atom, and it is greater as the metallic atom is heavier: for MoS_2 it's around 150 meV, while for WS_2 is 450 meV [10]. The splitting of the conductive band minima is much smaller and usually neglected in the first-order approximations.

Opposite L_z in K and K' causes opposite spin splitting, which then in turn creates a new degree of freedom called spin-valley locking [10]. This phenomenon allows selective population of valleys, called circular dichroism: with a right (left) circularly polarized light, only transition at K (K') is allowed [36–39].

In semiconductors, free electrons in the conductive band are coupled with free holes in the valence band. These Coulomb-bound pairs are called excitons [40]. In the case of 2D materials, due to their reduced dimensionality and reduced dielectric screening, the Coulomb interactions are enhanced, which yield increased exciton binding energies in the range of several hundreds of meV at room temperature [41–45]. The binding energy of an exciton is calculated as a difference between the bandgap energy, which is calculated with a certain theoretical model, and the optical bandgap energy, which is usually derived from the PL spectra peak position [46, 47]. Because of the mentioned SOC, there are two optically bright transitions in MoS_2, called A and B excitons, see Figure 1.3.

Apart from these simple quasiparticle systems, there are a plethora of other excitonic species in 2D TMDs [48]. If the exciton binds to another free carrier (electron or a hole), a trion is formed, with a binding energy ~ 10 meV. If there is a large concentration of excitons in a material, two excitons can create a bound state called a biexciton with even smaller binding energy, as shown in Figure 1.4.
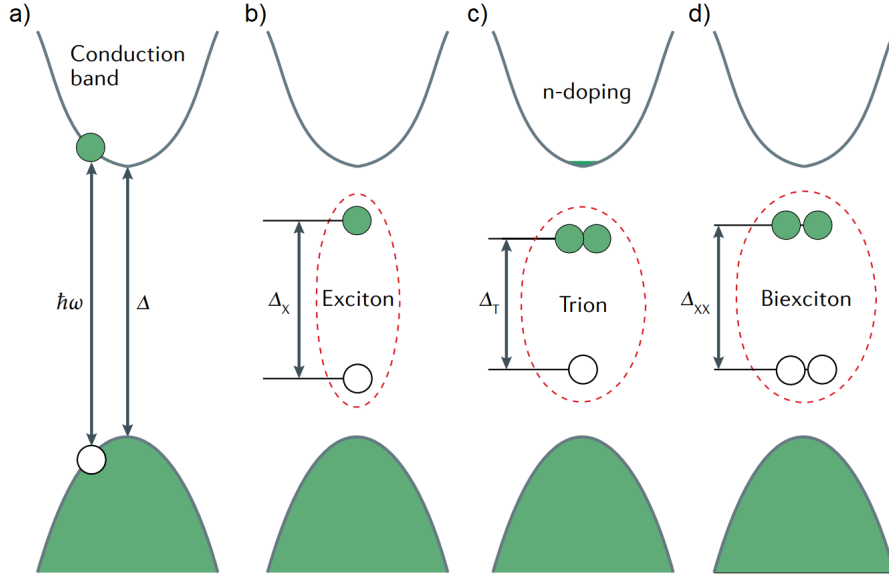
Figure 1.4: a) Free electron-hole pairs created in a semiconductor upon absorption of a photon with energy $\hbar\omega$. b) Excitons form due to the strong Coulomb attraction between an electron and a hole. c) Trion is created when additional electron (or a hole) and an exciton form a dipole-dipole interaction. d) A biexciton is formed due to the dipole-dipole interactions between two excitons. Taken from [48].

The electronic structure, and hence the optical properties, of MoS_2 can be changed by various means. Bandgap engineering has opened up many new research paths and shown the versatility of 2D materials. Electrical doping of MoS_2 causes the prominent redshift and broadening of the A_{1g} Raman mode, while the E_{2g} mode remains the same [49]. It was shown that uniaxial strain in MoS_2 leads to a bandgap redshift and a decreased PL intensity indicates a direct-to-indirect bandgap transition [11]. Also, with the decrease in temperature, the bandgap of MoS_2 blueshifts and also, below 100 K, additional emission line emerges, which is attributed to the so-called bound excitons. In this case, the excitons are bound to a lattice defect [50, 51]. This phenomenon will be discussed in Chapter 4. In multilayer materials, the angle between neighbouring layers, or twist angle, dramatically changes the electronic structure. It was shown that if the angle between two graphene layers is 1.1°, the material becomes a superconductor [52].

1.2 Transition metal dichalcogenide alloys and heterostructures

The sample's properties are most easily modified by introducing foreign atoms into its crystal lattice. Choosing suitable dopants is crucial for obtaining optimum results. For example, the radii of the host atom and the dopant must be similar in order to have good miscibility. That is why the best dopants are the elements in close proximity to the

transition metal or chalcogen element. In this way, the least amount of strain is introduced to the crystal lattice and the alloy will most likely have the same crystal structure as the original material. Doping MoS_2 with tungsten atoms leads to the blueshift of PL signal [53], while doping with Se atoms leads to the PL redshift [54], meaning that the MoS_2 bandgap can be tuned from ~ 1.8 eV to 2.0 eV. The optical properties of monolayer CVD-grown $Mo_{1-x}W_xS_2$ sample are analysed in Chapter 5. These extrinsic defects also modify electronic, optical and magnetic properties [11]. It was shown that doping intrinsically semiconducting TMDs with elements such as Fe, Co or Mn introduces room-temperature ferromagnetism [55–57].

Since TMDs have no dangling bonds, and the interlayer interactions are rather weak, novel materials called heterostructures (HS) can easily be fabricated just by vertical stacking one layer on top of the other, like stacking Lego blocks [58]. Van der Waals HS can be utilized for a broad range of applications: photodetectors [59], light-emitting diodes [60], photovoltaics [61], etc.
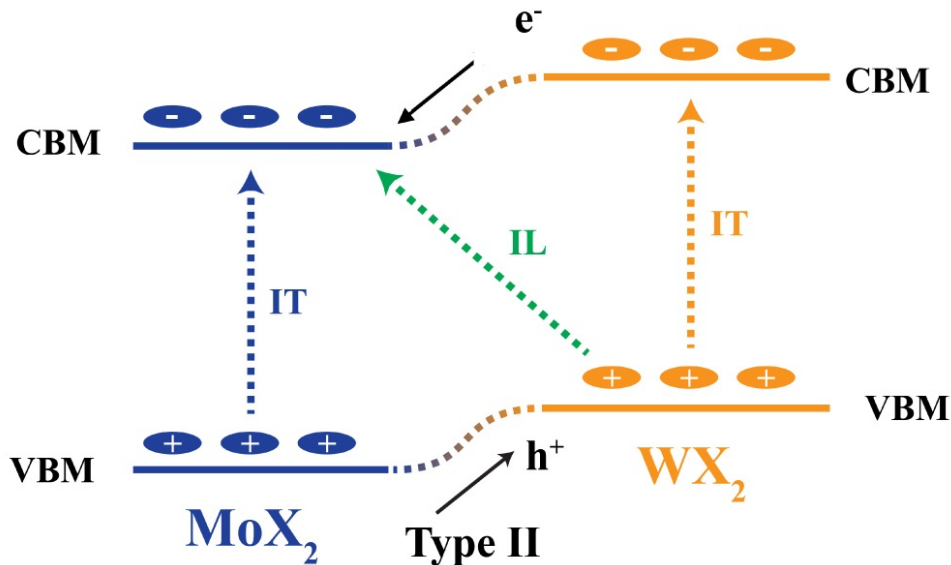
Figure 1.5: Band-alignment for MoX_2/WX_2 bilayer. Shown are conductive band minimum (CBM) and valence band maximum (VBM) levels of each material. Also, the direction of the electron (e^-) and hole (h^+) transfers at the interface are marked. The IT and IL represent intralayer and interlayer exciton, respectively. Taken and adapted from [62].

Heterostructures made from TMDs, such as MoS_2 and WS_2, form the type-II heterojunction: valence band maximum is located in one material and the conduction band minimum in another (Figure 1.5). This means that the excitons live at the interface between two layers, and because of that, they are called interlayer excitons (ILE). Vertical HS (v-HS) can be fabricated with all of the mentioned techniques, although the easiest one is the mechanical exfoliation. With this technique, it is also possible to control the twist angle, which tunes electronic and optical properties of the heterostructure, just like in homobilayers. In the case of artificially stacked v-HS, the ILE can only occur if the

interaction between layers is strong enough [63]. CVD-grown v-HS are somewhat difficult to produce, since the synthesis process requires significant tuning of the growth parameters, which will be discussed in Chapters 2 and 5. The main drawback of the CVD-grown v-HS is that the twist angle cannot be tuned, but the ILE is usually present in the CVD-grown v-HS. Materials can also be stacked horizontally, making the lateral HS (l-HS). L-HS made from semiconducting TMDs create p-n junctions with atomically sharp interface, which minimizes losses [64]. These types of heterostructures can only be produced with CVD and MBE techniques [65–67].

1.3   Potential applications and challenges

Figure 1.6 shows predictions for possible applications of 2D materials. Besides of the production of "classical" optoelectronic and photovoltaic devices, single photon emitters and quantum technologies based on 2D materials recently have become quite attractive field of research [68–70]. Silicon-based devices are already reaching the limits predicted by the Moore law [71] and losses due to heating and short-channel losses [72] are becoming a insurmountable obstacle. Semiconducting 2D materials, due to their reduced dimensionality and reduced dielectric screening, are suitable and natural replacement for the 3D silicon counterparts. Regarding their transport properties, good carrier transport is preserved even with the sub-nanometre material's thickness. Apart from the development of the transistors, 2D materials can also be building blocks for sensors [73], memory devices [74], photonics [75], etc.
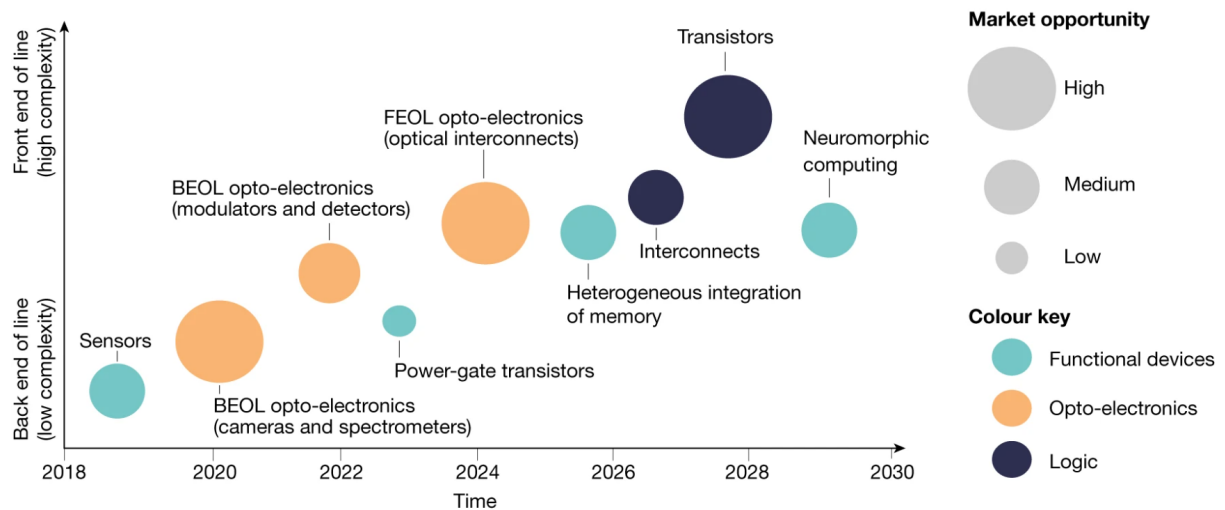
Figure 1.6: Possible applications of 2D materials. Taken from [72].

The biggest obstacle in the industrialization of 2D materials is reproducible and cheap synthesis which would produce high-quality and large-area samples [9]. As already mentioned, mechanical exfoliation technique is not adequate, even though large-scale samples

with low defect concentration can be fabricated. On the other hand, the CVD-grown large-scale samples often are polycrystalline with many grain boundaries and/or cracks which hinder optical and electronic properties.

Although the subject of controllable and scalable CVD growth of MoS_2 and other TMDs has been widely explored in the literature [14, 76–83], detailed study of as-grown MoS_2 samples that correlates the growth parameters with the spatial distribution of intrinsic defects has not been done.

In this Thesis, I explore the influence of intrinsic defects on the optical and electronic properties of MoS_2 monolayers. In order to have high-quality monocrystals, the CVD growth parameters first needed to be optimized. In Chapter 3, I show how the growth parameters influence samples' morphologies and optical properties. After establishing the optimum growth parameters, the spatial distribution of intrinsic defects in 1L MoS_2 was determined using various non-invasive microscopic techniques (Chapter 4). Understanding how intrinsic defects modulate properties in MoS_2 is important for defect utilisation via doping, alloying, or the synthesis of heterostructures (Chapter 5). The main results that are presented in this Thesis have been published in two papers:

1. **Senkić, A.**, **Bajo, J.**, Supina, A., Radatović, B., Vujičić, N., *Effects of CVD growth parameters on global and local optical properties of MoS₂ monolayers* Materials Chemistry and Physics **296** 127185 (2023),

2. **Senkić, A.**, Supina, A., Akturk, M., Gadermaier, C., Maiuri, M., Cerullo, G., Vujičić, N., *Microscopic investigation of intrinsic defects in CVD grown MoS₂ monolayers*, Nanotechnology **34** 475705 (2023).

Chapter 2

Experimental techniques

In this Chapter, experimental techniques used in this Thesis are presented. In Section 2.1, detailed description of synthesis processes for monolayer MoS_2 samples, $Mo_{1-x}W_xS_2$ alloys and heterostructures is provided. Following Sections present the scanning probe techniques used for investigation of topography and electronic properties (Section 2.2) and the optical techniques used for investigation of steady-state and ultrafast time-resolved optical properties (Section 2.3).

2.1   Chemical vapour deposition

CVD is commonly used technique for synthesising large-scale monocrystalline samples. As mentioned in Chapter 1, it is relatively cheap, simple, reproducible and scalable, which makes it superior to other fabricating techniques, such as mechanical exfoliation, exfoliation from liquid phase, ALD and MBE. In the CVD technique, the evaporated precursors are deposited on a suitable substrate in the atmosphere of an inert gas. Many factors need to be considered before the synthesis process: the choice of precursors, the growth promoters, inert gas and growth parameters are the most important ones.

For TMDs, the most commonly used precursors for metallic elements are the oxide powders, such as MoO_3, WO_3 [84–87], even though complex metal-organic precursors have also been noted in the literature [88, 89]. Here, I have used the liquid metallic precursors, obtained from molybdenum or tungsten salts dissolved in deionised (DI) water. In such way, the metallic precursor is placed directly on the substrate, eliminating one crucial synthesis parameter: distance between the substrate and precursors, which substantially influences the growth density and sample's morphology [90]. Also the evaporation temperature of liquid precursors is lower than the one for oxide powders, making the synthesis simpler, since temperatures above 900°C can be avoided. It is known from the literature [84, 86] that alkali metals promote the TMD growth, so a choice of the growth promoter is also of great importance. For MoS_2 synthesis, I have used the molybdenum salt with sodium, while for alloys and WS_2 synthesis a NaOH DI water solution was used.

The purpose of the inert gas is twofold: one is the transfer of precursor vapour onto the substrate and the other is creating a stable and contamination-free atmosphere in which the chemical reactions occur. High-purity argon gas ($> 99.9999~\%$) was used for synthesis of all the samples presented in this Thesis. Other than the inert gases, hydrogen gas can also be used during certain phases of synthesis. Hydrogen etches samples, creating more defects in the islands, but also it has been used in order to synthesise heterostructures [91–93].

The most challenging part in the CVD technique is finding the set of optimum growth parameters. This set of growth parameters yield samples with desired properties: large, isolated monocrystals, which do not deteriorate due to long atmospheric exposure. Some of the most important growth parameters are: precursor concentration (or mass ratio in case of oxide powders), inert gas flow rate, pressure inside the furnace, growth temperature, sulphur evaporation temperature, duration of synthesis and type of substrate. The parameters are not independent: for example, high precursor concentration would also require high degree of sulphurisation, i.e., high sulphur evaporation temperature, in order to achieve 1L growth. The influence of the growth parameters on the MoS_2 morphology and optical properties is presented in the Chapter 3.

The schematics of the CVD-setup used for all the samples in this Thesis is shown in Figure 2.1. Through the commercial CVD furnace, a smaller quartz tube ($\Phi = 17$ mm) was inserted. The additional home-made heater was placed ≈ 5 cm from the right edge of the CVD furnace, or upstream, in order to have better control of the sulfur evaporation temperature. Before the synthesis, the Si/SiO_2 substrate was cleaned with argon gas in order to remove dust particles. Afterwards, the silicon part was heated with propane gas to minimize organic impurities.

Different metal precursors and growth procedures were used in order to synthesise MoS_2 islands, $Mo_{1-x}W_xS_2$ alloys and heterostructures.
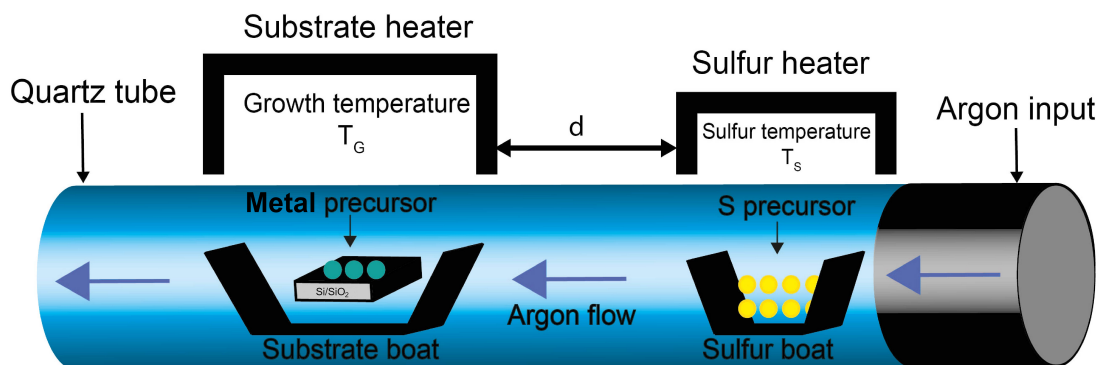
Figure 2.1: Schematic illustration of the CVD growth method based on solution-based metal precursors. Taken and adapted from [94].

MoS$_2$ growth procedure

As a molybdenum (Mo) precursor, the mixture of two DI water solutions in equal parts were used: ammonium heptamolybdate ((NH$_4$)$_6$Mo$_7$O$_{24}$ - AHM) and sodium-molybdate (Na$_2$MoO$_4$), both having 15.4 ppm concentration.

Preliminary work done in [94] showed that the mixture of these two solutions in the equal volume parts gives the best crystal morphology and good optical response. When using only the AHM solution, the MoS$_2$ islands were small and irregular and the PL spectra were good. The density of crystal growth was moderate and uniform throughout the substrate. In the case of sodium-molybdate solution, the islands were dendritic and their PL spectra were poor. The crystal growth density was high, so there were many clustered islands as well. This result also indicated that sodium serves as a good catalyst for the MoS$_2$ growth [95]. The proposed chemical reaction for obtaining the MoO$_3$ film from two DI water-based salt solutions is: (NH$_4$)$_6$Mo$_7$O$_{24}$$\times$ H$_2$O + Na$_2$MoO$_4$ $\rightarrow$ 8MoO$_3$ + 8H$_2$O + 2NaOH + 6NH$_3$.

A 10 µL droplet of this mixture was dropcasted on the previously cleaned Si/SiO$_2$ substrate and then placed on a hot plate at 120°C until the droplet had dried. The substrate is than placed in the CVD furnace at 650°C for 30 min in argon atmosphere (Figure 2.2) with maximum argon flow rate (ζ = 200 sccm[1]). After this, the argon flow rate was stopped and the furnace temperature was raised to the growth temperature (T$_G$). The sulphur heater was also turned on and set to the desired sulphur evaporation temperature (T$_S$). When both temperatures reached their target values, the argon flow was set to the desired value, between 50 and 100 sccm, and the synthesis process begins. After 10 min both heaters were switched off, the furnace was cooled to 650°C and the sample was immediately removed from the heater zone and kept on the left edge of the furnace until it reached $\sim$ 200°C, under maximum argon flow rate. After that, it was completely removed from the quartz tube.

Figure 2.2: Temperature and argon-flow profiles during the synthesis process of MoS$_2$.

---

[1]standard cubic centimetres per minute

$\mathbf{Mo_{1-x}W_xS_2}$ growth procedure

As a tungsten source, the tungstic acid, H_2WO_4, (99%, Sigma-Aldrich) was first dissolved in ammonia, then this solution was diluted to 75 ppm in DI water. As a growth promoter, 5 ppm of NaOH (dissolved in DI water) was used. Resulting W-precursor solution was a mixture of equal volumes of these two mixtures. For the Mo-precursor, the same mixture used in MoS_2 growth was used in this recipe, the only difference being that the concentration was 200 ppm, instead of 15.4 ppm.

Figure 2.3: a) Position of the substrates in the substrate boat for the $Mo_{1-x}W_xS_2$ growth. b) Temperature and argon-flow profiles during the synthesis process of $Mo_{1-x}W_xS_2$ alloy.

For the alloy synthesis, three previously cleaned substrates were simultaneously placed in the substrate boat, with configuration shown on the Figure 2.3 a). A droplet of 10 µL W-precursor was dropcasted on the first and second substrate, while on the third one a mixture of 5 µL Mo- and 5 µL W-precursors was used. The droplets were dried on a hot plate at 130°C. The substrates are then placed in the CVD furnace at 500°C for 10 min in argon atmosphere (Figure 2.3 b) with maximum argon flow rate ($\zeta = 200$ sccm). After this, the argon flow rate was reduced to 100 sccm and the furnace temperature was raised to the $T_G = 850$°C. When the furnace temperature reached 780°C, the sulphur heater was switched on and the sulphur temperature was set to 140°C. When both temperatures reached their target values ($T_G = 850$°C, $T_S = 140$°C), the argon flow was set to 75 sccm, and the synthesis process begins. After 5 min both heaters were switched off, the argon flow rate reduced to 50 sccm, while the samples were kept in the furnace, for ≈ 2 minutes. The quartz tube was cooled using compressed air until the samples' temperatures reached 500°C. After that, the samples were kept on the left side of the furnace until they cooled down to 200°C. Then they were completely removed from the quartz tube.

Optical analysis of PL and Raman spectra on islands from the two substrates with only W-precursor, showed that they are 1L $Mo_{1-x}W_xS_2$ alloys. Detailed PL and Raman spectra of one island is presented in Section 5.1. These substrates originally had only W-precursor and the Mo-precursors originate from the third substrate in the boat (Figure 2.3 a). At high tempertures, the Mo-precursors evaporated and incorporated in the WS_2 lattice. It

was shown in the literature [90, 96] that one substrate can be used only as a source of metallic precursor, while the others substrates are referred to as growth substrates. During the development of have also used a sodium tungstate dihydrate salt ($Na_2WO_4 \cdot H_2O$) with less than 5 ppm molybdenum impurities. Even though the used synthesis process was in favour of the WS_2 growth, only MoS_2 samples were synthesised, which was confirmed with PL and Raman spectra. These results show that small concentration of molybdenum is enough for MoS_2 synthesis. Further investigation of synthesis parameters for alloys and heterostructures needs to be conducted in order to fully explore the synthesis phase space.

Heterostructure growth procedure

Sodium-molybdate (40 ppm) was used as a Mo-precursor, while 200 ppm of previously mentioned W-precursor (H_2WO_4) was used as a tungsten source. The 10 µL of each solution was directly deposited on the previously cleaned substrate and then the substrate was placed on the hot plate at 130°C, until the droplet had dried. The substrate was introduced in the CVD furnace and heated to the growth temperature $T_G = 850$°C under argon atmosphere $\zeta = 100$ sccm (Figure 2.4). When the substrate reached temperature of 700°C, the sulphur heater was set to 140°C so the both temperatures reach their target values at the same moment. During the synthesis, the argon flow rate was set to 75 sccm. After 6 min, the growth temperature was lowered to 780°C, the sulphur heater was kept at 140°C, while the argon flow rate was increased to 100 sccm. Second growth stage was ≈ 2 minutes long, during which the WS_2 was synthesised. Afterwards, the substrate was held outside the heater zone ≈ 10 min until it reached temperature of 150°C.

Figure 2.4: Temperature and argon-flow profiles during the synthesis process of TMD heterostructure.

2.2   Structural investigation techniques

In order to determine the crystal quality, multiple scanning techniques were used. The atomic force microscope (AFM) was used to investigate sample's topography, height and roughness. With the same instrument, the MoS_2 work function was determined using the Kelvin Probe Force Microscope (KPFM) module. The scanning electron microscope (SEM) was also used to determine the sample's topography for high-resolution images.

2.2.1   Atomic Force Microscope and Kelvin Probe Force Microscope

AFM is non-invasive, high-resolution type of scanning probe microscope technique, which allows investigation of topography, work function (in the KPFM mode), conductivity and Young's modulus of a given material.

Figure 2.5: Illustration of the AFM probe. Taken from [97].

The main part of the instrument is a oscillating cantilever, which on the free end has a very sharp tip, as shown in Figure 2.5. During the scanning, the AFM tip is several nm away from the sample's surface. The photodiode detects the changes in the cantilever's positions during its oscillations, using a laser beam reflected from the cantilever, while the feedback loop transforms that change in the information about the sample's topography. The sample position can be precisely controlled via the piezoelectric xy-stage. There are two basic AFM modes of operation: the AC mode and the contact mode. In the contact mode the AFM tip is always in the contact with the sample, while in the AC mode the AFM tip is maintained at a constant distance above the sample's surface. This constant distance is maintained either by the amplitude modulation (AM) or by the frequency modulation (FM) of the cantilever's oscillation. In the case of AM mode, the changes in the amplitudes are the signal for the feedback loop and surface of the sample can be imaged, because the amplitude modulation is directly related to the force between the sample's surface and the AFM tip. In the case of FM mode, the oscillation's frequency

is modulated and it is connected to the force gradient between the sample's surface and the AFM tip. This mode of operation has a higher spatial resolution than the AM mode [98].

Atomic force microscope images of MoS_2 were taken with a JPK Nanowizard Ultra Speed AFM under ambient conditions. Non-contact AC mode was used for the acquisition with a set point of around 70%. NCHPt tips from Nanoworld with a nominal spring constant of 42 N/m were used. Images were processed with JPK Data Processing software.

Figure 2.6: Energy levels of the sample's surface and the AFM tip for three regimes: a) sample's surface and the AFM tip are not in electrical contact, b) sample's surface and the AFM tip are in the electrical contact, c) bias voltage V_{DC} is applied in order to null the contact point difference (V_{CPD}) and the force between the sample's surface and the AFM tip. E_v is the vacuum energy, E_{fs} and E_{ft} are the Fermi energies of the sample's surface and the AFM tip, respectively. Taken from [98].

For the KPFM measurements, the same AFM tips were used. When using this mode, both topography images and samples' surface potential are simultaneously obtained when the AFM tip moves above the sample. In Figure 2.6 energy levels of the sample and the AFM are shown in three different regimes. When the AFM tip is far away from the sample's surface (i.e. not in electrical contact), then their vacuum levels (E_v) are levelled, but their Fermi energies (E_f) are different (Figure 2.6 a). As the AFM tip and the sample's surface come in the electrical contact (Figure 2.6 b), their Fermi energies are equal, but their vacuum energies are different by V_{CPD}. The difference in the vacuum energies is called contact point difference. The levelling of the Fermi energies enables the flow of electrons from the sample's surface to the AFM tip. External bias voltage V_{DC} is applied in order to null the V_{CPD} (Figure 2.6 c). This bias voltage is equal to the difference of the work functions of the AFM tip (Φ_t) and the sample's surface (Φ_s). The work function of the material can then be calculated using following equation [98]:

$$\Phi_s = -e \cdot V_{CPD} + \Phi_t. \tag{2.1}$$

The calibration of the instrument for KPFM measurements was done using a freshly

cleaved highly ordered pyrolytic graphite (HOPG) sample, for which the work function is well defined: $\Phi_{HOPG} = 4.6$ eV [99]. The work function of the AFM tip was determined to be equal to $\Phi_t = 4.87$ eV.

2.2.2 Scanning Electron Microscope

Scanning electron microscopy (SEM) is a high-resolution scanning technique for determining the quality and chemical compound of the sample. Figure 2.7 shows a schematic of the SEM and its components. The electron beam is generated by the electron source and accelerated by the anode. The voltage applied to the anode determines the scanning resolution, but one must be careful not to damage the sample. A set of magnetic lenses is used for focusing and improving spatial resolution, while the scanning coils are used for steering the electron beam over the sample's surface. There are many physical processes which happen during the interaction between the electron beam and the sample [100]. These processes generate electrons and photons which are collected in order to determine sample's quality, chemical composition and topography.
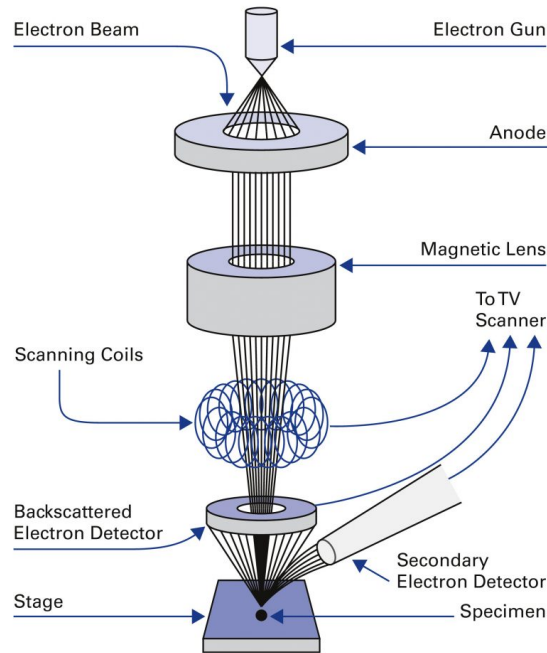
Figure 2.7: Illustration of the SEM components. Taken from [101].

For the research presented in this Thesis, Tescan VEGA3 SEM with a tungsten cathode was used for observation of MoS_2. Imaging was performed at a working distance of 10 mm and with 5 kV accelerating voltage in resolution mode, while the image acquisition was done with a secondary electron (SE) detector.

2.3   Optical techniques

Photoluminescence (PL) is a process in which a photon is emitted from a material after it absorbs light from an external source. In the case of semiconductors, the electrons in the valence band absorb high-energy photons and are excited to the conduction band. The electrons are cooled down to the bottom of the conduction band via electron-phonon scatterings. Once they are at the bottom of the conduction band, they bind to the holes in the top of valence band and form excitons. During the recombination of bright excitons, light emitted from the material is detected using CCD camera (Figure 2.8 a).
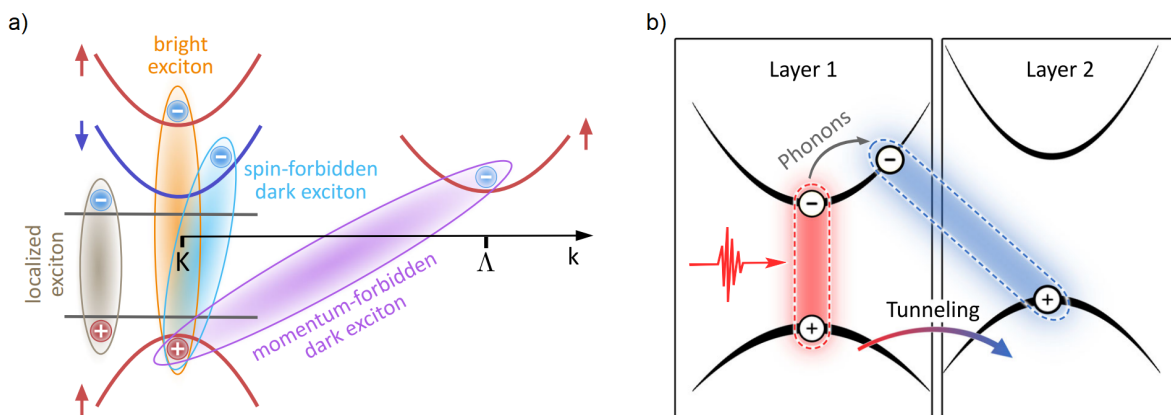
Figure 2.8: a) Illustration of different types of excitons in 1L TMDs. b) Illustration of excitons in a heterostructure. Taken from [102].

Described process is common in materials with a direct bandgap, when the conductive band minimum (CBM) and valence band maximum (VBM) are located in the same point of the Brillouin zone. In the case of indirect bandgap, the exciton recombination is phonon-assisted and its efficiency is smaller. Apart from the bright excitons, different types of dark excitons exist, namely spin-forbidden and momentum forbidden. In molybdenum based TMDs, the spin-allowed bright excitons have the lowest energy, but for tungsten based TMDs, this is not the case, as shown in Figure 2.8 a). This type of dark excitons can be investigated in low-temperature magneto-optic measurements [102]. The momentum dark-excitons involve exciton-phonon interactions and these states can be made bright by introduction of strain or with probing intra-excitonic 1s-2p transition [102].

As mentioned in Chapter 1, defects in material create localized in-gap states. Electrons and holes can be trapped in these states and their properties are presented in Chapter 4. Because these states are close to the CBM or VBM, they are thermalised and cannot be distinguished at room temperature. Low-temperature PL measurements are needed in order to directly investigate these localized states.

In Figure 2.8 b) the interlayer excitons are illustrated. As mentioned in Chapter 1, type-II band alignment in a TMD heterostructure has CBM in one material and VBM in the other. After the photoexcitation, electrons or holes can tunnel to the lowest energy

level, and thus are located in different materials forming an interlayer exciton (ILE). This type of excitons can also be observed at the room temperature, due to its relatively large binding energy (~ 100 meV).

Photoexcitation of a semiconductor changes the occupation of electronic levels and populations of photoexcited free charges and related quasiparticles, such as excitons, trions, and biexcitons, influencing the optical properties of materials. Photoluminescence is a widely used technique for studying the electronic and optical properties of semiconducting materials and quantum dots and it provides information about the material's steady-state properties upon the absorption of light. On the other hand, ultrafast optical spectroscopy gives insights into the dynamics of the excited state upon photoexcitation, including relaxation times, energy transfer processes, and other transient phenomena. Due to its time resolution in tens of femtoseconds to picoseconds, it is an ideal technique for capturing ultrafast processes and disentangling all of the multiple scattering processes occurring after photoexcitation.

Ultrafast transient absorption experiments require two temporally and spatially overlapped pulsed lasers: pump and probe. With the pump pulse, the electrons in the material are excited to a high-energy level and with the probe pulse, which arrives on the sample after a certain time delay, the relaxation processes are investigated. Pump pulse usually has narrow energy distribution, while the probe pulse is a broad white-light continuum, so the changes in the material's optical response can be investigated. Depending on the time-scales of the process one wants to investigate, different laser pulse durations are utilised. For relaxation and recombination processes in TMDs, femtosecond lasers are employed.

2.3.1 Optical measurements

All PL and Raman measurements presented in this Thesis have been done at the Institute of Physics, Zagreb on two setups. The ultrafast transient absorption measurements have been done at the Physics Department in Politecnico di Milano during an ERASMUS+ internship. The optical micrographs (OM) were taken with a commercial optical microscope Leica DM2700 M, Leica Microsystems, Wetzlar, Germany. Setup schematics and descriptions are presented in the following sections.

Home-made PL and Raman confocal microscope

Home-made PL and Raman confocal microscope in backscattered coniguration, shown in Figure 2.9 was used for the investigation of optical properties of CVD-grown Mos_2 samples. It is equipped with 532 nm (2.33 eV) and 488 nm (2.54 eV) single-mode laser sources, a white-light source for the optical microscopy and contrast reflectivity measurements and objectives with 5x, 10x and 50x magnification. For all the measurements 532 nm laser

source and 50x objective with NA = 0.75 was employed. In the detection part, a set of Bragg filters are used for measuring low-energy Raman modes for 532 nm excitation. The detected signal is focused onto a 50 μm multimode fiber and led to a spectrometer (Andor Shamrock 500i) with 150, 300 and 1800 mm^{-1} gratings. The spectrometer is coupled with a CCD camera (Newton EMCCD DU970P) which is cooled to -80°C. For PL (Raman) spectra, the 150 (1800) mm^{-1} is used. EMCCD technology offers significant increase of sensitivity which is suitable for the detection of low level signals. The laser power on the sample was 500 μW, unless stated differently. The spotsize in the focus is approximately 700 nm.

For low-temperature measurements, the continuous flow optical cryostat (HiRES, Oxford Instruments) was mounted on the xy-manipulator stage. The temperature-dependent measurements were conducted in a range from 4.2 K up to 300 K with liquid helium as a coolant.
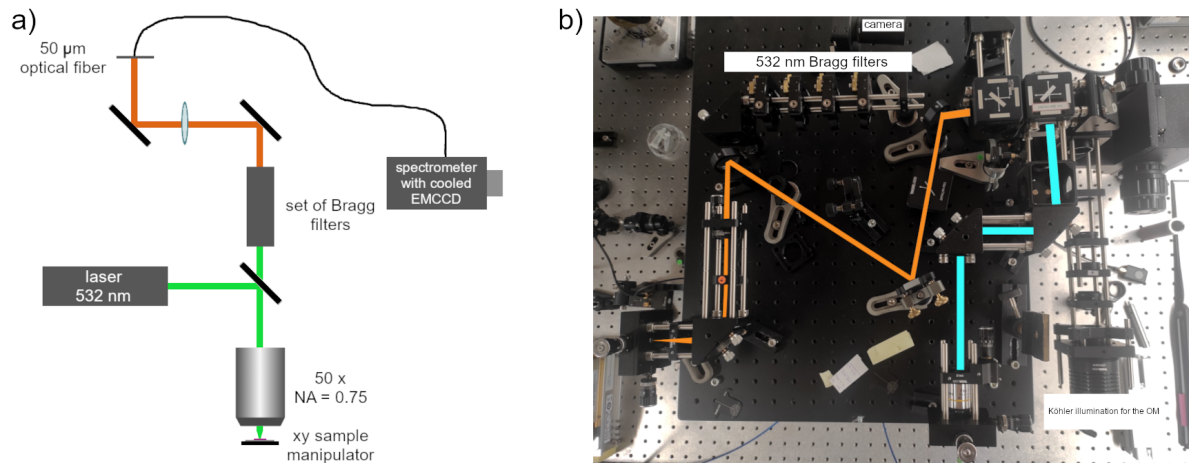
Figure 2.9: a) Simplified schematics of home-made PL and Raman confocal microscope. b) Photograph of the home-made PL and Raman confocal microscope utilized for the 488 nm laser excitation.

Renishaw in-via Raman microscope

The commercial Renishaw in-via Raman microscope (Figure 2.10) was used for fast PL and Raman mapping of MoS_2 samples analysed in Section 3.3, alloys and heterostructures. It is equipped with a 532 nm (2.33 eV) laser source, objectives with 10x, 50x and 100x magnification. For all the measurements, the objective with 100x magnification (NA = 0.9) and spotsize of 300 nm was used. In the detection part, it has three gratings with 150, 600 and 2400 mm^{-1} and the signal is collected with a lens and projected onto a CCD camera. For the PL (Raman) measurements a grating with a 150 (2400) mm^{-1} constant was used.

Figure 2.10: Photograph of commercial Renishaw in-via Raman confocal microscope.

Ultrafast transient absorption microscope

The home-built ultrafast transient absoprtion microscope was used for investigation of relaxation processes in MoS$_2$ monolayers, presented in Section 4.2.3. Schematics of such setup is shown in Figure 2.11.
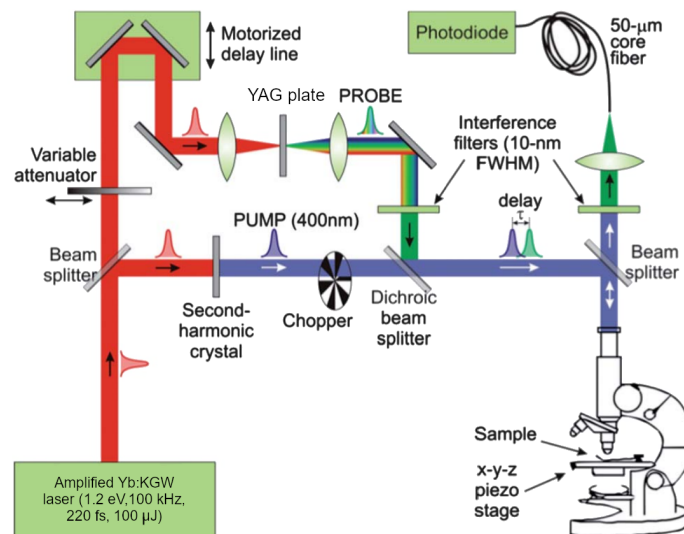
Figure 2.11: Schematics of ultrafast transition absorption microscope. Taken and adapted from [103].

The ultrafast TA microscope [103] starts from an amplified Yb:KGW laser (Pharos, Light Conversion) generating 100-μJ, 220-fs pulses at 1.2 eV photon energy and 100 kHz repetition rate. A 12-μJ fraction of the energy is used to power the microscope. The 2.4 eV pump pulses are obtained by Type I second harmonic generation in a β-barium borate crystal cut at θ=23.4°, while the broadband probe pulses are obtained by white-light continuum generation in a 6-mm thick YAG plate. Pump and probe pulses, whose delay

is controlled by a mechanical delay line, are collinearly combined by a dichroic mirror and focused on the sample by $100\times$ Leica microscope objective (NA = 0.9), with the resulting beam diameter on the sample of 580 nm. The sample position is raster scanned by a motorized XY-scanning stage (Standa-8MTF) to allow investigation of different positions on the sample. In the epi-detection mode, the reflected probe beam is recollimated by the same infinity-corrected objective lens and separated by a 50:50 beam splitter.

Probe pulses are spectrally filtered at 680 nm (690 nm) using a 25 nm (10 nm) bandwidth interference filter for 1L MoS_2 samples grown at 800°C (900°C) and focused on a Si photodiode. Different probe energies correspond to different average A exciton energies obtained from the room temperature PL measurements in investigated samples. The pump pulse is modulated at 10 kHz by a mechanical chopper and the pump-induced differential reflectivity ($\Delta R/R$) is recorded by a lock-in amplifier.

Chapter 3

Tuning the synthesis parameters for optimum MoS$_2$ crystal quality

In this Chapter, I describe how the CVD growth parameters influence morphology and the optical properties of MoS$_2$ monolayers. The main results of this chapter have been published in a paper *Effects of CVD Growth Parameters on Global and Local Optical Properties of MoS$_2$ Monolayers*, Materials Chemistry and Physics **296** 127185 (2023).

The CVD grown samples from liquid-based Mo-precursors were synthesised under different growth conditions, explained in detail in the Chapter 2, and their overall optical properties were investigated immediately upon synthesis by measuring PL and Raman spectra on different islands across the substrate and from different sample zones. If the obtained optical properties are not satisfying, then new hypothesis for growth parameters is suggested and another synthesis process begins. Such a work-flow is shown in Figure 3.1 and it allows improving the knowledge about the future growth parameters space, its resulting morphology accompanied by sample properties with as few experimental runs as possible.
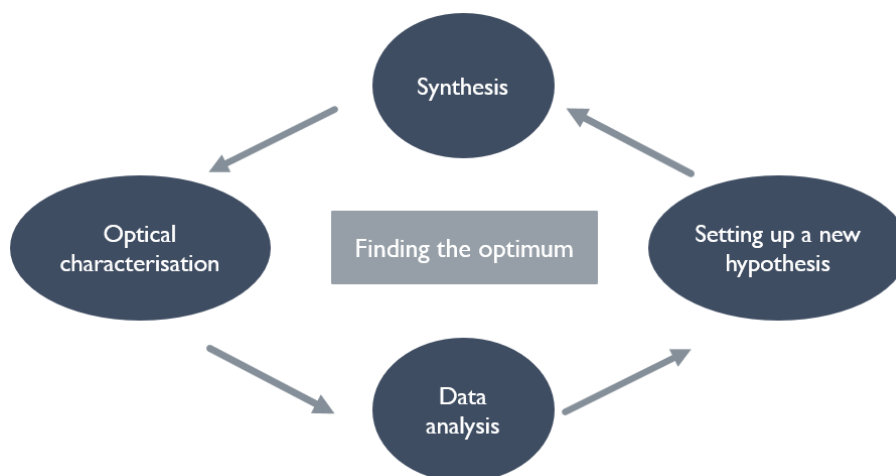
Figure 3.1: Work-flow for systematic synthesis and subsequent characterisation.

In this work, I tuned three growth parameters:

- growth temperature, T_G, from 800°C to 900°C,

- sulphur temperature, T_S, from 135°C to 145°C and

- argon flow, ζ, from 50 sccm to 100 sccm,

which yielded in total of 25 different samples. For easier management, the samples were divided into 5 batches, as shown in Table 3.1. With the T_G increase, the amount of molybdenum in the local reaction area increases, due to the formation of initial nucleation sites; by increasing the T_S, overall sulphur concentration increases, while the increase of argon flow ζ leads to higher degree of sulpfurisation and promotes lateral island growth.

Table 3.1: Growth parameters for 25 monolayer MoS_2 samples sorted into 5 batches.

Batch No.	1	2	3	4	5
T_S (°C)	135	140	145	140	140
ζ (sccm)	50	50	50	75	100
T_G (°C)	800				
	825				
	850				
	875				
	900				
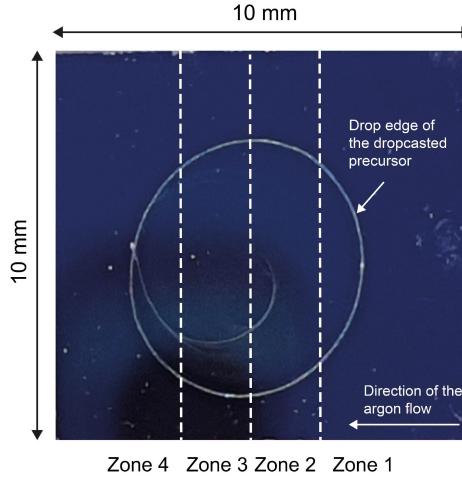
Figure 3.2: Photo of the sample depicting the droplet deposition contour in the substrate center. The direction of the argon flow is indicated with an arrow. Dashed lines indicate zone borders that separate four zones (1-4) on the substrate, with the first one being the closest to the sulphur boat.

Figure 3.2 shows a photo of the sample with the droplet deposition contour in the substrate center. The 10 mm x 10 mm substrate is divided into 4 zones, marked by the white dashed lines, with the first zone being upstream, i.e., closest to the sulphur

boat. The second and the third zone are located in the central part of the droplet, while the fourth zone is the furthest from the sulphur boat. Under the assumption that the Mo-precursors are evenly distributed across the zones (neglecting the droplet edge), this four-zone approach enables investigation of sulfur inflow's influence on the sample growth on different parts of the substrate. The quality of the sample was checked on a randomly chosen monocrystal from each of the four zones, by measuring PL and Raman spectra. In such way, the systematic growth method with high reproducibility over the whole substrate was ensured. The lateral size of the chosen monocrystal was up to 50 µm.

3.1 Morphology evolution

Figure 3.3 shows the change in MoS_2 morphology with respect to change in growth temperature T_G and sulphur evaporation temperature T_S. The argon flow was set to 50 sccm. The growth temperature was changed from 800°C to 900°C, in steps of 25°C, while the sulphur temperature was changed from 135°C to 145°C in steps of 5°C. For lower T_G, as the T_S increases the MoS_2 samples become polycrystalline and dendritic (Figure 3.3 a, f, k and b, g, l), which indicates sulphur-rich growth conditions. Triangular shape can be restored by increasing the T_G, as shown in Figure 3.3 (i, j) and (n,o).
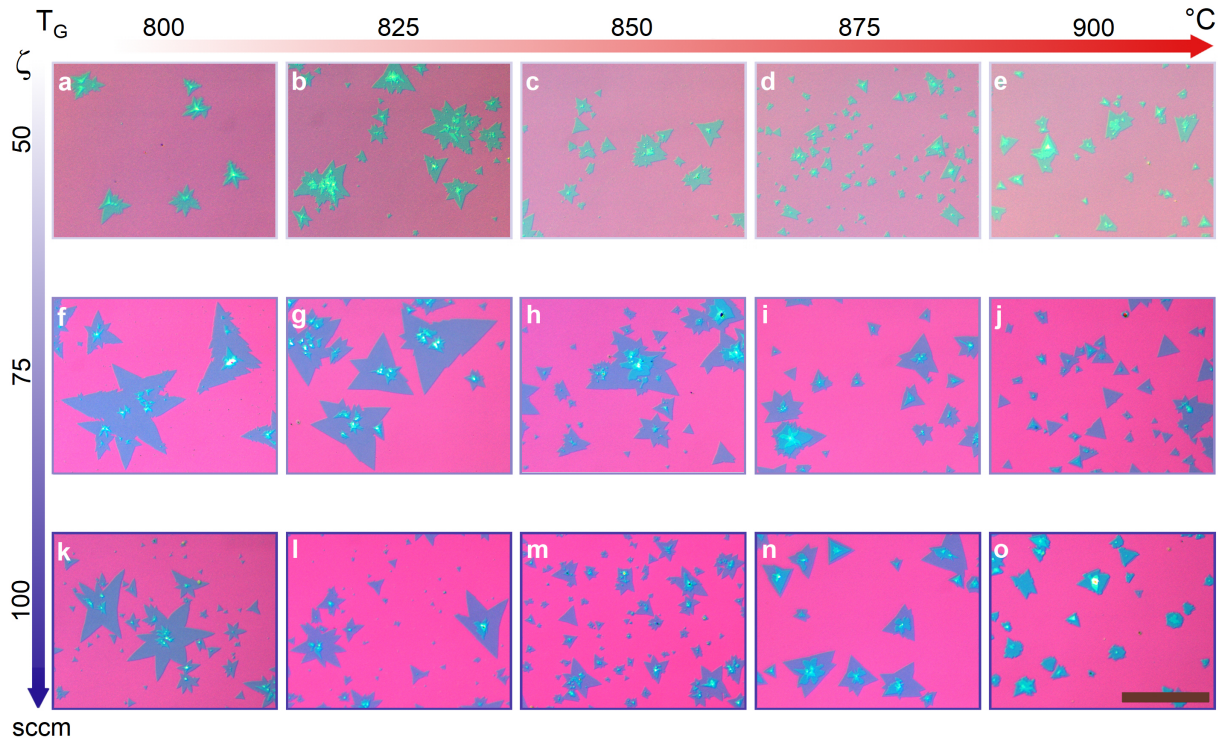
Figure 3.3: OM images of as-grown MoS_2 samples as a function of growth temperature (T_G) and sulphur evaporation temperature (T_S). The argon flow was 50 sccm. Scale bar is 100 µm.

With the increase of T_G, the amount of Mo-precursors in the local reaction area also increases [104] and if the degree of sulphurisation is sufficient, the equilateral triangular

growth will be favourable. On the other hand, if the degree of the sulphurisation is not sufficient, than poly-crystalline islands will be synthesised [95]. As an example, at the droplet edge, where the concentration of Mo-precursors is high, the isolated monolayer growth is achieved onlyy at high T_G, while the bulky growth with the noticeable depletion zone ($\sim$ 10 μm) is observed at low T_G. For moderate and high T_S only for high values of T_G (875 and 900°C), multilayer growth is observed, since the evaporation of the Mo-precursors promotes the epitaxial growth of additional layers on top of the existing one [79, 95, 104, 105]. On the other hand, for low T_S value (135°C) the degree of sulphurisation is low for the whole T_G range and multilayer growth is achieved for every T_G. Dense growth, accompanied with three-point star shapes or poly-crystalline dendritic growth is typical for sulphur rich environment, as can be seen in Figure 3.3 (k, l). The sulphur rich environment is usually a consequence of low T_G, high T_S and low concentration of Mo-precursors.
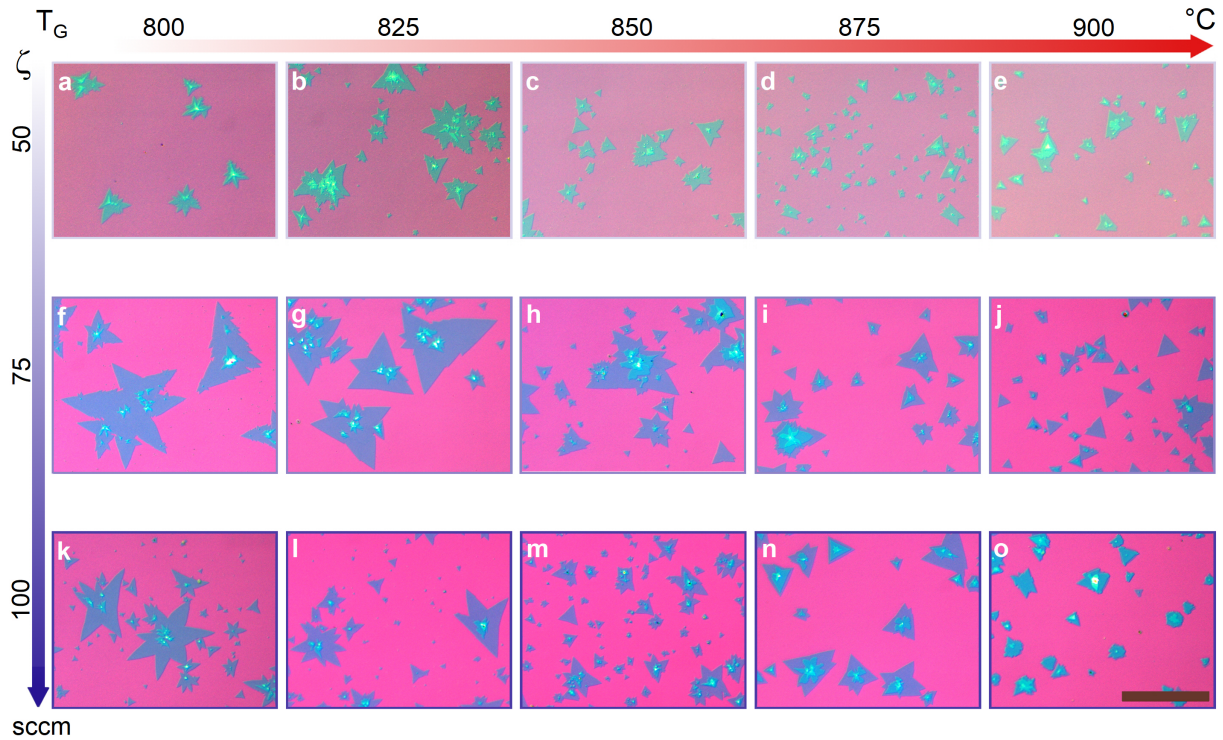
Figure 3.4: OM images of as-grown MoS$_2$ samples as a function of growth temperature (T_G) and argon flow (ζ). The sulphur evaporation temperature was 140°C. Ideal growth conditions result in OM image (j). Scale bar is 100 μm.

In addition to the influence of T_S on the morphology of MoS$_2$ islands, I investigated how the argon flow ζ changes their morphology and quality. The results are shown in Figure 3.4. The sulphur temperature was fixed at 140°C. The range of the growth temperature is the same as in the previous case and the argon flow was changed from 50 sccm to 100 sccm in step of 25 sccm. For lower T_G values, the increase of ζ increases the islands' lateral size and activates more nucleation sites, as shown in Figures 3.4 (a, f, k)

and (b, g, l). It was observed that there is a limit of argon flow, above which no evident increase in lateral size is observed. For high ζ, the MoS_2 islands likely grow under kinetic conditions, rather than the thermodynamic ones [90], which results in irregular, dendritic growth. Kinetic growth conditions promote the mass transfer process, which contributes to the increase in the island growth rate, as seen in Figures 3.4 (a, b, c, f, g, h, k, l, m) with the formation of dendritic poly-crystals, which are not suitable for production of high-quality 2D devices.

Kinetic growth conditions imply that atoms do not have enough time to set in the right place in the crystal lattice, which means that the probability of creating point defects is increased [90]. Thermodynamic growth conditions can be achieved again by increasing T_G, which is observed in Figure 3.4 (j, n, o), where equilateral triangular growth is restored. In these conditions, the increased evaporation rate of Mo-precursors in the local reaction area (due to high T_G) is countered with the increase of sulphur inflow which enables the growth of equilateral triangles. This implies, that with the control of argon flow rate during the synthesis, the reaction process can be precisely controlled: blocking effects of increased Mo-precursors concentration can be avoided by increasing the flow rate; morphology and islands' growth density and their lateral size can be tuned to desired shape and values [106].

For our CVD setup, the sample with best morphology is synthesised under this set of growth parameters: $T_G = 900°C$, $T_S = 140 °C$ and $\zeta = 75$ sccm, which is shown in Figure 3.4 (j). At this moderate argon flow value, the density of MoS_2 islands is moderate, the islands are mostly isolated equilateral triangles, with lateral size of ≈ 40 μm. Triangular shape implies Mo-zz terminations, as observed in similar works [90, 107]. This set of growth parameters give not only the optimum morphology, but the optical properties throughout the substrate, as will be shown in the following subsection.
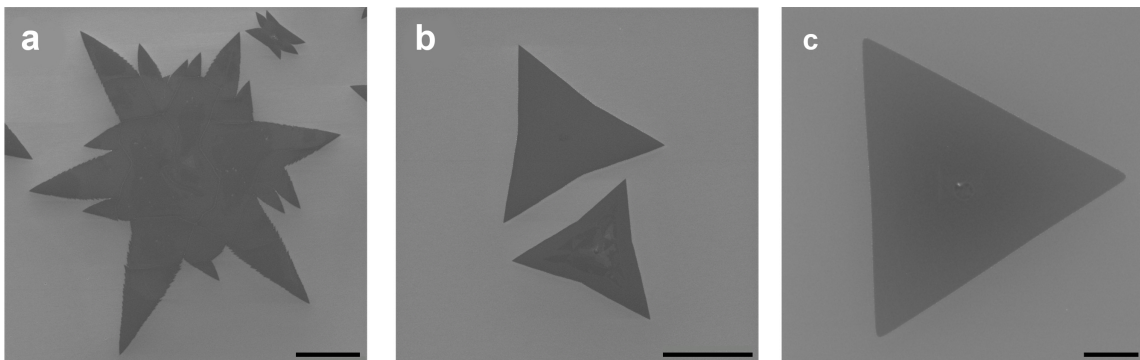
Figure 3.5: SEM images of as-grown MoS_2 samples as a function of (T_G, T_S) for argon flow $\zeta = 50$ sccm. a) (775°C, 145°C), b) (775°C, 140°C), c) (900°C, 140°C). Scale bar is 20 μm.

Tunability of MoS_2 morphology was also investigated using SEM, as shown in Figure 3.5. For low values of argon flow (Figure 3.5 (a)), sulphur rich environment (low T_G accompanied with high T_S) produces dendritic and polycrystalline growth, with extremely large islands (larger than 60 µm). Decreasing the sulphur evaporation temperature, the morphology is tuned towards concaved triangles, as shown in Figure 3.5 b), and finally, by increasing the growth temperature T_G, the equilateral triangular shape is restored (Figure 3.5 (c)), with increased lateral size.
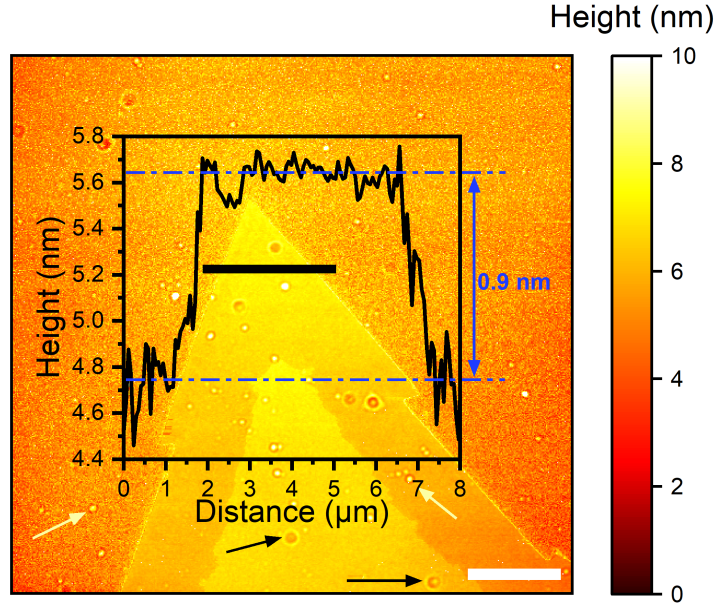
Figure 3.6: AFM topography image of the as-grown MoS_2 bilayer obtained for the growth parameters: $(T_G, T_S, \zeta) = (900°C, 140°C, 75 \text{ sccm})$. Inset shows corresponding height profile along the solid black line. The unreacted precursors and craters on the substrate surface are indicated by yellow and black arrows, respectively. Scale bar is 2 µm.

The surface of the as-grown MoS_2 islands was investigated with AFM, as shown in Figure 3.6. The inset shows the height profile taken along the solid black line. The height of the MoS_2 island is ~0.9 nm, which agrees well with the previously reported monolayer thickness of the CVD-grown MoS_2 [108]. The yellow and black arrows in Figure 3.6 represent the unreacted precursors' residues and craters on the substrate surface, respectively, which are common for the CVD-grown samples [109]. Unreacted precursors have higher topography, which increase the substrate surface roughness (~4.9 nm), while the surface of the MoS_2 island is rather smooth (~0.15 nm). Craters most likely appear due to the presence of NaOH and NH_3 compounds in Mo-precursors which cause etching of SiO_2 substrate [78]. These features can be removed by transferring the as-grown samples on untreated, clean substrate [109].

3.2 Optical properties

In this study, apart from determining the correlation between the growth parameters and the sample's morphology, the second part was establishing the connection between the growth parameters and the sample's optical properties. The four-zone approach allowed the investigation of so-called global optical properties, i.e., properties across entire substrate. From this data, I have determined the optimum growth parameters for which the optical properties do not change significantly across the substrate. Afterwards, I have conducted detailed analysis of optical properties on five islands from the batch 4 in order to determine how growth temperature influences local optical properties in 1L MoS_2 monocrystals.

3.2.1 Global optical response

For global optical response, I correlated the A exciton energy, linewidth (measured as full width at half maximum - FWHM) and intensity with the growth parameters. The PL intensity is correlated with the exciton lifetime (τ_E) by following relation: $I(PL) \sim \tau_E/\tau_R$ [110, 111], where τ_R is the radiative recombination time, which is related to the exciton lifetime: $\tau_E^{-1} = \tau_R^{-1} + \tau_{NR}^{-1}$. The non-radiative recombination time (τ_{NR}^{-1}) mostly depends on the properties of defect states and traps, which provide more non-radiative decay channels, and thus, shorten the τ_{NR} [14, 112, 113]. The radiative recombination time is temperature dependent and intrinsic to a specific material. Since the measurements were done at room temperature, the PL intensity of both A and B excitons depends only on the defect concentration, which changes the non-radiative contribution of the exciton lifetime. That is why the information of A exciton intensity was taken as a figure of merit for sample quality. Study of McCreary et al. [114] also showed that the intensity ratio of A and B excitons can be used for determining the sample quality. Point PL and Raman spectra were taken close to the island's centre, avoiding the nucleation site. The main result on how growth conditions influence the PL spectra of A exciton is shown in Figure 3.7. The spectra are grouped by the substrate zones and growth temperature for each batch.

Strong PL emission across all four substrate zones is observed in samples at high growth temperatures, grown under moderate sulphur inflow ($T_S = 140°C$, $\zeta = 75$ sccm or 100 sccm, batches 4 and 5), as shown in Figure 3.7. On the other hand, samples from Batch 1, where the degree of sulphurisation is low ($T_S = 135°C$, $\zeta = 50$ sccm), have modest PL emission. In Section 3.1 it was discussed how the growth temperature changes the ratio of Mo/S precursors in the local reaction area, thus changes the samples' uniformity and quality. Moderate growth temperatures (825 and 850°C), for all combinations of T_S and ζ give less intense PL emission. If we take a look at the substrate uniformity, the samples grown in Batches 4 and 5 have more intense PL signals for higher T_G in all
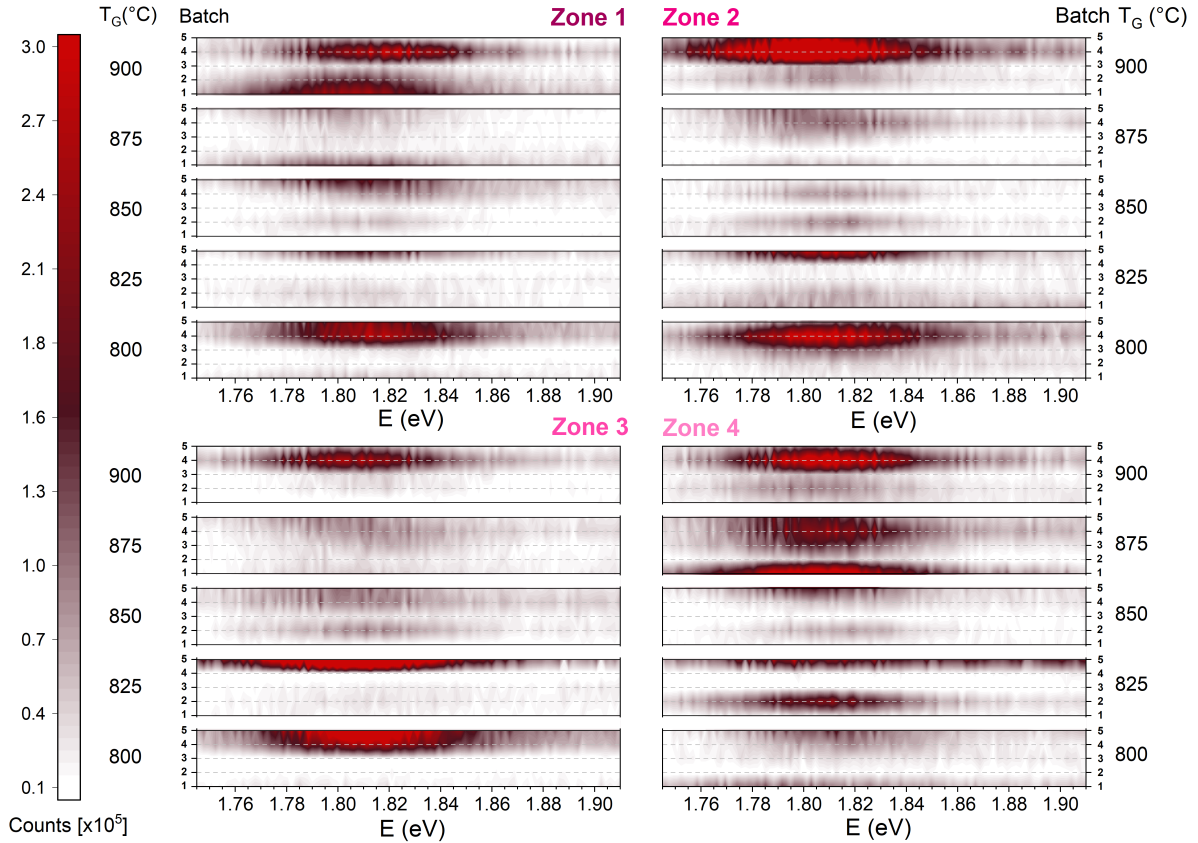
Figure 3.7: The PL spectra of MoS_2 A exciton as a function of different growth conditions for all four zones on a substrate.

four substrate zones. These results, in combination with the analysis made in previous section, are in accordance with the hypothesis that the growth parameters influence both morphology and optical properties of a material. Also, favourable morphology implies good or excellent optical properties on a larger scale.

The A exciton energy and FWHM are comparable in all samples, across all four substrate zones, as shown in Figure 3.8 a) and b), respectively. The A exciton energy averaged over all islands is (1.80 ± 0.02) eV with average FWHM value of (34 ± 5) meV, which is comparable with previously reported values [78, 115, 116]. The A exciton energy is less dispersed for zones 3 and 4, for all values of T_G, as shown in Figure 3.8 a). This homogeneous optical response is most likely the result of the more suitable position of local reaction area with respect to the sulphur boat. In these two zones the Mo/S ratio is well balanced and the result is uniform growth with homogeneous optical response. These results can be correlated with the FWHM results shown in 3.8 b). Also, it is observed that samples synthesised at higher T_G have smaller deviation from the calculated mean values for A exciton energy and FWHM. This means that, if the favourable growth conditions are set, the sulphur concentration gradient across the Si/SiO_2 substrate, which may arise from the relative distance between the substrate zone and the sulphur boat position, is not crucial for producing uniform, high-quality MoS_2 sample growth across the whole
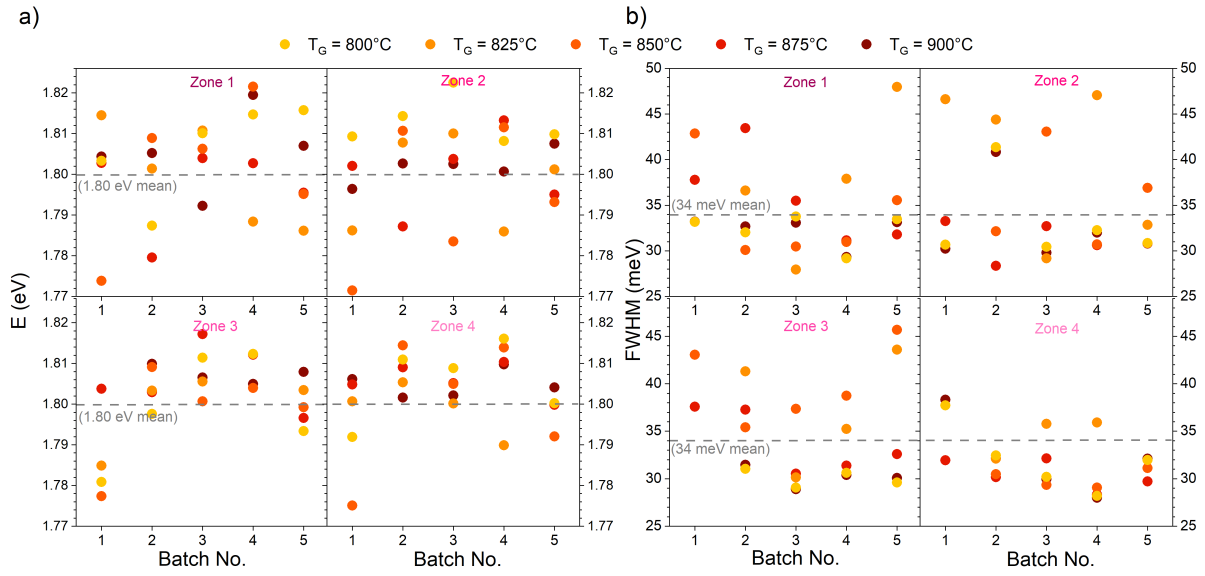
Figure 3.8: a) Energy and b) FWHM of A exciton for different batches and different substrate zones.

substrate.
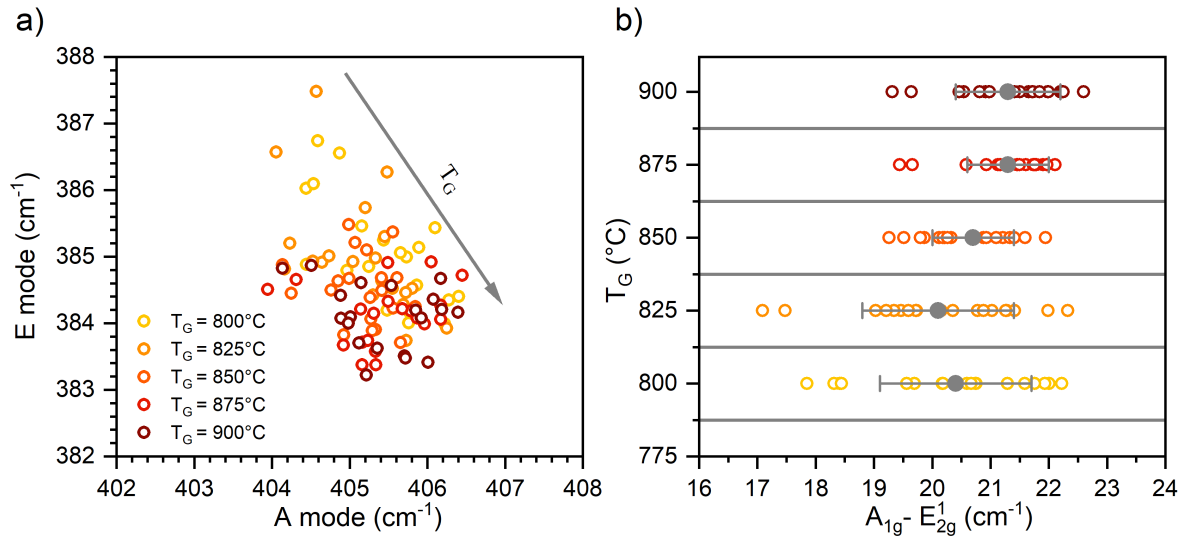
Figure 3.9: a) Frequency of MoS_2 Raman modes and b) frequency difference of A_{1g} and E^1_{2g} Raman modes for different T_G.

Photoluminescence spectra can be changed with presence of defects, such as vacancies or grain boundaries, or by imposing strain and electrostatic doping [107]. The presence of strain and/or electrostatic doping can be determined with analysis of Raman spectra, since the frequency of E^1_{2g} mode is sensitive to strain [117, 118], while the frequency of A_{1g} mode is sensitive to the electrostatic doping [49, 118]. The frequencies of Raman vibrational modes for different growth temperatures are shown in Figure 3.9 a). Note that other growth parameters are also different, since the classification is done only by the T_G

31

value. Increased growth temperature may induce the strain in the as-grown MoS_2 islands on Si/SiO_2 substrate during the fast cooling phase from the set growth temperature to 650°C, since the MoS_2 and SiO_2 have different thermal coefficients [119, 120].

With an increase in T_G, the E^1_{2g} mode slightly softens, while the average frequency of the A_{1g} mode does not change significantly with the growth parameters. As a result, the frequency difference between A_{1g} and E^1_{2g} modes is modulated with T_G by $\approx 0.9\ cm^{-1}$ (3.9 (b), which is lower than the instrument's resolution. Such a small change indicates that the strain and doping are not the main cause for inhomogeneous optical response [121] between sample batches. Instead, possible reason might be existence of structural defects. For all investigated islands, Raman spectra did not show existence of molybdenum oxide phases, which would indicate low degree of sulphurisation [104]. In the cited paper, results from the X-ray photoelectron spectroscopy show that the increased degree of sulphurisation yields improved stoichiometry and reduced concentration of molybdenum oxides within the probed region.

Detailed analysis of PL and Raman spectra over the whole substrate, show that the sufficient degree of sulphurisation influences the optical properties of CVD-grown samples, where the good or excellent optical response was obtained for higher T_G values, moderate T_S and ζ values. For our CVD setup, the optimum set of growth parameters is: $T_G = 900°C$, $T_S = 140°C$ and $\zeta = 75$ sccm, for which the optical response is excellent in all four substrate zones. Other sets of growth parameters with $T_G = 900°C$ (such as from batch 1 and 5) yield low PL intensity, which means that increased T_G is not sufficient for producing good optical response, but also other growth parameters need to be tuned as well. For $T_G = 900°C$, the energies of A and B excitons are nearly constant for all other growth parameters, throughout all substrate zones and equal to $E_A = 1.805 \pm 0.006$ eV and $E_B = 1.98 \pm 0.02$ eV.

3.2.2   Local optical response

In order to investigate the influence of T_G on the local optical properties of a randomly chosen monocrystal MoS_2 island, I measured PL maps at room temperature for each sample in the batch 4. In the previous subsections, I showed that the sample with the optimum morphology and global optical properties is synthesised under following conditions: $T_G = 900°C$, $T_S = 140°C$ and $\zeta = 75$ sccm. Here, I investigated how the growth temperature influences the island's uniformity, in terms of intensity and energy of A exciton.

The PL maps presented in Figure 3.10 show the spatial distribution of A exciton energy (Figure 3.10 a - e) and intensity (Figure 3.10 f - j) in islands synthesised under different growth temperatures. In all islands, the variation in the PL intensity is accompanied with the variation in the energy of A exciton. With the increase of T_G, the energies of A exciton become more homogeneous and slightly red-shifted. The intensity of A exciton
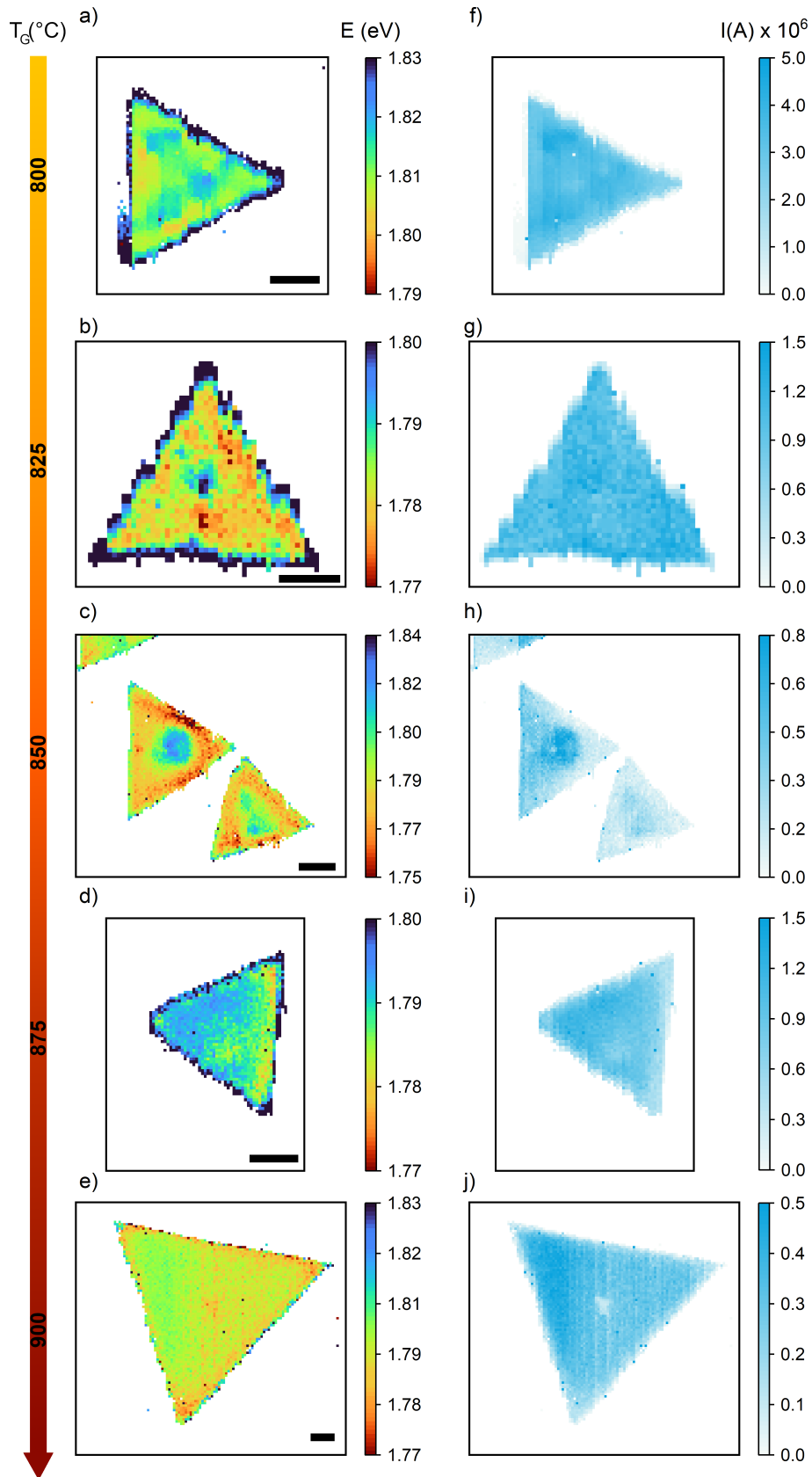
Figure 3.10: Spatial distribution of A exciton energy (left column) and intensity (right column) at room temperature for samples in batch 4. Scale bar is 5 μm.

in sample grown at $T_G = 900°C$ changes across the island due to the laser defocusing which happened during the measurement. Even though all these islands have favourable morphology (equilateral triangles with lateral sizes between 15 and 50 µm), their local optical response heavily depends on the growth temperature. Higher T_G values provide islands with homogeneous optical response over their entire areas. As already mentioned in previous subsections, higher T_G increases locally the concentration of Mo-precursors within the local reaction area, and if the degree of sulphurisation is sufficient, synthesised sample will have good or excellent quality [77]. This implies, that by tuning the argon flow rate together with the growth temperature, it is possible to avoid the blocking effects on Mo-precursors. This control not only tunes the samples' morphology toward equilateral triangles with large lateral sizes [109], but also makes their optical response uniform. From these microscopic optical measurements across the entire island, I conclude that the sample with growth parameters: $T_G = 900°C$, $T_S = 140°C$ and $\zeta = 75$ sccm is synthesised under the optimum growth conditions and has homogeneous optical response [77]. In the next subsection I will demonstrate that these samples are also resilient to prolonged exposure to atmospheric conditions.
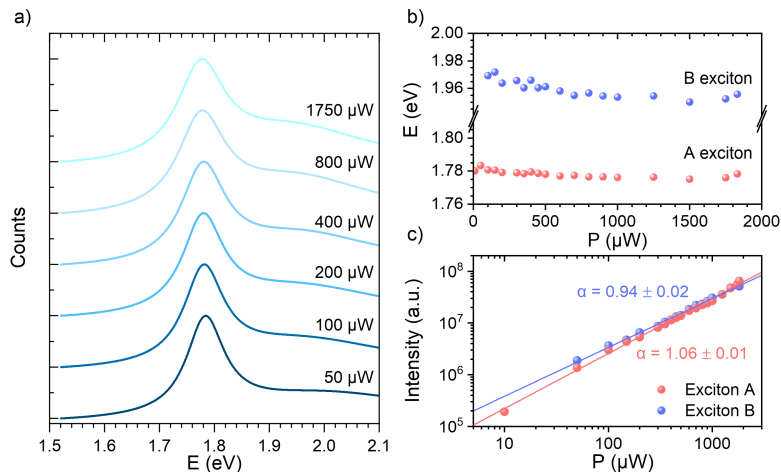
Figure 3.11: a) PL spectra dependence on laser power in ambient conditions for MoS_2 island synthesised at $(T_G, T_S, \zeta) = (900°C, 140°C, 75 \text{ sccm})$. Both the PL spectral line-shapes a) and energies b) are unaffected by increased laser power. c) PL intensity shows linear dependence on the laser power.

On the sample grown under optimum conditions, I also conducted excitation power dependent measurements, in order to investigate the interaction between the island and the substrate. It is known from the literature that the high excitation fluence can enhance trion and biexciton emission in TMDs [116, 122–124]. Dependence of the PL spectra on the excitation power is shown in Figure 3.11. For all incident excitation powers there are two emission lines (Figure 3.11 a)), which coincide with the emissions from neutral A and B excitons with energies (Figure 3.11 b)) of (1.778 ± 0.002) eV and (1.970 ± 0.006) eV, respectively. Since the PL intensity of both excitons linearly depends on the

incident excitation power (Figure 3.11 c), we can conclude that these two emissions are dominated with excitonic quasiparticle systems, and not defect states [125]. The influence of defects on the optical properties in 1L MoS_2 monocrystals will be further discussed in the next Chapter. Because this sample shows no variation in the spectral shape or energies of A and B excitons, with the increase of incident excitation power, I assume that the observed behaviour is a result of the interfacial effects between the MoS_2 and the substrate. If the MoS_2 - substrate interaction is strong, then the electron transfer from the MoS_2 to the substrate is efficient and thus the creation of trions is hindered [111]. Since the PL spectral line-shape does not change over the broad range of incident excitation power, there is no indication of a local heating [77]. And finally, the linear dependence between the excitons' intensities and the incident excitation power indicates the absence of exciton-exciton recombination process [126, 127].

3.3 Uniformity across substrate and ageing effect

After determining the optimum set of growth parameters, many samples were synthesized under these specific growth conditions, for the purpose of future investigations. Some of those samples have travelled a great distance across Europe with my colleague Josip Bajo, who tested a few experimental setups at KTH in Stockholm, before finally settling in Vienna Center for Quantum Science and Technology (VCQ). In May 2023, more than 2 years after synthesising the MoS_2 samples, we have checked the homogeneity of their optical response at the Institute of Physics in Zagreb. It is important to mention that these samples were not encapsulated with hexagonal boron-nitride (hBN), or stored in ultra-high vacuum. The samples were kept in their original plastic box and stored in a desiccator. Even though I did not make PL maps immediately upon the synthesis, so the direct comparison of A exciton energy and intensity is not possible in a real sense of the ageing effect, I believe that the results shown in Figure 3.12 can still be a good indication of samples' high quality, since the mean value of the A exciton energy and its total PL intensity does not vary significantly from island to island (Figure 3.12). This confirms that the growth parameters $T_G = 900°C$, $T_S = 140°C$ and $\zeta = 75$ sccm provide samples with homogeneous optical response, even though the measurements were made on samples which are more than 2 years old.
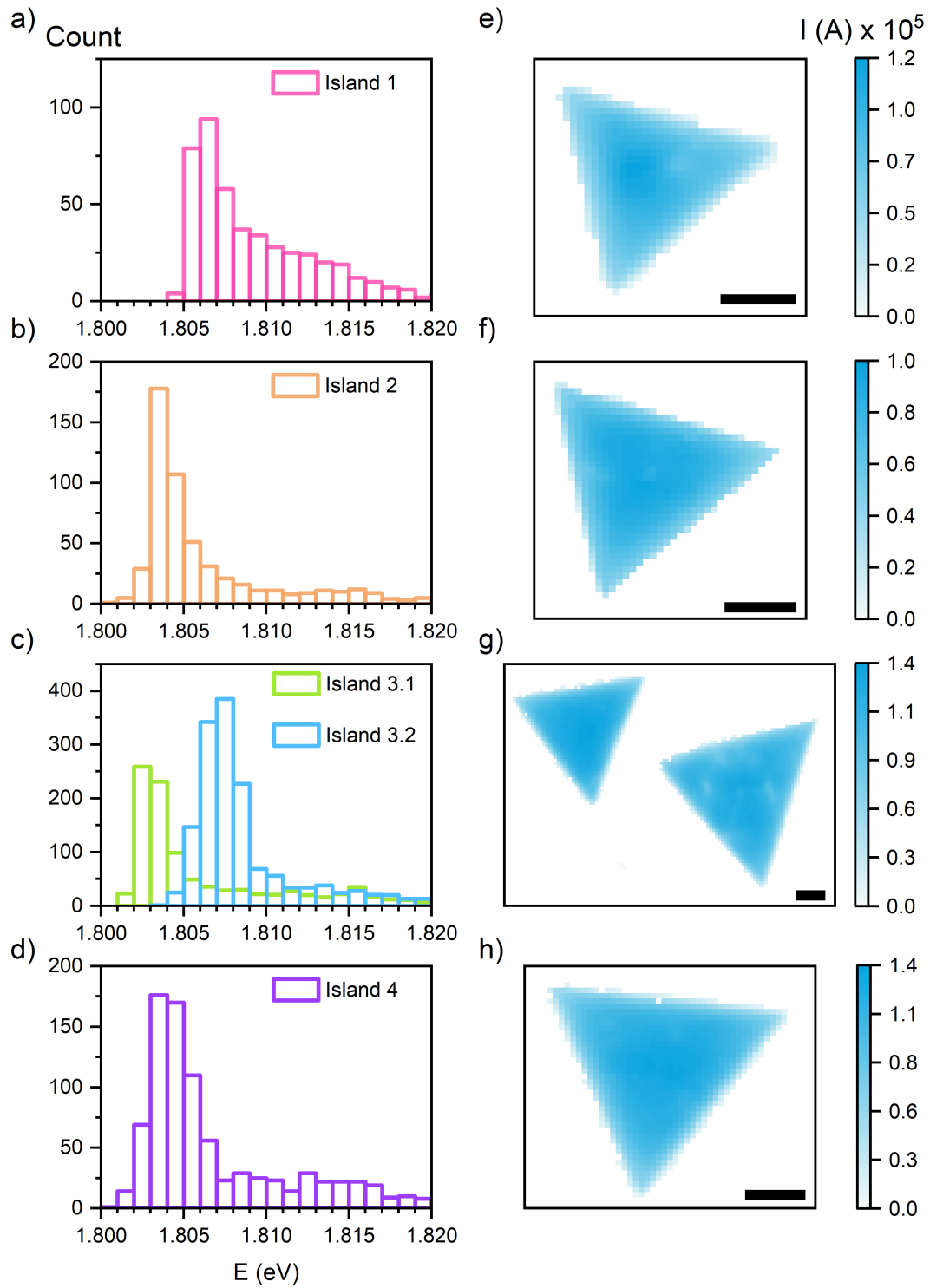
Figure 3.12: Left column: energy distribution of A exciton in each island, grown under optimum set of parameters. Right column: Spatial distribution of A exciton intensity. Scale bar is 5 μm.

3.4 Conclusion

In this Chapter I have shown how the growth parameters influence the samples' morphology and optical response. This was done by the systematic change of growth parameters and by correlating them with the optical response of MoS_2 monolayers. It was observed that the growth parameters are not mutually independent and careful tuning of each of them is needed in order to obtain favourable equilateral triangular monocrystalline growth. The samples synthesised at the optimum growth conditions have: 1) uniform optical response throughout the whole substrate; 2) homogeneous local optical response in terms of A exciton energy and intensity spatial distribution; 3) stable and homogeneous optical response even 2 years after the synthesis. In the subsection 3.2.2, I showed that the equilateral triangular growth is a necessary, but not sufficient condition, in order to have the best quality samples.

In the next Chapter, I will show detailed microscopic analysis of the islands from batch 4. I will correlate their electronic properties with low-temperature PL maps and room temperature ultrafast transient absorption measurements in order to investigate how growth temperature influences the existence and spatial distribution of intrinsic point defects in monolayer MoS_2 islands.

Chapter 4

Distribution of intrinsic defects in CVD-grown MoS$_2$ monocrystals

In this Chapter, I present how one synthesis parameter, namely the growth temperature T$_G$, influences the spatial distribution of intrinsic point defects in CVD-grown MoS$_2$ monolayers. The main results of this chapter have been published in a paper *Microscopic Investigation of Intrinsic Defects in CVD Grown MoS$_2$ Monolayers*, Nanotechnology **34** 475705 (2023).

As discussed in the previous Chapter, sample's optical properties significantly depend on its growth parameters. Optimum growth parameters yield samples with homogeneous and non-deteriorating optical response, with no evident degradation on a microscopic scale. In this Chapter, the focus is on the five samples from batch 4, introduced in Chapter 3, synthesised under following growth parameters: T$_G \in [800, 825, 850, 875, 900]°C, T_S = 140°$C, $\zeta = 75$ sccm. PL maps obtained at room temperature are shown in Figure 3.10 in the previous Chapter. In this Chapter, I will discuss how the growth temperature influences the spatial distribution of intrinsic defects in as-grown MoS$_2$ triangular monolayers. Spatial distribution of defects in all five samples was determined using KPFM and low-temperature PL maps. Detailed analysis was done on two samples, with extreme growth temperatures: T$_G = 800°$C and T$_G = 900°$C. Sample synthesised at lower T$_G$ has position-dependent electronic and optical properties and its excitons have shorter lifetime, due to the higher defect concentration. On the other hand, sample synthesised at T$_G = 900°$C has homogeneous electronic and optical properties, with longer lived excitons.

4.1 Electronic properties

Kelvin Probe Force Microscopy was used in order to directly detect and measure influence of defects on material's intrinsic properties, such as the surface potential. This provides information on defects' spatial distribution across MoS_2 islands. Measured work function depends on the material's intrinsic properties, since the defects modify its Fermi energy and thus, its work function. It is known from the literature [98, 128] that in MoS_2 defects lower its Fermi energy towards the valance band and increase its work function Φ.

Samples synthesised at lower growth temperature (800-850°C), shown in Figure 4.1 a)-c), exhibit significant difference between the interior and the edges in KPFM work functions, as indicated in the line profiles denoted with the white dashed line. In these samples, the edges have higher work function than the interior, meaning that the defect concentration is higher at the edges. Work function becomes homogeneous for samples with higher values of T_G (Figure 4.1 d),e), which indicates improved crystal quality.

The lowest mean value of the work function is achieved in the sample with $T_G = 900°C$ and it is equal to $\Phi = 4.5$ eV, while for the sample synthesised at $T_G = 800°C$ the work function is higher and equal to $\Phi = 4.67$ eV. Even though the theoretical value of the work function ($\Phi = 4.71$ eV) for pristine MoS_2 is not achieved [129], it is important to bear in mind that the absolute value of the measured surface potential heavily depends on the type of substrate, environment, probe type, signal feedback of the equipment etc. [130]. Previous studies based on resolved techniques such as transmission electron microscope (TEM) and energy dispersive spectroscopy (EDS), showed that the sulphur vacancies are the most common type of point defects in CVD grown MoS_2 samples, which create localized in-gap states [12, 14, 128, 131, 132]. Based on those analyses, sulphur vacancies are the most probable reason for inhomogeneous electronic properties in CVD-grown MoS_2 samples with lower T_G values.
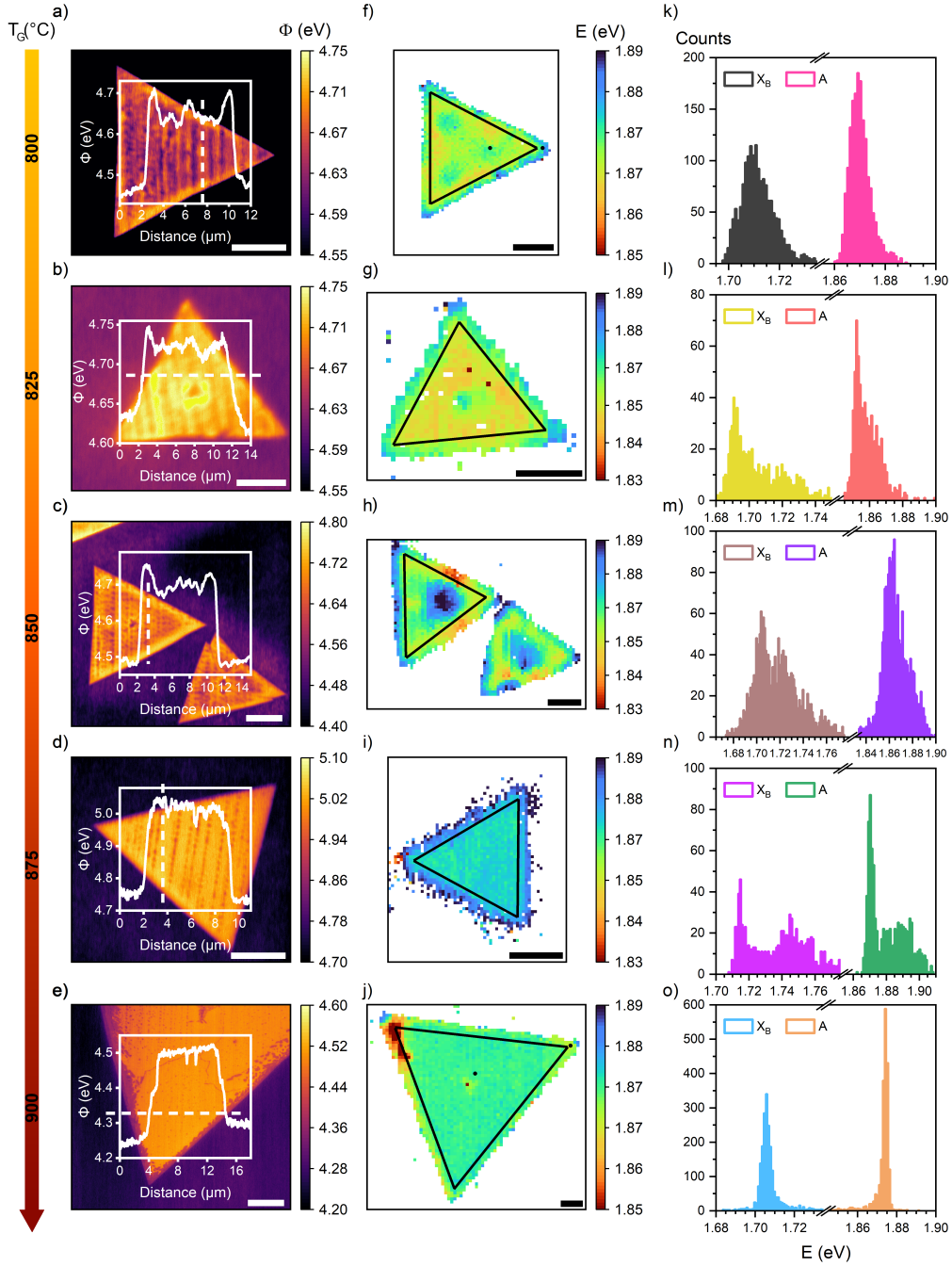
Figure 4.1: Left column: KPFM maps of MoS$_2$ samples synthesised under different growth temperatures T$_G$. Insets show the work function measured across the sample (work function line profile) denoted by the white dashed line. Middle column: PL maps of A exciton energy taken at 4.2K. Right column: Energy distribution of X$_B$ and A excitons at 4.2K for the same samples. Black lines represent two distinct regions on islands: edge and interior, analysed further in Figure 4.3 f) - j) . Marks " • " represent points where the power- and temperature-dependent measurements shown in Figures 4.4, 4.5 and 4.6. Scale bar is 5 µm.

4.2 Optical properties

At temperatures below 100 K, most 2D semiconductors exhibit additional low-energy feature in their PL spectra, as shown in Figure 4.2. The feature is ascribed to localized in-gap states, created by defects and these states trap free excitons. This emission line is called bound exciton (X_B), which means that the neutral A exciton is bound to a lattice defect. Its binding energy, which depends on the defect type, is equal to: $\Delta = E_A - E_{X_B}$, while its intensity increases with the increase of the defect concentration [133].
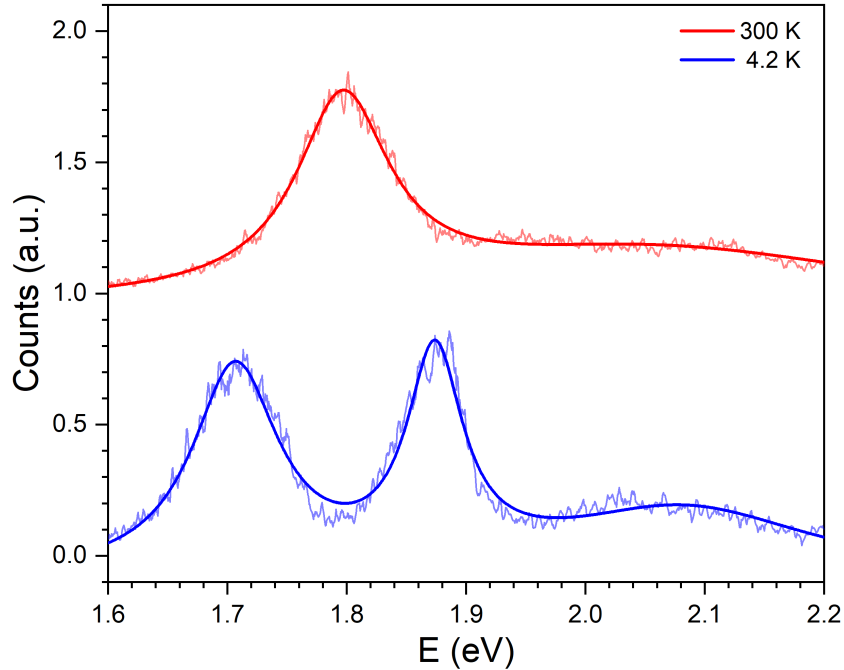
Figure 4.2: Normalized MoS_2 PL spectra taken at 300 K and 4.2 K.

PL maps taken at 4.2K, shown in Figure 4.1 f)-j), are used to determine the spatial distribution of A exciton energy with respect to the growth temperature T_G. Usually, the variations in A exciton energy and intensity can be correlated with morphological features, such as grain boundaries [134], but since samples shown in Figure 4.1 are monocrystals without evident grain boundaries, the inhomogeneous spatial distribution of A exciton energy is attributed to different defect concentrations arising from different growth conditions.

The correlation between defects and the X_B emission band was proven either by introducing additional defects [17, 125] or by correlating spatial fluctuations of the existing defect density and excitonic properties [12, 134]. From the A exciton energies at 4.2K (Figure 4.1 f-j), it is noticeable that samples with lower T_G value have more pronounced variations in the A exciton energy (Figure 4.1 f-h), while the samples grown at higher T_G have more homogeneous A exciton spatial distribution (Figure 4.1 i, j). Also, samples with higher defect concentration exhibit significant blueshift in the edge region.

Energy distribution of bound (X_B) and A excitons with respect to the growth temperature is shown in Figure 4.1 k)-o). All samples, except the one synthesised at the optimum growth conditions, show broad energy distribution for both excitons at 4.2 K. These histograms show the impact of the growth temperature on the optical properties in triangular monolayer MoS_2 samples [77, 135]. The binding energy of the bound exciton can be calculated from the histograms: E_b = 159, 155, 150, 150 and 169 meV for sample grown at 800°C, 825°C, 850°C, 875°C and 900°C, respectively. In the recent work [15], a shallow trap state with binding energy of 200 meV was identified using deep level transient spectroscopy (DTLS) technique and it was ascribed to the hybridised pairs of neighbouring sulphur vacancies.

Figure 4.3 a)-e) presents the intensity ratio of the X_B and A excitons. According to the study [133], the intensity of the bound exciton increases if more defects are created using the electron beam. In the case of CVD-grown MoS_2 samples, from the line profiles shown in insets, it can be observed that the intensity ratio of X_B and A excitons decreases with the increase of T_G, meaning that the defect concentration lowers as the growth temperature increases, which is in agreement with the KPFM analysis.

The sample synthesised at T_G = 900°C has uniform $I(X_B)/I(A)$ spatial distribution, except at the nucleation site at the centre of the triangle [136] and in the one vertex, since the vertex can be also an active site for nucleation [137]. Line profiles, shown in the insets, further confirm that the sample with the least amount of defects has homogeneous $I(X_B)/I(A)$, while all the other samples exhibit the same non-uniformity which can be also be correlated with the inhomogeneous spatial A exciton energy distribution (Figure 4.1 f-j).

Since both the KPFM and PL maps indicate a distinction between the sample edge and the sample interior, an additional analysis of the PL maps has been carried out. The triangular islands were tentatively divided in two parts: interior and the edge, as shown in Figure 4.1 f)-j) - the interior is inside the region denoted with black lines, while the edge region is calculated by subtracting the entire data of an island and the interior part. For each pixel in the PL map, the correlation between A exciton intensity and energy was done and the results are shown in Figure 4.3 f)-j). The intensity of A exciton is higher in the interior part than on the edges, which indicates better crystal quality and lower defect concentration. Sample with T_G = 850°C has different behaviour from the other samples, due to the blueshifted region in the interior. The region encloses the nucleation centre which has increased concentration of Mo-precursors, namely oxides. This gives rise to a higher defect concentration around the nucleation centre which changes the material's properties. In all the other samples, the energy distribution is broader on the edges, with respect to the interior. The drop in intensity is accompanied with the blueshift in A exciton energy, apart from the sample with T_G = 900°C, where slight redshift is observed, due to the vertex discussed in the previous paragraph. Nevertheless, these results suggest
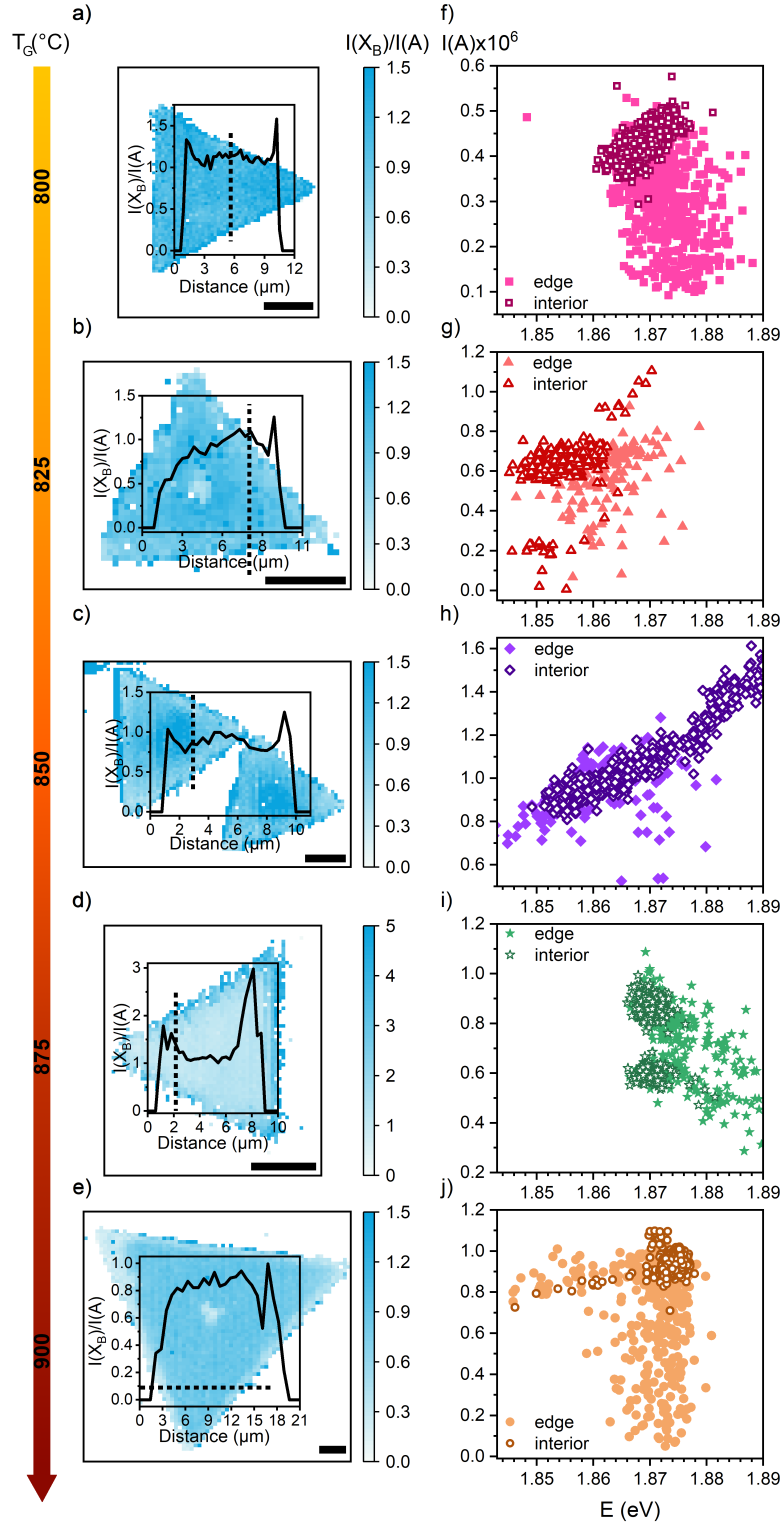
Figure 4.3: Left column: Ratio of bound (X$_B$) and A exciton intensities for different growth temperatures T$_G$. Insets show intensity ratio line profiles denoted with dashed black line. Scale bar is 5 μm. Right column: The scattering plots show correlation between intensity of A exciton and its energy for two distinct regions denoted with black lines shown in Figure 4.1 f)-j).

that in-gap defect states modify sample's bandgap [134].

Again, further analysis of differences between the central part and the edges was conducted on two samples with $T_G = 800°C$ and $T_G = 900°C$. As already discussed, the sample with higher defect concentration is synthesised at lower growth temperature and it has position-dependent electronic and optical properties. Power- and temperature-dependent measurements were taken at two positions on these two islands, denoted with "•" marks on Figures 4.1 f) and j): at the edges of the islands and close to the island centres, avoiding the nucleation site.

4.2.1 Power-dependent measurements

In order to investigate the nature of the each emission line in the PL spectra, shown in Figure 4.2, I've conducted power-dependent PL measurements. Under the assumption that intensity of A exciton (I(A)) linearly depends on the excitation power, as was already proven in Section 3.2.2, the power-dependent measurements of the bound exciton intensity (I(X_B)) can be related to I(A) with following relation: $I(X_B) \sim I(A)^\alpha$. A higher α value ($0.5 < \alpha < 1$) suggests a higher defect concentration and is accompanied by a steeper increase of the PL intensity [77]. Deeper defect levels have lower α value and these states saturate at lower excitation powers [138].
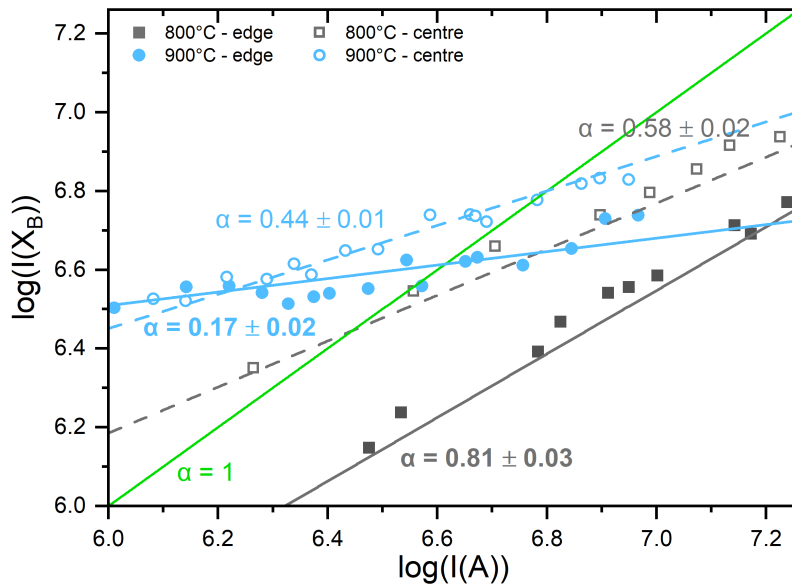
Figure 4.4: Power-dependent measurements taken at 4.2K. Logarithmic plot of the bound exciton intensity, I(X_B), as a function of the intensity of A exciton I(A). Lines are power-law fits and the green solid line $\alpha = 1$ is included for comparison.

The excitation power is changed over three orders of magnitude and the I(A) has linear dependence on the excitation power, while the I(X_B) saturates (Figure 4.4). This indicates that the new emission line in caused by the lattice defects, which induce localized

in-gap states and trap excitons, as observed in other studies [12, 133, 139]. Also, these results show that the sample with $T_G = 900°C$ has lower defect concentration with larger binding energy, in agreement with analysis of PL and KPFM maps.

4.2.2 Temperature-dependent measurements

Semiconductor's properties are modulated with temperature due to the electron-phonon coupling [140]. Up to 110 K, the acoustic phonons dominate the entire modification of all spectral features [141–144]. The strength of electron-phonon coupling can be derived from the temperature dependence of spectral features, such as intensity and energy.

Temperature-dependent point measurements were taken in the same points as the power-dependent measurements, in steps of 10 K, ranging from 4.2 K to 300 K. Figure 4.5 shows temperature dependence of PL spectra taken at four different spots: 800°C – edge (Figure 4.5 a)), 800°C – centre (Figure 4.5 b)); 900°C – edge (Figure 4.5 c)) and 900°C – centre (Figure 4.5 d)). It can be seen that the intensity of the bound exciton emission line at ≈ 1.8 eV (≈ 1.7 eV) for $T_G = 800°C$ (900°C) decreases as the temperature increases to 130K (90K).
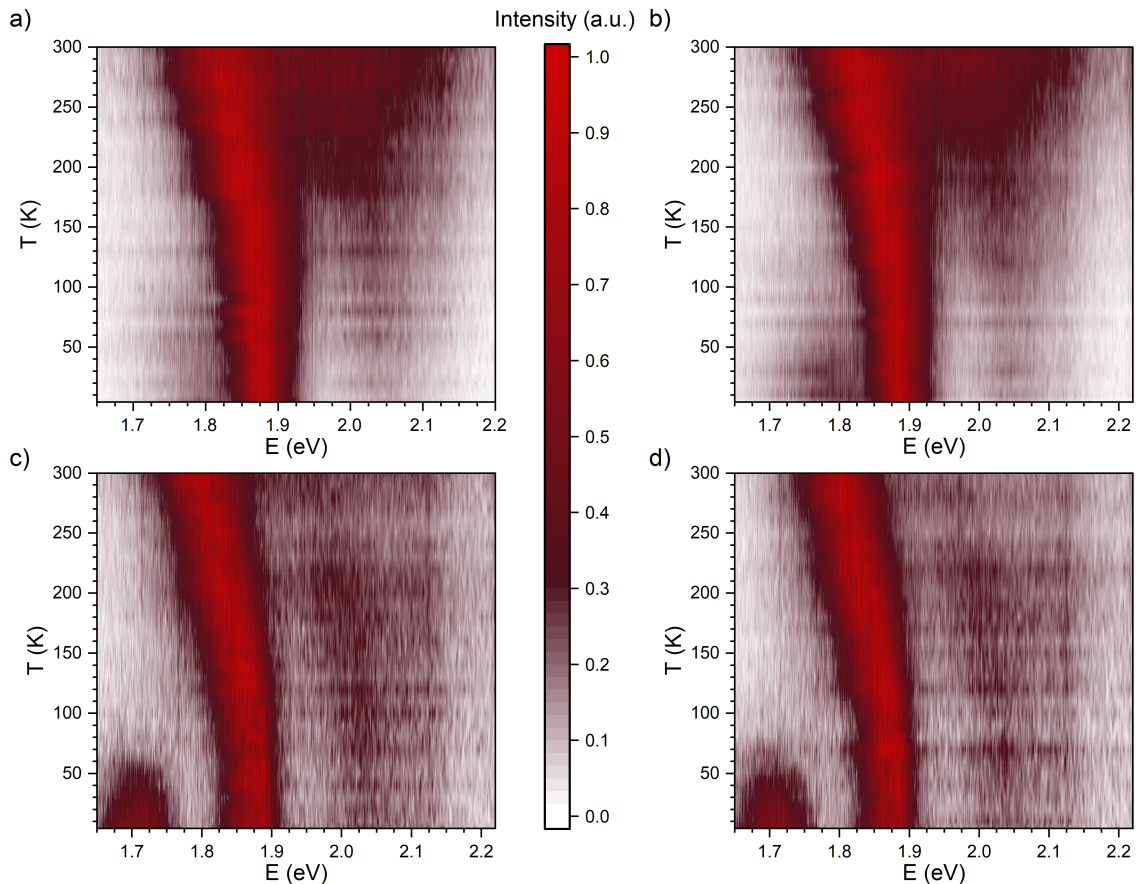
Figure 4.5: Temperature dependent measurements. a) $T_G = 800°C$ - edge, b) $T_G = 800°C$ - centre, c) $T_G = 900°C$ - edge, d) $T_G = 900°C$ - centre.
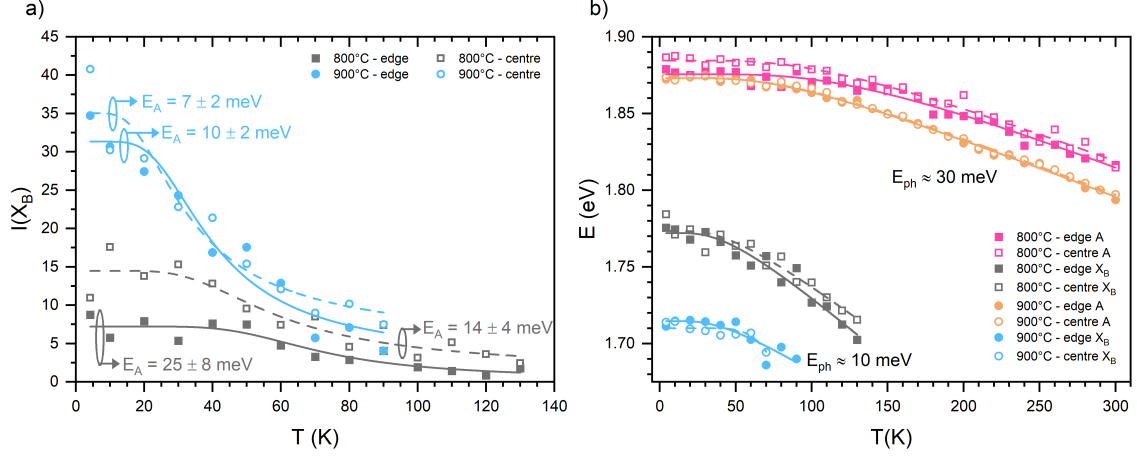
Figure 4.6: a) Bound excitons' normalized intensity ($I(X_B)$) as a function of temperature T and corresponding fits to the data. b) Temperature dependence of bound and A exciton energies.

At low temperatures, neutral excitons are loosely bound to defects in the material and they can be easily thermally perturbed. The thermal stability of this complex depends on the activation energy, which can be calculated from the temperature dependence of the normalized bound exciton intensity (Figure 4.6 a) using the equation [145]:

$$I(X_B)(T) = \frac{I_0}{1 + C \cdot e^{-E_A/k_B T}},\tag{4.1}$$

where $I(X_B)$ is the bound exciton intensity, C is the process rate parameter and E_A is the thermal activation energy. Bound exciton is less stable and it dissociates at lower temperature if its activation energy is lower. In the analysed samples, the bound exciton with the lowest activation energy is located in the centre of the sample with $T_G = 900°C$. All calculated thermal energies are lower than their binding energies (160 - 170 meV, as calculated from histograms in Figure 4.1), which means that the bound excitons do not directly thermally activate into the neutral exciton continuum [146]. Possible explanation for this is the strong electron-phonon coupling between electrons and acoustic phonons.

Mainly, the bandgap in semiconductors redshifts with the increase of the temperature, due to the electron-phonon interactions. For temperatures up to $\approx 100K$, the redshift of bound excitons is larger than the shift of neutral excitons (Figure 4.6 b). The redshift is also more pronounced in the sample with higher defect concentration, indicating stronger electron-phonon coupling [147]. The phonon energy can be calculated by fitting the data to a modified Varshni equation [148]:

$$E(T) = E_0 - S\left[\coth\left(\frac{E_{ph}}{2k_B T}\right) - 1\right],\tag{4.2}$$

where E_0 is the bandgap energy at 0K, E_{ph} is the phonon energy, k_B the Boltzmann constant, T temperature and S is the Huang-Rhys factor, a measure of the electron-

phonon coupling strength. For A excitons, the calculated phonon energy is ~ 30 meV, while for the bound excitons it's equal to 10 meV - with the exception of 900°C - centre, which did not yield a reliable fitting result, because there are not enough data points. It was shown in a study done by Lee et al. [149] that longitudinal acoustic phonons in TMDs have strong electron-phonon coupling and their energies are in the range of 10-25 meV.

4.2.3 Charge carriers' dynamics dependence on the growth temperature

In order to understand the influence of intrinsic defects on the relaxation dynamics in monolayer triangular MoS_2 samples, I conducted microscopic TA measurements. Recent theoretical work [150–152] showed that, due to the presence of defects in monolayer TMDs, the direct recombination timescale is greatly reduced since defects create in-gap states which, in turn, generate new relaxation channels and thus significantly shorten the recombination timescales. These defect-assisted relaxation processes are non-radiative and are the main reason behind the low quantum yield in monolayer TMDs [112, 153, 154].
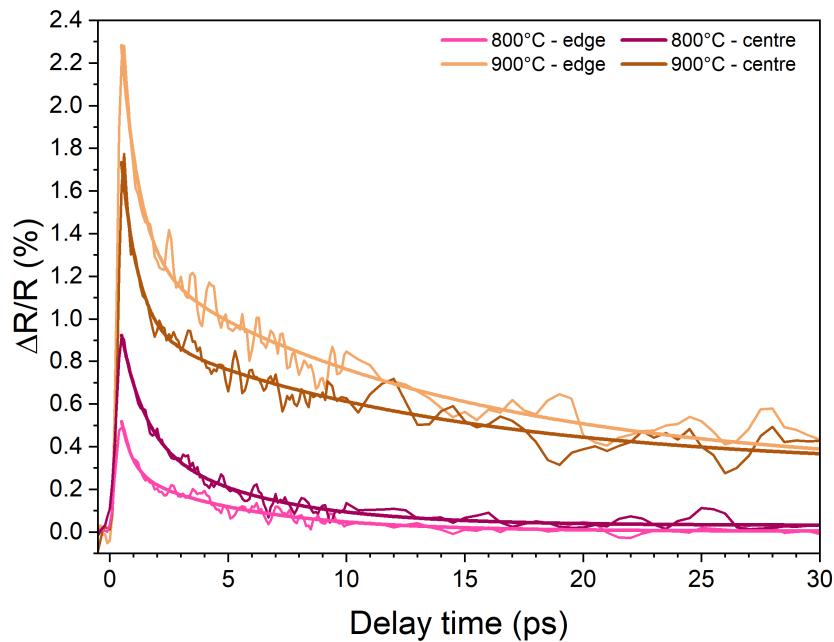
Figure 4.7: Relaxation dynamics of samples grown at 800°C (900°C) at 1.82 (1.8) eV probe photon energy measured by ultrafast TA microscopy in the samples' edge and centre.

The samples were pumped at 2.4 eV, with ≈ 0.5 eV excess energy with respect to the A exciton resonance. Representative TA dynamics for sample grown at 800°C (900°C) at the A exciton resonance at 1.82 (1.80) eV probe photon energy for a fixed excitation fluence are shown in Figure 4.7. The relaxation dynamics is fitted on biexponential decay

Table 4.1: Relaxation dynamics fitting parameter values for 1L CVD-grown MoS_2 samples.

| | 800 °C | | 900 °C | |
	centre	edge	centre	edge
A_1 (a.u.)	0.77 ± 0.05	0.7 ± 0.1	1.6 ± 0.1	1.9 ± 0.2
τ_1 (ps)	1.0 ± 0.1	0.49 ± 0.08	0.73 ± 0.07	0.79 ± 0.07
A_2 (a.u.)	0.48 ± 0.06	0.31 ± 0.02	0.68 ± 0.02	1.03 ± 0.03
τ_2 (ps)	4.9 ± 0.5	5.1 ± 0.4	13 ± 1	13 ± 1

function:

$$y(t) = y_0 + A_1 e^{(-\tau_1/t)} + A_2 e^{(-\tau_2/t)}, \tag{4.3}$$

where τ_1 and τ_2 represent faster and slower decay times, respectively, and A_1 and A_2 represent related amplitudes. Values obtained for these parameters are listed in Table 4.1. Since the time constants do not show significant pump fluence dependence (Figure 4.8 a), we can conclude that the main reason for different timescales is caused by relaxation processes, and not heat dissipation to the crystal lattice induced by the photoexcitation process [155, 156].
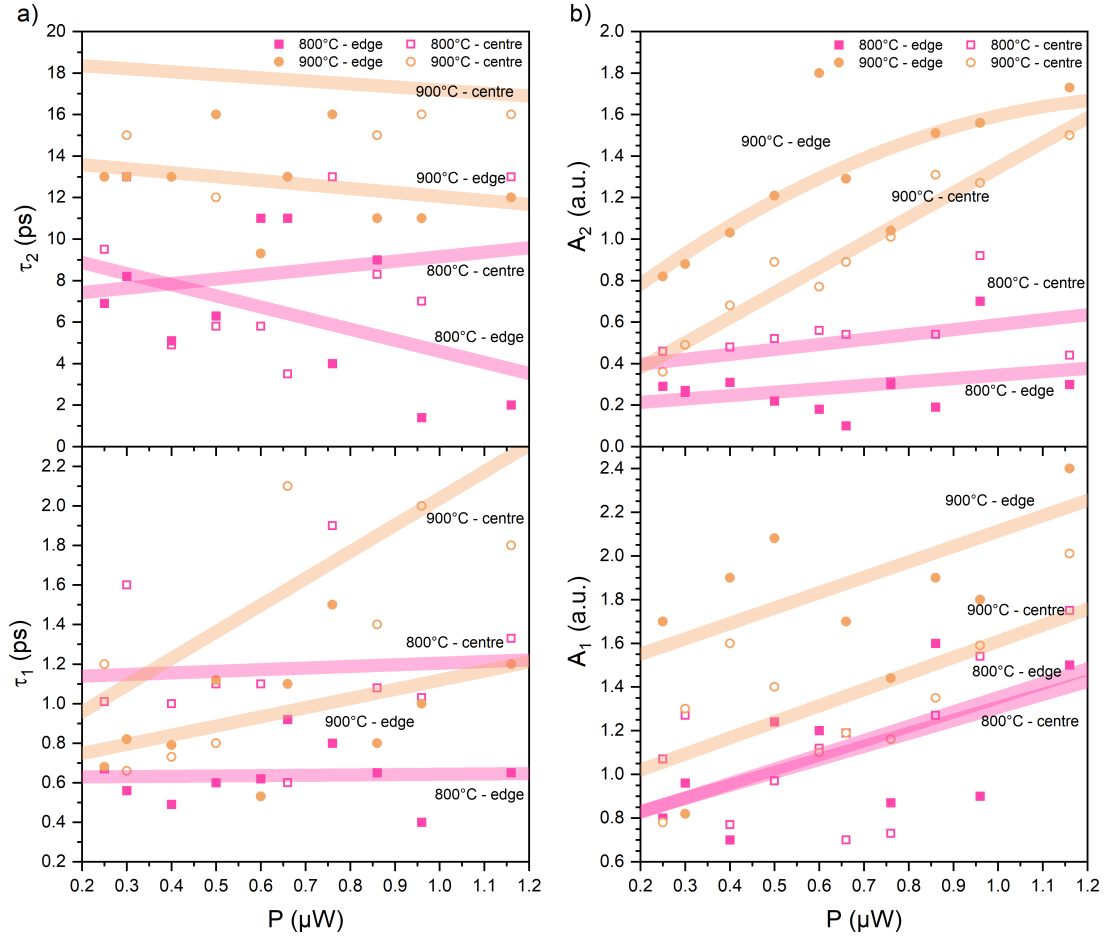
Figure 4.8: Fitting parameters time constants τ (a)) and amplitudes A (b)) of the biexponential decay function dependence on excitation power. Thick lines are eye guidelines.

In all four positions, the fast decay component is a (sub)picosecond process which can be ascribed to the carrier intraband cooling from high-energy state into the conduction band minimum. The cooling process involves energy transfer from hot carriers to lattice vibrations by carrier-phonon interaction [157, 158] and it is associated with a rapid reduction of free electrons in highly excited states [159]. Research done by Cunningham et al. in [160], using time-resolved terahertz (THz) spectroscopy, demonstrated a photoinduced increase in conductivity with the same dynamics, confirming that the mobile charge carriers produce the fast decay, and not excitons. In another study [161] it was shown that only in the near-resonant excitation, the fast decay component has a certain fluence dependence. In the case of WS$_2$, in the resonant case, it was shown that the increase of the fast decay component is caused by the increase in fluence. In the off-resonant case [162], such as ours, there was no evident correlation between the excitation fluence and the fast decay component, (Figure 4.8 a). In a low carrier density regime, this implies that the dynamics of the photocarriers are independent of the carrier density. Since the values of τ_1 is similar for both samples, this indicates that the defect states which emerge due to the different growth temperatures, do not influence the cooling process of hot carriers in monolayer MoS$_2$ samples.

Slower decay component, which is about tens of ps long, is associated with the exciton recombination. In this process the localized in-gap defect states trap the photoexcited paticles and shorten their lifetimes [160, 163]. In the sample with lower defect concentration, the value of τ_2 is higher than in the sample with T$_G$ = 800°C and it is position independent, confirming again its homogeneity. Different values of τ_2 in these two samples may imply that there are different types of defects. This can be correlated with the low-temperature PL measurements, where it was established that these two samples have defects with different binding energies.

Regarding the amplitudes of decay components, the A_1 component is smaller for the sample with T$_G$ = 800°C. This may be caused by the reduced number of carriers which end up at the bottom of the conduction band, because most of them are scattered to the shallow defect level due to the increased defect concentration [164], which results in lower TA amplitude. Because exciton formation and electron-phonon scattering occur in the same timescales [159], increased photocarrier scattering results in a less efficient exciton formation process, thus reducing the overall TA amplitudes.

The amplitude of the slow decay component (A_2) gives information about the intensity of A exciton relaxation from the conduction band minimum. For sample with lower defect concentration this parameter shows mild saturation with the increase of the excitation fluence (Figure 4.8 b), indicating the saturation of defects' states under certain excitation fluence. For the sample with higher defect concentration, the parameter A_2 does not have significant fluence dependence, which means that the electrons either radiatively recombine with the holes in the valence band maximum or they are trapped in the shallow

defect states. If the electrons are trapped, than they recombine non-radiatively and as a result the amplitude of the radiative process decreases. In the sample with $T_G = 800°C$, the value of A_2 is lower at the edge than in its centre, due to the higher defect concentration. These results are consistent with the power-dependent PL measurements conducted at 4.2 K, which showed sublinear trend of the X_B intensity and from which was concluded that sample wiht $T_G = 800°C$ has higher defect concentration.

4.3   Conclusion

In this Chapter, I have shown how the intrinsic defects in CVD-grown 1L MoS_2 monocrystals modfy their electronic and optical properties. The nature and concentration of intrinsic defects can be tuned by controlling growth temperature during the CVD synthesis process. KPFM maps showed that the work function is inhomogeneous in samples synthesised at lower temperatures, $T_G = 800 - 850°C$ - namely the edge region has higher value of the work function. This indicates that the electronic structure changes due to the higher defect concentration. This behaviour is not observed in samples with higher T_G values: 875 and 900°C, in which the work function is homogeneous throughout the whole area of the island. Regarding the optical properties, PL maps taken at 4.2K showed that samples synthesised at lower T_G (800 - 850°C) have inhomogeneous spatial distribution of A exciton energy. Since all synthesised samples are monocrystals, with no evident cracks or grain boundaries, these inhomogenities can be attributed to intrinsic defects originated from different values of T_G. In agreement with the KPFM analysis, samples synthesised at lower growth temperatures have non-uniform PL response, in terms of both energy and intensity, due to the higher defect concentration. The optical properties of the samples grown at higher T_G are homogeneous and uniform. Even though the spatial distribution of A exciton energy is homogeneous in the sample with $T_G = 875°C$, the overall energy distributions of bound (X_B) and A excitons are wider than those in the sample with $T_G = 900°C$. In addition to mentioned inhomogeneous optical properties, charge carriers in the sample with higher defect concentration ($T_G = 800°C$) have shorter and position-dependent lifetimes.

In the next Chapter I will show how optical properties in monolayer MoS_2 samples can be modified by introduction of foreign atoms in the crystal lattice via alloying. Also, I will demonstrate how slightly different growth conditions can lead to drastically different materials.

Chapter 5

Tailoring MoS$_2$ properties via defect engineering

In this Chapter, I describe the influence of alloying on optical properties in monolayer TMDs. Introduction of foreign atoms in a material changes its electronic and optical properties. It is possible even to introduce long-range magnetic order in non-magnetic materials [165–168]. It was shown that the resulting material depends on the growth temperature [66, 67, 169, 170]. This indicates that with the control of growth parameters, one can deterministically synthesise either alloys or different types of heterostructures.

5.1 Alloying

As mentioned in Chapter 1, the simplest way of inducing novel properties in a material is by introduction of foreign atoms in its crystal lattice. Alloying MoS$_2$ with W-atoms (and vice versa) is somewhat easy to achieve, since Mo and W are isoelectronic atoms - meaning that they have the same number of electrons in their outmost shell, while the only difference is in their mass.

Optical micrograph of the CVD-grown monolayer Mo$_{1-x}$W$_x$S$_2$ alloy is shown in Figure 5.1 a). The PL maps shown in panels c) and d) are taken in the area indicated with the dashed black square, while green and red points denote points where power-dependent measurements were done. Rather large nucleation centre is visible in the centre of the island. The PL spectra (Figure 5.1 b) taken at two points, denoted with green (centre) and red (edge) dots in Figure 5.1 a), show that there are two components: A exciton (lines 1.1 and 2.1) and a trion (lines 1.2 and 2.2). The spectrum taken near the edge is slightly blueshifted ($\sim$ 15 meV) with respect to the one taken in the centre. Similar behaviour was observed in the sample with higher defect concentration in the previous Chapter. In the case of an alloy, the blueshift could be caused either due to the existence of intrinsic defects or due to the strain which foreign atoms induce in the host material [171].
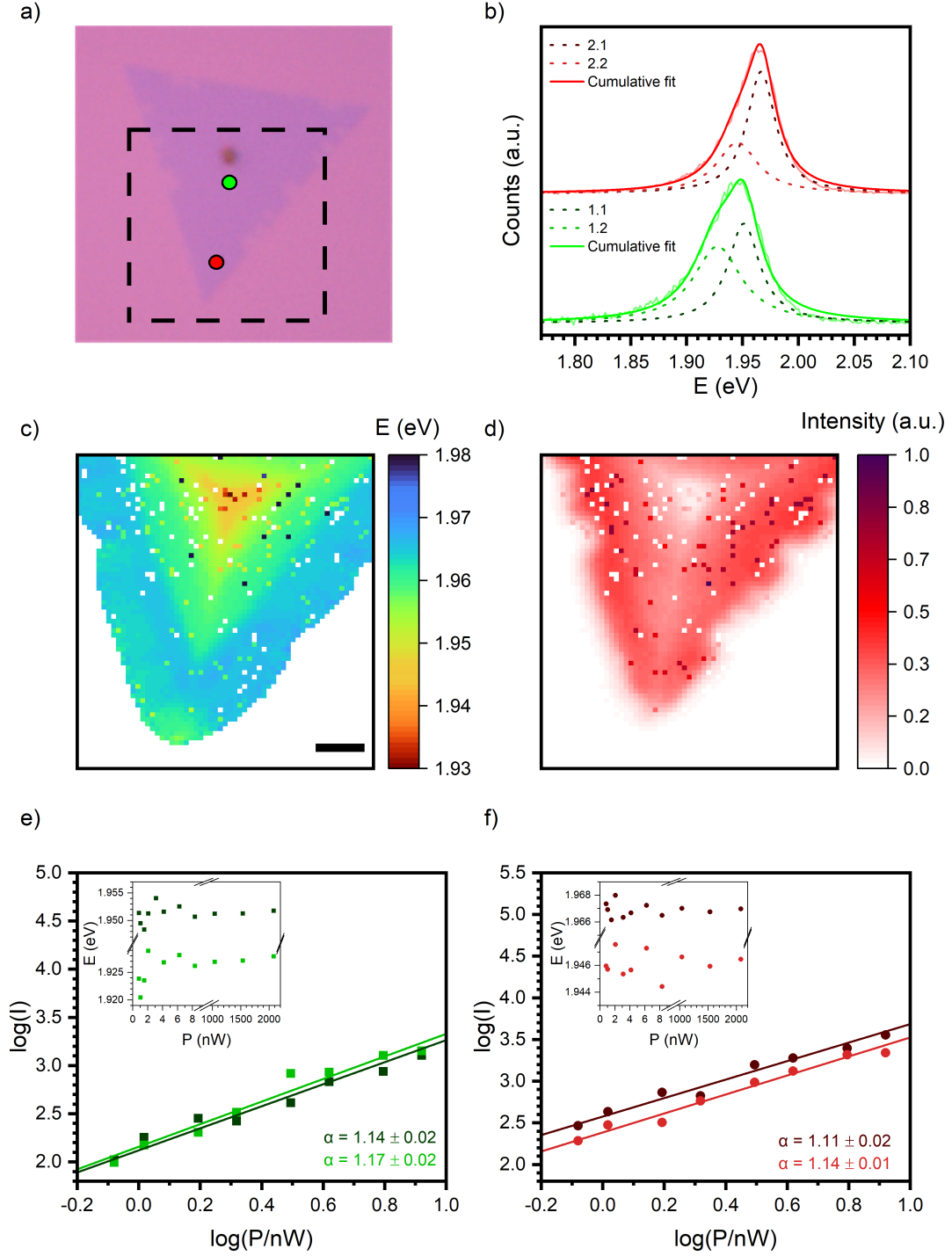
Figure 5.1: a) Optical micrograph of the CVD-grown monolayer $Mo_{1-x}W_xS_2$ alloy. Dashed black square denotes area of PL maps shown in panels c), d). Green and red circles denote points on which power-dependent measurements were done. b) PL spectra taken at two points, marked with green and red circle on the optical micrograph. Corresponding fit components are shown in dashed lines. Spatial distribution of A exciton energy (c) and intensity (d). Scale bar is 2 μm. e) and f) PL intensity dependence on laser power with corresponding coefficient for each fitting component. Insets in both graphs show dependence of A exciton's and trion's energies on incident laser power.

Spatial distributions of A exciton energy and intensity are shown in Figure 5.1 c) and d). The A exciton energy blueshifts radially from the centre towards the edge, while its intensity increases. This behaviour can be attributed to the higher W-concentration, as will be explained later.

In order to determine the nature of each PL component, I have conducted power-dependent measurements on points indicated in the Figure 5.1 a). The measurements are shown in Figure 5.1 e) and f) with corresponding fit coefficients. The insets in graphs indicate the power-dependence of A exciton's and trion's energies. Both of those emission lines have linear power-dependence, confirming their excitonic nature.
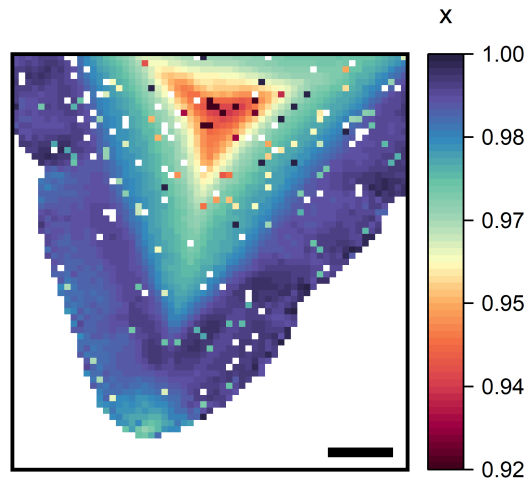
Figure 5.2: Spatial distribution of W-composition (x) determined from A exciton energy of the alloy. Scalebar is 2 μm.

Composition of an $Mo_{1-x}W_xS_2$ alloy can be tentatively calculated from the A exciton energy. The bandgap energy of an alloy is smaller than the linear combination of its components, due to the bowing effect of the lowest unoccupied molecular orbital (LUMO) energy level [53]. In the highest occupied molecular orbital (HOMO) energy level, each metal atom contributes with its d_{xy} and $d_{x^2-y^2}$ orbitals. Because of this, their contribution to the HOMO energy level is the same and with the increase of the W-concentration, the HOMO energy level increases linearly. In case of the LUMO energy level, the orbital contributions of MoS_2 and WS_2 are not the same: only d_{z^2} needs to be considered for MoS_2, while for WS_2 orbitals $d_{xy}, d_{x^2-y^2}$ and d_{z^2} need to be included. And since the LUMO energy for WS_2 is higher than in MoS_2, the total contribution of WS_2 to LUMO energy level is smaller. With the increase of W-concentration, the increase of LUMO energy level is not linear, but smaller, and this results in the bowing effect [53]. Without considering factors such as strain or defects, the bandgap of the $Mo_{1-x}W_xS_2$ alloy is equal to:

$$E_{\text{alloy}} = (1-x)\,E_{MoS_2} + x \cdot E_{WS_2} - bx\,(1-x), \tag{5.1}$$

53

where $E_{MoS_2} = 1.810$ eV and $E_{WS_2} = 1.968$ eV are the bandgaps of our CVD-grown MoS$_2$ and WS$_2$ monolayers. The coefficient b is the bowing factor, and it is equal to $b = (0.25 \pm 0.04)$ eV [53]. The spatial map of W-composition (x) is shown in the Figure 5.2. The alloy is in its majority constituted of WS$_2$, while the central part has small MoS$_2$ contributions (less than 10%). Higher tungsten concentration leads the the blueshift of the PL spectrum, but also it increases its intensity, as indicated previously in Figures 5.1 c) and d).
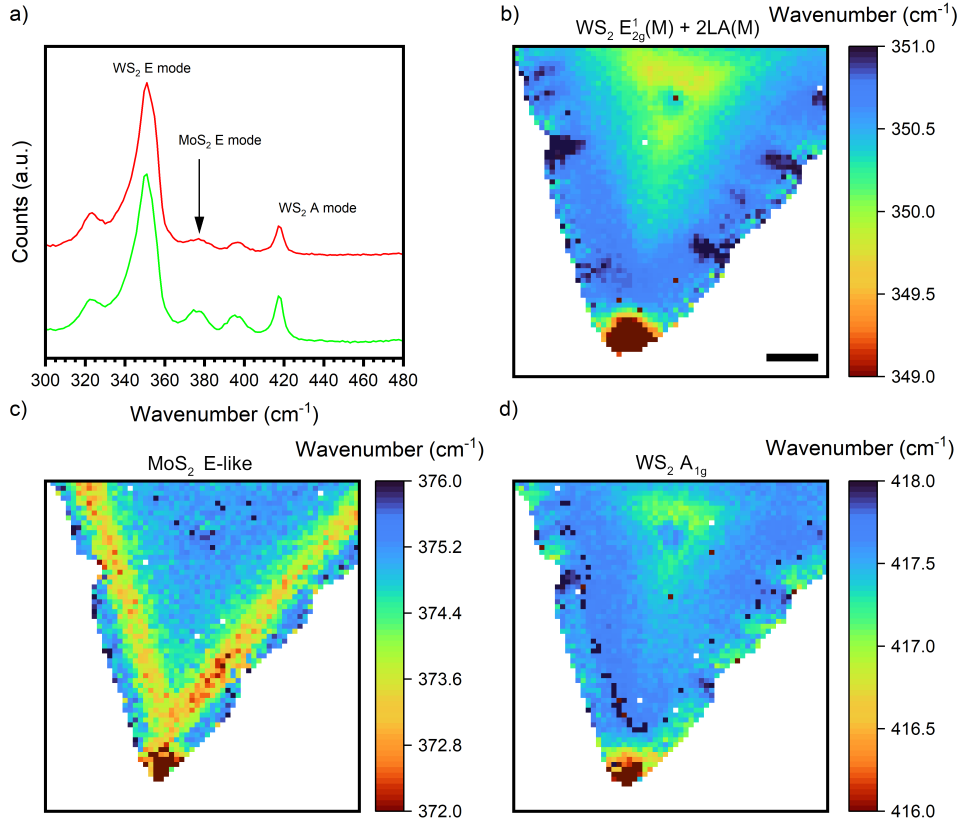
Figure 5.3: a) Raman spectra taken in the centre (green) and on the edge (red) of the monolayer island. Spatial distribution of Raman modes' frequencies: b) WS$_2$ E$_{2g}^1$(M) + 2LA(M) mode, c) MoS$_2$ E-like mode and d) WS$_2$ A$_{1g}$ mode. Scalebar is 2μm.

Since the alloy has two different metal atoms, which are randomly distributed in a material, the vibrational modes are modified with respect to the alloy's components. The frequency of Raman modes are shifted, while the spectral lines are asymmetrical and broader [91, 172]. Raman spectra (Figure 5.3 a) taken in the centre (green) and near the edge (red) show that the island has both WS$_2$ and MoS$_2$ vibrational modes, with modified frequencies. The modes at ~ 323 cm^{-1}, ~ 344 cm^{-1}, ~ 351 cm^{-1} and ~ 417 cm^{-1} belong to monolayer WS$_2$, namely: 2LA(M)-E$_{2g}^2$(Γ), E$_{2g}^1$(M), 2LA(M) and A$_{1g}$ while the one at ~ 375 cm^{-1} corresponds to modified E$_{2g}^1$ mode in MoS$_2$ and ~ 396 cm^{-1}, which is present only for composition values greater than $x > 0.7$, is attributed to the lattice perturbation caused by S vacancies [173–175]. Similar vibrational mode associated with disorder and

localized strain is observed in $WS_{2(1-x)}Se_{2x}$ monolayer alloy with $x > 0.6$ [176–178], but not in $MoS_{2(1-x)}Se_{2x}$ alloy [54, 179].

The composition of an alloy can also be determined from the frequencies of Raman modes [172]. In the cited literature it was shown that for weak alloying ($x < 0.2$), there is no significant difference between pure monolayer MoS_2 and $Mo_{1-x}W_xS_2$ Raman spectra. This implies that for weak alloying, the Raman spectroscopy is not suitable technique for composition determination. When the W-concentration is higher ($x \approx 0.4$), new Raman mode emerges, around 350 cm^{-1}, which is attributed to the linear combination of longitudinal acoustic 2LA(M) and inactive A_2'' optical mode. On the other hand, the MoS_2 E_{2g}^1 mode redshifts (from ≈ 383 cm^{-1}), while the A_{1g} mode blueshifts from ≈ 403 cm^{-1} until it merges with the WS_2 A_{1g} mode (~ 418 cm^{-1}). In our case of monolayer $Mo_{1-x}W_xS_2$ alloy, the MoS_2 E-like mode has frequency of 375 cm^{-1}, and the corresponding composition is equal to $x \approx 0.8$, which is less than one calculated from the A exciton energy.

The spatial distribution of frequencies for WS_2 E_{2g}^1(M) + 2LA(M) modes, MoS_2 E-like mode and WS_2 A_{1g} are shown in Figure 5.3 b)-d), respectively. The E_{2g}^1(M) + 2LA(M) mode blueshifts with the increase of W-concentration (Figure 5.2), while the MoS_2 E-like mode (Figure 5.3 c) redshifts, which is in agreement with previous studies [172, 180].

5.2   Heterostructures

By controlling CVD growth conditions, especially the growth temperature, it is possible to synthesise both v-HS and l-HS [11, 66, 67, 170, 181, 182]. In Chapter 2, by comparing the graphs corresponding to the alloy (Figure 2.3 b) and heterostructure growth procedures (Figure 2.4), the prolonged second stage growth at lower temperature ($\sim 775°C$) caused the WS_2 growth, both laterally and vertically on the existing MoS_2 islands. The monolayer alloy sample, analyzed in the previous section, was synthesised at a higher growth temperature and rapidly cooled afterwards. In this section, a complex WS_2/MoS_2 heterostructure is investigated with room-temperature Raman and PL measurements.

Optical micrograph of the CVD-grown heterostructure is shown in Figure 5.4 a). Along the vertical line PL and Raman spectra were acquired and shown in Figure 5.4 b) and c), respectively. Dashed square denotes area of PL and Raman maps shown in Figure 5.4 d). The optical micrograph shows that the island in its central part has monolayer thickness (1L), while near the edge darker contrast suggests that island has at least two layers and the very edge has again monolayer thickness.

Normalized PL spectra (Figure 5.4 b)) show the change of island's optical response along the line denoted on the optical micrograph in panel a). On the very edge, the optical response belongs to the monolayer WS_2, with one dominant emission line at $\sim$1.95 eV. On the multilayer part, there are two prominent peaks, $\sim$1.82 eV and $\sim$2.0 eV, while the third one at 1.47 eV has much lower intensity. In the central part, the PL signal has again two
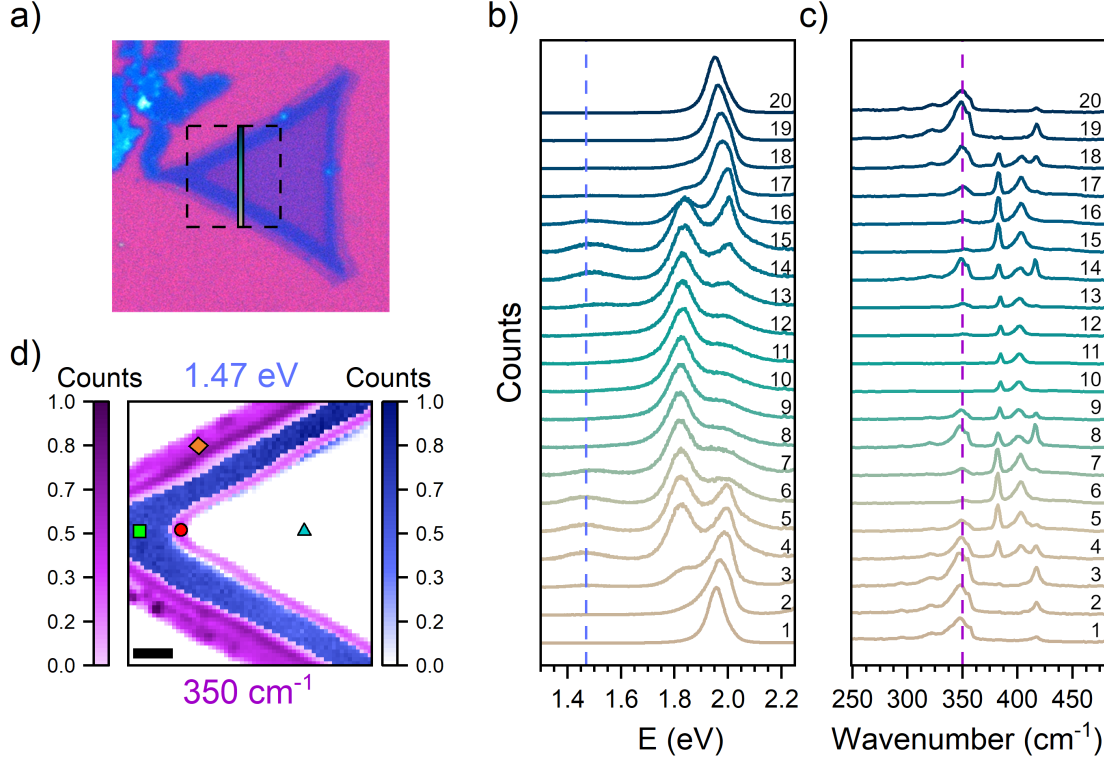
Figure 5.4: a) Optical micrograph of the CVD-grown heterostructure. For 20 points along the vertical line PL and Raman spectra were extracted and shown in panels b) and c), respectively. Dashed square denotes area of PL and Raman maps shown in panels d). b) PL spectra extracted from a line shown in a). Vertical dashed line is set at 1.47 eV. c) Raman spectra extracted from a line shown in a). Vertical dashed line is set at 350 cm^{-1}. d) Spatial map of PL (Raman) spectra counts at 1.47 eV (350 cm^{-1}) shown in blue (purple) color. Green, red, cyan and orange shapes denote points at which power-dependent measurements were taken. Scalebar is 2 μm.

peaks, ∼1.84 eV and ∼2.0 eV. The high energy peaks which are dominant in all spectra belong to excitons in MoS_2 and/or WS_2. The additional emission which is observed only in the multilayer part is attributed to the interlayer exciton (ILE). Its spatial distribution is shown in Figure 5.4 d) in blue color.

Interlayer exciton is formed when a hole resides in one layer of a material and the electron is in the second. This exciton has larger radius and it's less stable then the common intralayer exitons, such as already analysed A and B excitons in monolayer materials. ILE are typically observed in multilayer CVD grown samples, while their existence in mechanically stacked v-HS depends on the interaction between exfoliated layers [183].

Raman spectra extracted from the same points as PL ones are shown in Figure 5.4 c). The vibrational modes evolve from pure WS_2 (1. and 2. spectra), across v-HS of WS_2 and MoS_2 (3., 4. and 5. spectra), multilayer MoS_2 (6. and 7. spectra), again v-HS of WS_2 and MoS_2 (8. and 9. spectra) and finally, in the central part there the Raman spectra show modes of monolayer MoS_2 (10. and 11. spectra). Unlike the alloy analysed in the

previous section, in this island there is no significant shift in the modes' frequencies, since both MoS_2 and WS_2 Raman A modes are visible, suggesting that this is indeed a sample with both lateral and vertical heterostructures. The MoS_2 vibrational modes shift from 384.5 cm^{-1} and 401.6 cm^{-1} in the monolayer region to 382.1 cm^{-1} and 403.1 cm^{-1}, which is expected in transition from 1L to multilayer. Along the shift in frequencies, the modes' intensities also increase with the increasing number of layers.

The Raman map (Figure 5.4 d), purple color) shows the spatial distribution of the WS_2 E mode. The step size was set to 0.2 μm and the laser spotsize in focus was equal to 300 nm. The overlap with the spatial distribution of ILE indicates that the WS_2 is also present in multilayer edge, meaning that besides the l-HS, this island also has v-HSs on the outer and inner edge of the multilayer part.
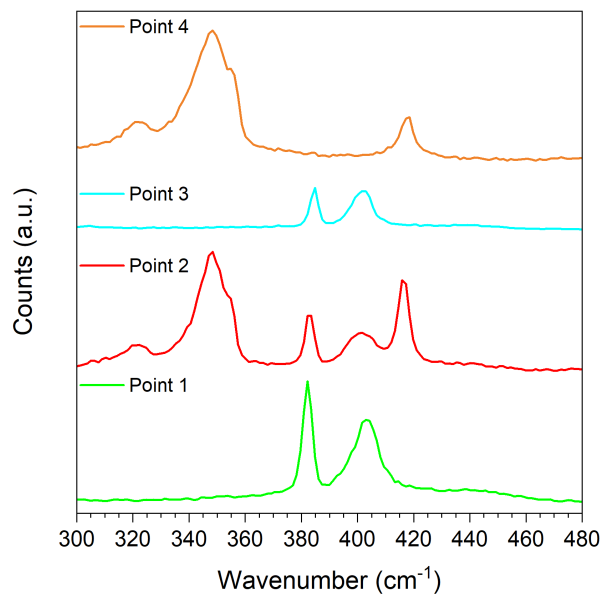
Figure 5.5: Raman spectra taken at different points which are indicated in the Figure 5.4 d). Spectra were fitted using Lorentzian functions and the fitting parameters are presented in Table 5.1.

Point measurements were conducted on four locations indicated in the Figure 5.4 d). Point 1 is taken on the multilayer part (green square in Figure 5.4 d), where only MoS_2 modes are present (Figure 5.5 green line). Point 2 is located on the inner edge of the multilayer part (red circle in in Figure 5.4 d) where all of MoS_2 and WS_2 Raman modes are visible (Figure 5.5 red line). Point 3 is located in the central (cyan triangle in Figure 5.4 d) part, where only MoS_2 modes are present (Figure 5.5 cyan line). And finally, point 4 is located on the monolayer edge (orange rhombus in Figure 5.4 d), where only WS_2 vibrational modes are present (Figure 5.5 orange line). The normalized Raman spectra were fitted using Lorentzian function and the results are shown in Table 5.1.

The frequency difference of MoS_2 A_{1g} and E_{2g}^1 modes in point 1 is equal to ~ 21 cm^{-1}, which corresponds to the bilayer MoS_2 [184]. On the other, the frequency difference of

Table 5.1: Fitting parameters for Raman spectra in TMD heterostructure.

Location	Vibrational mode	Frequency (cm^{-1})	FWHM (cm^{-1})	Intensity (a.u.)
Point 1	MoS$_2$ E$_{2g}^1$	382.13 ± 0.03	3.74 ± 0.08	3.16 ± 0.05
	MoS$_2$ A$_{1g}$	403.10 ± 0.07	11.2 ± 0.3	6.4 ± 0.1
Point 2	WS$_2$ E$_{2g}^1$ (M)	320.5 ± 0.6	17 ± 2	2.3 ± 0.2
	WS$_2$ 2LA(M)	347.7 ± 0.1	10.6 ± 0.4	8.8 ± 0.3
	WS$_2$ E$_{2g}^1(\Gamma)$	354.4 ± 0.1	2.7 ± 0.7	0.6 ± 0.1
	MoS$_2$ E$_{2g}^1$	382.88 ± 0.07	2.7 ± 0.3	1.17 ± 0.07
	MoS$_2$ A$_{1g}$	401.4 ± 0.3	11.2 ± 0.9	2.9 ± 0.2
	WS$_2$ A$_{1g}(\Gamma)$	416.41 ± 0.07	4.7 ± 0.2	3.0 ± 0.1
Point 3	MoS$_2$ E$_{2g}^1$	384.49 ± 0.04	2.8 ± 0.1	0.82 ± 0.03
	MoS$_2$ A$_{1g}$	401.61 ± 0.08	8.3 ± 0.2	2.33 ± 0.05
Point 4	WS$_2$ E$_{2g}^1$ (M)	321.2 ± 0.6	24 ± 2	4.6 ± 0.4
	WS$_2$ 2LA(M)	347.5 ± 0.1	14.0 ± 0.4	12.7 ± 0.4
	WS$_2$ E$_{2g}^1(\Gamma)$	355.5 ± 0.1	2.8 ± 0.6	0.8 ± 0.2
	WS$_2$ A$_{1g}(\Gamma)$	417.6 ± 0.2	6.5 ± 0.5	1.9 ± 0.1

the same modes taken at point 3 is ∼17 cm^{-1}, indicating that the central part of the island is monolayer MoS$_2$ [184]. It is known from the literature [184] that the frequency difference of MoS$_2$ modes increases with the increasing number of layers. Also, with the increasing thickness, the FWHM and intensity of both modes increase.

At point 2 the Raman spectra has 6 components, four of which belong to WS$_2$. The excitation energy (2.33 eV) is in resonance with the WS$_2$ modes and that is why second-order mode at ∼ 320 cm^{-1} is also visible and it is attributed to the longitudinal acoustic mode at M point [172, 185]. The broad mode at ∼350 cm^{-1} is a combination of two modes: 2LA(M) and E$_{2g}^1(\Gamma)$, and the mode with ∼417 cm^{-1} frequency belongs to A$_{1g}$ phonon at Γ point. The frequency difference between WS$_2$ A$_{1g}(\Gamma)$ and WS$_2$ E$_{1g}(\Gamma)$ at point 2 is equal to ∼62 cm^{-1}, which corresponds to a monolayer WS$_2$ [185]. The difference of MoS$_2$ modes at point 2 is ∼18 cm^{-1}, indicating that MoS$_2$ at point 2 is also a monolayer. This means that at the point 2 (the inner part of the multilayer edge) is made from a vertical heterostructure, which contains one layer of MoS$_2$ and one of WS$_2$.

At point 4 the frequency difference of WS$_2$ A$_{1g}(\Gamma)$ and WS$_2$ E$_{1g}(\Gamma)$ modes is also ∼62 cm^{-1}, confirming that the most outer edge is made from monolayer WS$_2$.

In order to determine the origin of the PL emission lines, I have made power-dependent measurements on the same points. The PL spectra with corresponding fit components are shown in Figure 5.6 a). The normalized PL spectra were fitted using Lorentzian functions and the results are shown in Table 5.2.

At point 1 (green line in 5.6 a), on the bilayer MoS$_2$, the PL spectra has four components: B exciton (1.1), A exciton (1.2), trion (1.3) and an ILE (1.4). The PL intensities of both excitons increase linearly with the increase in excitation power, while the PL
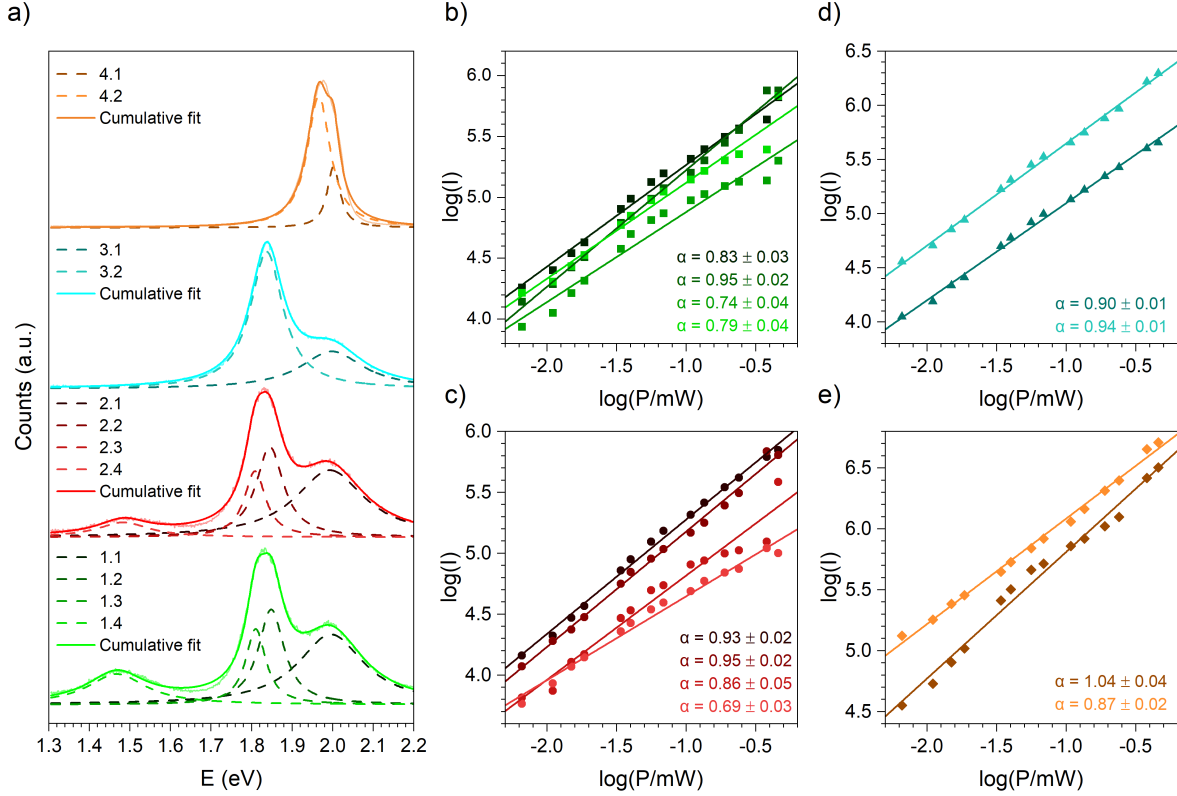
Figure 5.6: a) PL spectra taken at 4 points, indicated in Figure 5.4 d). Corresponding fit components are shown as dashed lines. b)-e) PL intensity dependence on laser power with corresponding coefficient for each fitting component.

intensities of the trion and ILE show slight sub-linearity. The sublinear behaviour for ILE is typical due to its long lifetime [186, 187].

As discussed in [187], effective charge transfer, which happens in first few-hundreds fs after the excitation, saturates optically active states - including those of an ILE. The reason why only the ILE shows sublinear dependence on the power is due to its long lifetime ($\sim$ns at 6 K) in comparison to the intralayer excitons ($\sim$ps). This means, that the levels corresponding to the intralayer excitons empty faster and have linear dependence on the excitation power, while the ILE saturates even at low excitation powers.

In point 2 (red line in 5.6 a), on the v-HS, the PL spectra has also 4 components: A exciton in WS_2 (2.1), A exciton in MoS_2 (2.2), trion (2.3) and ILE (2.4) [182]. This ILE is formed due to a type-II heterostructure, where the valence band maximum belongs to MoS_2 and conduction band minimum is located in WS_2 [188]. This type of band alignment leads to a reduced bandgap, which is lower than the intralayer direct transitions. Again, the PL intensities of both excitons and the trion have linear dependence on the excitation power, while the intensity of ILE saturates, in agreement with previous analysis.

At points 3 and 4 the PL lines belong to the emissions of monolayer MoS_2 and WS_2, respectively, and have two components. In all cases, the PL intensities have linear dependence on the excitation power.

59

Table 5.2: Fitting parameters for PL spectra in TMD heterostructure.

Location	Energy (eV)	FWHM (meV)	Intensity (a.u.)
Point 1	1.996 ± 0.001	199 ± 5	0.150 ± 0.005
	1.849 ± 0.002	77 ± 3	0.079 ± 0.008
	1.810 ± 0.001	61 ± 3	0.049 ± 0.006
	1.468 ± 0.001	176 ± 6	0.058 ± 0.003
Point 2	1.993 ± 0.001	208 ± 4	0.150 ± 0.004
	1.845 ± 0.002	82 ± 3	0.080 ± 0.009
	1.809 ± 0.001	64 ± 3	0.045 ± 0.007
	1.484 ± 0.002	153 ± 9	0.024 ± 0.002
Point 3	1.9982 ± 0.0007	190 ± 3	0.077 ± 0.001
	1.8374 ± 0.0001	98.2 ± 0.4	0.1449 ± 0.0006
Point 4	2.0024 ± 0.0005	38 ± 2	0.025 ± 0.002
	1.9659 ± 0.0006	69.0 ± 0.9	0.098 ± 0.002

5.3 Conclusion

In this Chapter, I investigated optical properties of a CVD-grown monolayer $Mo_{1-x}W_xS_2$ alloy and complex WS_2/MoS_2 heterostructure. Even though the growth procedures for these two materials are similar, the subtle differences in the growth temperature have strong impact on the outcome of synthesis processes. Further investigation of the synthesis phase space is needed to fully exploit the tunability of 1L MoS_2 bandgap via alloying. Higher growth temperature allowed for the diffusion of molybdenum atoms in the WS_2 lattice, while the second stage growth at lower temperature resulted in the growth of a complex WS_2/MoS_2 heterostructure. In this case, WS_2 is located in the defect-rich areas, such as edges of the previously grown MoS_2 island. Since the MoS_2 island has monolayer interior and a bilayer edge, the WS_2 has grown both on the inner and the outer part of the bilayer MoS_2 edge (Figure 5.4 d). The final product is an uncommon hybrid heterostructure: 1L WS_2 - 2L homobilayer MoS_2 - 2L heterobilayer MoS_2/WS_2 - 1L MoS_2, which was proven with point Raman spectra at four different locations on the island. Optical measurements on the nanoscale are planned in order to investigate interfaces in this heterostructure.

Chapter 6

Conclusion and outlook

The purpose of the research presented in this Thesis was investigating the influence of intrinsic defects on the optical properties of CVD-grown MoS_2 monocrystals. Understanding how intrinsic defects influence these properties on a microscopical level allows for development of more complex materials, such as alloys and heterostructures. Even though defects cannot be completely removed from a material, their concentration can be reduced by the optimisation of the synthesis parameters. The first step was establishing the reproducible recipe for CVD synthesis of high-quality MoS_2 monocrystals, with large lateral size, as presented in the Chapter 3. Samples synthesised at the optimum growth conditions have shown excellent optical response, which is homogeneous throughout the individual island, but also across the entire substrate as well. These samples also show no degradation after prolonged exposure to the atmospheric conditions, confirming again their excellent intrinsic quality. It was shown in Chapter 4 that the most important synthesis parameter for controlling the defect concentration is the growth temperature. Sample synthesised at the higher growth temperature has position independent optical and electronic properties, indicating lower defect concentration. After detailed analysis of monolayer MoS_2 samples, research was oriented towards the tuning of MoS_2 properties via alloying or heterostructure synthesis. In Chapter 5 monolayer $Mo_{1-x}W_xS_2$ alloy and a complex WS_2-MoS_2 heterostructure were analysed using photoluminescence and Raman microscopy.

Research presented in this Thesis provides a foundation for several new investigation pathways:

- the synthesis processes can easily be expanded to selenides and related alloys and heterostructures, tuning the bandgap towards the infrared spectrum. Also, different growth substrates can be used, such as sapphire, providing materials suitable for optical measurements in transmission.

- doping high-quality TMDs with metal atoms such as Cr, Fe or Co introduces novel properties in the host materials. Such materials are good candidates for fabrication

of magneto-optical and spintronic devices.

- defect-engineering of 1L TMDs towards the telecommunication wavelengths using rare-earth elements, such as Er and Yb.

- production of TMDs-plasmonic hybrid systems by decorating TMDs with metallic nanoparticles or nanorods as a building block for plasmonic devices.

References

[1] K. S. Novoselov, A. K. Geim, S. V. Morozov, D. Jiang, Y. Zhang, S. V. Dubonos, I. V. Grigorieva, and A. A. Firsov, "Electric field effect in atomically thin carbon films", Science **306**, 666–669 (2004).

[2] Y. Zhang, T.-T. Tang, C. Girit, Z. Hao, M. C. Martin, A. Zettl, M. F. Crommie, Y. R. Shen, and F. Wang, "Direct observation of a widely tunable bandgap in bilayer graphene", Nature **459**, 820–823 (2009).

[3] F. Xia, D. B. Farmer, Y. ming Lin, and P. Avouris, "Graphene field-effect transistors with high on/off current ratio and large transport band gap at room temperature", Nano Letters **10**, 715–718 (2010).

[4] S. Sahu and G. C. Rout, "Band gap opening in graphene: a short theoretical study", International Nano Letters **7**, 81–89 (2017).

[5] K. S. Novoselov, D. Jiang, F. Schedin, T. J. Booth, V. V. Khotkevich, S. V. Morozov, and A. K. Geim, "Two-dimensional atomic crystals", Proceedings of the National Academy of Sciences **102**, 10451–10453 (2005).

[6] B. Radisavljevic, A. Radenovic, J. Brivio, V. Giacometti, and A. Kis, "Single-layer MoS$_2$ transistors", Nature Nanotechnology **6**, 147–150 (2011).

[7] A. Castellanos-Gomez, "Why all the fuss about 2D semiconductors", Nature Photonics **10**, 202–204 (2016).

[8] N. Mounet, M. Gibertini, P. Schwaller, D. Campi, A. Merkys, A. Marrazzo, T. Sohier, I. E. Castelli, A. Cepellotti, G. Pizzi, and N. Marzari, "Two-dimensional materials from high-throughput computational exfoliation of experimentally known compounds", Nature Nanotechnology **13**, 246–252 (2018).

[9] M. Bosi, "Growth and synthesis of mono and few-layers transition metal dichalcogenides by vapour techniques: a review", RSC Advances **5**, 75500–75518 (2015).

[10] A. Rodin, *Two-dimensional semiconductor transition metal dichalcogenides: basic properties* (Elsevier, 2020), pages 1–23.

[11] J. Chen and J. H. Warner, *Atomic structure of defects in transitional metal dichalcogenides using transmission electron microscopy* (Elsevier, 2020), pages 167–197.

[12] V. Carozo, Y. Wang, K. Fujisawa, B. R. Carvalho, A. McCreary, S. Feng, Z. Lin, C. Zhou, N. Perea-López, A. L. Elías, B. Kabius, V. H. Crespi, and M. Terrones, "Optical identification of sulfur vacancies: bound excitons at the edges of monolayer tungsten disulfide", Science Advances **3** (2017).

[13] J. Hong, Z. Hu, M. Probert, K. Li, D. Lv, X. Yang, L. Gu, N. Mao, Q. Feng, L. Xie, J. Zhang, D. Wu, Z. Zhang, C. Jin, W. Ji, X. Zhang, J. Yuan, and Z. Zhang, "Exploring atomic defects in molybdenum disulphide monolayers", Nature Communications **6**, 6293 (2015).

[14] M. R. Rosenberger, H.-J. Chuang, K. M. McCreary, C. H. Li, and B. T. Jonker, "Electrical characterization of discrete defects and impact of defect density on photoluminescence in monolayer WS_2", ACS Nano **12**, 1793–1800 (2018).

[15] Y. Zhao, M. Tripathi, K. Čerņevičs, A. Avsar, H. G. Ji, J. F. G. Marin, C.-Y. Cheon, Z. Wang, O. V. Yazyev, and A. Kis, "Electrical spectroscopy of defect states and their hybridization in monolayer MoS_2", Nature Communications **14**, 44 (2023).

[16] H. Nan, R. Zhou, X. Gu, S. Xiao, and K. (Ken) Ostrikov, "Recent advances in plasma modification of 2D transition metal dichalcogenides", Nanoscale **11**, 19202–19213 (2019).

[17] P. K. Chow, R. B. Jacobs-Gedrim, J. Gao, T.-M. Lu, B. Yu, H. Terrones, and N. Koratkar, "Defect-induced photoluminescence in monolayer semiconducting transition metal dichalcogenides", ACS Nano **9**, 1520–1527 (2015).

[18] M. Ghorbani-Asl, S. Kretschmer, and A. V. Krasheninnikov, *Two-dimensional materials under ion irradiation: from defect production to structure and property engineering* (Elsevier, 2022), pages 259–301.

[19] T. He, Z. Wang, F. Zhong, H. Fang, P. Wang, and W. Hu, "Etching techniques in 2D materials", Advanced Materials Technologies **4** (2019).

[20] M. A. Aslam, T. H. Tran, A. Supina, O. Siri, V. Meunier, K. Watanabe, T. Taniguchi, M. Kralj, C. Teichert, E. Sheremet, R. D. Rodriguez, and A. Matković, "Single-crystalline nanoribbon network field effect transistors from arbitrary two-dimensional materials", npj 2D Materials and Applications **6** (2022).

[21] J. Azadmanjiri, P. Kumar, V. K. Srivastava, and Z. Sofer, "Surface functionalization of 2D transition metal oxides and dichalcogenides via covalent and non-covalent bonding for sustainable energy and biomedical applications", ACS Applied Nano Materials **3**, 3116–3143 (2020).

[22] R. Ibragimova, P. Erhart, P. Rinke, and H.-P. Komsa, "Surface functionalization of 2D MXenes: trends in distribution, composition, and electronic properties", The Journal of Physical Chemistry Letters **12**, 2377–2384 (2021).

[23] S. Manzeli, D. Ovchinnikov, D. Pasquier, O. V. Yazyev, and A. Kis, "2D transition metal dichalcogenides", Nature Reviews Materials **2**, 17033 (2017).

[24] Z. M. Wang, *MoS2* (Springer Cham, 2014).

[25] K. F. Mak, C. Lee, J. Hone, J. Shan, and T. F. Heinz, "Atomically thin MoS_2 : a new direct-gap semiconductor", Physical Review Letters **105**, 136805 (2010).

[26] A. Kuc, *Low-dimensional transition-metal dichalcogenides* (The Royal Society of Chemistry, Nov. 2014).

[27] R. W. Boyd, *Nonlinear optics* (Academic Press, 2008).

[28] Y. Li, Y. Rao, K. F. Mak, Y. You, S. Wang, C. R. Dean, and T. F. Heinz, "Probing symmetry properties of few-layer MoS_2 and h-BN by optical second-harmonic generation", Nano Letters **13**, 3329–3333 (2013).

[29] J. L. Verble and T. J. Wieting, "Lattice mode degeneracy in MoS_2 and other layer compounds", Physical Review Letters **25**, 362–365 (1970).

[30] P.-H. Tan, editor, *Raman spectroscopy of two-dimensional materials*, Vol. 276 (Springer Singapore, 2019).

[31] X. Zhang, X.-F. Qiao, W. Shi, J.-B. Wu, D.-S. Jiang, and P.-H. Tan, "Phonon and Raman scattering of two-dimensional transition metal dichalcogenides from monolayer, multilayer to bulk material", Chemical Society Reviews **44**, 2757–2785 (2015).

[32] X. Zhang, W. P. Han, J. B. Wu, S. M. amd Y. Lu, Q. Q. Li, A. C. Ferrari, and P. H. Tan, "Raman spectroscopy of shear and layer breathing modes in multilayer MoS_2", Physical Review B **87** (2013).

[33] M. O'Brien, N. McEvoy, D. Hanlon, T. Hallam, J. N. Coleman, and G. S. Duesberg, "Mapping of low-frequency raman modes in CVD-grown transition metal dichalcogenides: layer number, stacking orientation and resonant effects", Scientific Reports **6** (2016).

[34] A. Splendiani, L. Sun, Y. Zhang, T. Li, J. Kim, C.-Y. Chim, G. Galli, and F. Wang, "Emerging photoluminescence in monolayer MoS_2", Nano Letters **10**, 1271–1275 (2010).

[35] O. Skrypka, "Optical properties of transition metal dichalcogenide monolayers, heterostructures and alloys", PhD Thesis (University of Sheffield, UK, 2018).

[36] D. Xiao, G.-B. Liu, W. Feng, X. Xu, and W. Yao, "Coupled spin and valley physics in monolayers of MoS_2 and other group-VI dichalcogenides", Physical Review Letters **108**, 196802 (2012).

[37] T. Cao, G. Wang, W. Han, H. Ye, C. Zhu, J. Shi, Q. Niu, P. Tan, E. Wang, B. Liu, and J. Feng, "Valley-selective circular dichroism of monolayer molybdenum disulphide", Nature Communications **3**, 887 (2012).

[38] X. Xu, W. Yao, D. Xiao, and T. F. Heinz, "Spin and pseudospins in layered transition metal dichalcogenides", Nature Physics **10**, 343–350 (2014).

[39] K. F. Mak, K. He, J. Shan, and T. F. Heinz, "Control of valley polarization in monolayer MoS_2 by optical helicity", Nature Nanotechnology **7**, 494–498 (2012).

[40] E. J. Sie, *Coherent light-matter interactions in monolayer transition-metal dichalcogenides* (Springer International Publishing, 2018).

[41] T. Cheiwchanchamnangij and W. R. L. Lambrecht, "Quasiparticle band structure calculation of monolayer, bilayer, and bulk MoS_2", Physical Review B **85**, 205302 (2012).

[42] A. Ramasubramaniam, "Large excitonic effects in monolayers of molybdenum and tungsten dichalcogenides", Physical Review B **86**, 115409 (2012).

[43] H.-P. Komsa and A. V. Krasheninnikov, "Effects of confinement and environment on the electronic structure and exciton binding energy of MoS_2 from first principles", Physical Review B **86**, 241201 (2012).

[44] K. He, N. Kumar, L. Zhao, Z. Wang, K. F. Mak, H. Zhao, and J. Shan, "Tightly bound excitons in monolayer WSe_2", Physical Review Letters **113**, 026803 (2014).

[45] A. Chernikov, T. C. Berkelbach, H. M. Hill, A. Rigosi, Y. Li, B. Aslan, D. R. Reichman, M. S. Hybertsen, and T. F. Heinz, "Exciton binding energy and non-hydrogenic Rydberg series in monolayer WS_2", Physical Review Letters **113**, 076802 (2014).

[46] C. Palacios-Berraquero, *Quantum confined excitons in 2-dimensional materials* (Springer International Publishing, 2018).

[47] G. Wang, A. Chernikov, M. M. Glazov, T. F. Heinz, X. Marie, T. Amand, and B. Urbaszek, "Colloquium: excitons in atomically thin transition metal dichalcogenides", Reviews of Modern Physics **90**, 021001 (2018).

[48] A. Rodin, M. Trushin, A. Carvalho, and A. H. C. Neto, "Collective excitations in 2D materials", Nature Reviews Physics **2**, 524–537 (2020).

[49] B. Chakraborty, A. Bera, D. V. S. Muthu, S. Bhowmick, U. V. Waghmare, and A. K. Sood, "Symmetry-dependent phonon renormalization in monolayer MoS_2 transistor", Physical Review B **85**, 161403 (2012).

[50] T. Korn, S. Heydrich, M. Hirmer, J. Schmutzler, and C. Schüller, "Low-temperature photocarrier dynamics in monolayer MoS_2", Applied Physics Letters **99** (2011).

[51] G. Plechinger, F.-X. Schrettenbrunner, J. Eroms, D. Weiss, C. Schüller, and T. Korn, "Low-temperature photoluminescence of oxide-covered single-layer MoS_2", Physica Status Solidi **6**, 126–128 (2012).

[52] Y. Cao, V. Fatemi, S. Fang, K. Watanabe, T. Taniguchi, E. Kaxiras, and P. Jarillo-Herrero, "Unconventional superconductivity in magic-angle graphene superlattices", Nature **556**, 43–50 (2018).

[53] Y. Chen, J. Xi, D. O. Dumcenco, Z. Liu, K. Suenaga, D. Wang, Z. Shuai, Y.-S. Huang, and L. Xie, "Tunable band gap photoluminescence from atomically thin transition-metal dichalcogenide alloys", ACS Nano **7**, 4610–4616 (2013).

[54] P. Tang, H. Shu, M. Yang, M. Zhang, C. Sheng, P. Liang, D. Cao, and X. Chen, "Rapid wafer-scale growth of $MoS_{2(1-x)}Se_{2x}$ alloy monolayers with tunable compositions and optical properties for high-performance photodetectors", ACS Applied Nano Materials **4**, 12609–12618 (2021).

[55] S. Fu, K. Kang, K. Shayan, A. Yoshimura, S. Dadras, X. Wang, L. Zhang, S. Chen, N. Liu, A. Jindal, X. Li, A. N. Pasupathy, A. N. Vamivakas, V. Meunier, S. Strauf, and E.-H. Yang, "Enabling room temperature ferromagnetism in monolayer MoS_2 via in situ iron-doping", Nature Communications **11**, 2034 (2020).

[56] J. Zhou, J. Lin, H. Sims, C. Jiang, C. Cong, J. A. Brehm, Z. Zhang, L. Niu, Y. Chen, Y. Zhou, Y. Wang, F. Liu, C. Zhu, T. Yu, K. Suenaga, R. Mishra, S. T. Pantelides, Z. Zhu, W. Gao, Z. Liu, and W. Zhou, "Synthesis of Co-doped MoS_2 monolayers with enhanced valley splitting", Advanced Materials **32** (2020).

[57] Y. Li, X. Cheng, Y. Zhao, M. Liu, F. Li, C. Huang, L. Dai, Y. Wan, and E. Kan, "Room-temperature ferromagnetism in layered Mn-substituted MoS_2", The Journal of Physical Chemistry C **127**, 12648–12654 (2023).

[58] A. K. Geim and I. V. Grigorieva, "Van der Waals heterostructures", Nature **499**, 419–425 (2013).

[59] L. Britnell, R. M. Ribeiro, A. Eckmann, R. Jalil, B. D. Belle, A. Mishchenko, Y.-J. Kim, R. V. Gorbachev, T. Georgiou, S. V. Morozov, A. N. Grigorenko, A. K. Geim, C. Casiraghi, A. H. C. Neto, and K. S. Novoselov, "Strong light-matter interactions in heterostructures of atomically thin films", Science **340**, 1311–1314 (2013).

[60] F. Withers, O. D. Pozo-Zamudio, A. Mishchenko, A. P. Rooney, A. Gholinia, K. Watanabe, T. Taniguchi, S. J. Haigh, A. K. Geim, A. I. Tartakovskii, and K. S. Novoselov, "Light-emitting diodes by band-structure engineering in van der Waals heterostructures", Nature Materials **14**, 301–306 (2015).

[61] M. Bernardi, M. Palummo, and J. C. Grossman, "Extraordinary sunlight absorption and one nanometer thick photovoltaics using two-dimensional monolayer materials", Nano Letters **13**, 3664–3670 (2013).

[62] M. Bernardi, C. Ataca, M. Palummo, and J. C. Grossman, "Optical and electronic properties of two-dimensional layered materials", Nanophotonics **6**, 479–493 (2017).

[63] Y. Jiang, S. Chen, W. Zheng, B. Zheng, and A. Pan, "Interlayer exciton formation, relaxation, and transport in TMD van der Waals heterostructures", Light: Science & Applications **10** (2021).

[64] J. Wang, Z. Li, H. Chen, G. Deng, and X. Niu, "Recent advances in 2D lateral heterostructures", Nano-Micro Letters **11**, 48 (2019).

[65] Y. Kobayashi, S. Mori, Y. Maniwa, and Y. Miyata, "Bandgap-tunable lateral and vertical heterostructures based on monolayer $Mo_{1-x}W_xS_2$ alloys", Nano Research **8**, 3261–3271 (2015).

[66] X. Fang, Q. Tian, Y. Sheng, G. Yang, N. Lu, J. Wang, X. Zhang, Y. Zhang, X. Yan, and B. Hua, "Chemical vapor deposition of $WS_2/Mo_{1-x}W_xS_2/MoS_2$ lateral heterostructures", Superlattices and Microstructures **123**, 323–329 (2018).

[67] J. D. Cain, E. D. Hanson, and V. P. Dravid, "Controlled synthesis of 2D MX_2 (M = Mo, W; X = S, Se) heterostructures and alloys", Journal of Applied Physics **123** (2018).

[68] K. Barthelmi, J. Klein, A. Hötger, L. Sigl, F. Sigger, E. Mitterreiter, S. Rey, S. Gyger, M. Lorke, M. Florian, F. Jahnke, T. Taniguchi, K. Watanabe, V. Zwiller, K. D. Jöns, U. Wurstbauer, C. Kastl, A. Weber-Bargioni, J. J. Finley, K. Müller, and A. W. Holleitner, "Atomistic defects as single-photon emitters in atomically thin MoS_2", Applied Physics Letters **117** (2020).

[69] S. Vadia, J. Scherzer, H. Thierschmann, C. Schäfermeier, C. Dal Savio, T. Taniguchi, K. Watanabe, D. Hunger, K. Karraï, and A. Högele, "Open-cavity in closed-cycle cryostat as a quantum optics platform", PRX Quantum **2**, 040318 (2021).

[70] M. Förg, L. Colombier, R. K. Patel, J. Lindlau, A. D. Mohite, H. Yamaguchi, M. M. Glazov, D. Hunger, and A. Högele, "Cavity-control of interlayer excitons in van der Waals heterostructures", Nature Communications **10**, 3697 (2019).

[71] G. E. Moore, "Cramming more components onto integrated circuits", Electronics **38**, 114 (1965).

[72] D. Akinwande, C. Huyghebaert, C.-H. Wang, M. I. Serna, S. Goossens, L.-J. Li, H.-S. P. Wong, and F. H. L. Koppens, "Graphene and two-dimensional materials for silicon technology", Nature **573**, 507–518 (2019).

[73] Y.-H. Wang, K.-J. Huang, and X. Wu, "Recent advances in transition-metal dichalcogenides based electrochemical biosensors: a review", Biosensors and Bioelectronics **97**, 305–316 (2017).

[74] R. Ge, X. Wu, M. Kim, J. Shi, S. Sonde, L. Tao, Y. Zhang, J. C. Lee, and D. Akinwande, "Atomristor: nonvolatile resistance switching in atomic sheets of transition metal dichalcogenides", Nano Letters **18**, 434–441 (2018).

[75] M. Romagnoli, V. Sorianello, M. Midrio, F. H. L. Koppens, C. Huyghebaert, D. Neumaier, P. Galli, W. Templ, A. D'Errico, and A. C. Ferrari, "Graphene-based integrated photonics for next-generation datacom and telecom", Nature Reviews Materials **3**, 392–414 (2018).

[76] C. González, J. Silva, A. Viana, K. Gwozdz, and O. Conde, "Shape-controlled monolayer MoSe$_2$ flakes by chemical vapor deposition towards tuning the photoluminescence emission", Applied Surface Science **605**, 154742 (2022).

[77] L. Fang, H. Chen, X. Yuan, H. Huang, G. Chen, L. Li, J. Ding, J. He, and S. Tao, "Quick optical identification of the defect formation in monolayer WSe$_2$ for growth optimization", Nanoscale Research Letters **14**, 274 (2019).

[78] S. K. Kang and H. S. Lee, "Study on growth parameters for monolayer MoS$_2$ synthesized by CVD using solution-based metal precursors", Applied Science and Convergence Technology **28**, 159–163 (2019).

[79] J. You, M. D. Hossain, and Z. Luo, "Synthesis of 2D transition metal dichalcogenides by chemical vapor deposition with controlled layer number and morphology", Nano Convergence **5**, 26 (2018).

[80] J. Chen, W. Tang, B. Tian, B. Liu, X. Zhao, Y. Liu, T. Ren, W. Liu, D. Geng, H. Y. Jeong, H. S. Shin, W. Zhou, and K. P. Loh, "Chemical vapor deposition of high-quality large-sized MoS$_2$ crystals on silicon dioxide substrates", Advanced Science **3** (2016).

[81] D. Kong, H. Wang, J. J. Cha, M. Pasta, K. J. Koski, J. Yao, and Y. Cui, "Synthesis of MoS$_2$ and MoSe$_2$ films with vertically aligned layers", Nano Letters **13**, 1341–1347 (2013).

[82] Y.-C. Lin, W. Zhang, J.-K. Huang, K.-K. Liu, Y.-H. Lee, C.-T. Liang, C.-W. Chu, and L.-J. Li, "Wafer-scale MoS$_2$ thin layers prepared by MoO$_3$ sulfurization", Nanoscale **4**, 6637 (2012).

[83] Y.-H. Lee, X.-Q. Zhang, W. Zhang, M.-T. Chang, C.-T. Lin, K.-D. Chang, Y.-C. Yu, J. T.-W. Wang, C.-S. Chang, L.-J. Li, and T.-W. Lin, "Synthesis of large-area MoS$_2$ atomic layers with chemical vapor deposition", Advanced Materials **24**, 2320–2325 (2012).

[84] X. Ling, Y.-H. Lee, Y. Lin, W. Fang, L. Yu, M. S. Dresselhaus, and J. Kong, "Role of the seeding promoter in MoS$_2$ growth by chemical vapor deposition", Nano Letters **14**, 464–472 (2014).

[85] P. Yang, X. Zou, Z. Zhang, M. Hong, J. Shi, S. Chen, J. Shu, L. Zhao, S. Jiang, X. Zhou, Y. Huan, C. Xie, P. Gao, Q. Chen, Q. Zhang, Z. Liu, and Y. Zhang, "Batch production of 6-inch uniform monolayer molybdenum disulfide catalyzed by sodium in glass", Nature Communications **9**, 979 (2018).

[86] S. H. Choi, Y. J. Kim, W. Yang, and K. K. Kim, "Alkali metal-assisted growth of single-layer molybdenum disulfide", Journal of the Korean Physical Society **74**, 1032–1038 (2019).

[87] A. Singh, M. Moun, and R. Singh, "Effect of different precursors on CVD growth of molybdenum disulfide", Journal of Alloys and Compounds **782**, 772–779 (2019).

[88] S. Chowdhury, A. Roy, C. Liu, M. H. Alam, R. Ghosh, H. Chou, D. Akinwande, and S. K. Banerjee, "Two-step growth of uniform monolayer MoS_2 nanosheets by metal–organic chemical vapor deposition", ACS Omega **6**, 10343–10351 (2021).

[89] S. Ishihara, Y. Hibino, N. Sawamoto, H. Machida, H. Wakabayashi, and A. Ogura, "MOCVD of monolayer MoS_2 using novel molybdenum precursor i-$Pr_2DADMo(CO)_3$", MRS Advances **3**, 379–384 (2018).

[90] S. Wang, Y. Rong, Y. Fan, M. Pacios, H. Bhaskaran, K. He, and J. H. Warner, "Shape evolution of monolayer MoS_2 crystals grown by chemical vapor deposition", Chemistry of Materials **26**, 6371–6379 (2014).

[91] Y. Gong, S. Lei, G. Ye, B. Li, Y. He, K. Keyshar, X. Zhang, Q. Wang, J. Lou, Z. Liu, R. Vajtai, W. Zhou, and P. M. Ajayan, "Two-step growth of two-dimensional $WSe_2/MoSe_2$ heterostructures", Nano Letters **15**, 6135–6141 (2015).

[92] M. Alahmadi, F. Mahvash, T. Szkopek, and M. Siaj, "A two-step chemical vapor deposition process for the growth of continuous vertical heterostructure WSe_2/h-BN and its optical properties", RSC Advances **11**, 16962–16969 (2021).

[93] X. Gong, X. Zhao, M. E. Pam, H. Yao, Z. Li, D. Geng, S. J. Pennycook, Y. Shi, and H. Y. Yang, "Location-selective growth of two-dimensional metallic/semiconducting transition metal dichalcogenide heterostructures", Nanoscale **11**, 4183–4189 (2019).

[94] J. Bajo, "Optical characterization of transition metal dichalcogenides for synthesis parameters improvements", Master Thesis (University of Zagreb, Croatia, 2020).

[95] S. Y. Yang, G. W. Shim, S.-B. Seo, and S.-Y. Choi, "Effective shape-controlled growth of monolayer MoS_2 flakes by powder-based chemical vapor deposition", Nano Research **10**, 255–262 (2017).

[96] M. Suleman, S. Lee, M. Kim, V. H. Nguyen, M. Riaz, N. Nasir, S. Kumar, H. M. Park, J. Jung, and Y. Seo, "NaCl-assisted temperature-dependent controllable growth of large-area MoS_2 crystals using confined-space CVD", ACS Omega **7**, 30074–30086 (2022).

[97]   *National informal STEM education network,* Last accessed 9 September 2023, `https://www.nisenet.org/catalog/scientific-image-atomic-force-microscope-illustration`.

[98]   W. Melitz, J. Shen, A. C. Kummel, and S. Lee, "Kelvin probe force microscopy and its application", Surface Science Reports **66**, 1–27 (2011).

[99]   M. M. Beerbom, B. Lägel, A. J. Cascio, B. V. Doran, and R. Schlaf, "Direct comparison of photoemission spectroscopy and in situ Kelvin probe work function measurements on indium tin oxide films", Journal of Electron Spectroscopy and Related Phenomena **152** (2006).

[100] B. J. Inkson, *Scanning electron microscopy (SEM) and transmission electron microscopy (TEM) for materials characterization* (Woodhead Publishing, 2016).

[101] *Monospektra,* Last accessed 9 September 2023, `https://www.monospektra.com/applications/drives-positioning-systems-electron-microscopes`.

[102] T. Mueller and E. Malic, "Exciton physics and device application of two-dimensional transition metal dichalcogenide semiconductors", npj 2D Materials and Applications **2**, 29 (2018).

[103] T. Virgili, G. Grancini, E. Molotokaite, I. Suarez-Lopez, S. K. Rajendran, A. Liscio, V. Palermo, G. Lanzani, D. Polli, and G. Cerullo, "Confocal ultrafast pump–probe spectroscopy: a new technique to explore nanoscale composites", Nanoscale **4**, 2219 (2012).

[104] I. S. Kim, V. K. Sangwan, D. Jariwala, J. D. Wood, S. Park, K.-S. Chen, F. Shi, F. Ruiz-Zepeda, A. Ponce, M. Jose-Yacaman, V. P. Dravid, T. J. Marks, M. C. Hersam, and L. J. Lauhon, "Influence of stoichiometry on the optical and electrical properties of chemical vapor deposition derived MoS_2", ACS Nano **8**, 10551–10558 (2014).

[105] X. Zhang, H. Nan, S. Xiao, X. Wan, X. Gu, A. Du, Z. Ni, and K. Ostrikov, "Transition metal dichalcogenides bilayer single crystals by reverse-flow chemical vapor epitaxy", Nature Communications **10**, 598 (2019).

[106] H. Liu, Y. Zhu, Q. Meng, X. Lu, S. Kong, Z. Huang, P. Jiang, and X. Bao, "Role of the carrier gas flow rate in monolayer MoS_2 growth by modified chemical vapor deposition", Nano Research **10**, 643–651 (2017).

[107] A. M. van der Zande, P. Y. Huang, D. A. Chenet, T. C. Berkelbach, Y. You, G.-H. Lee, T. F. Heinz, D. R. Reichman, D. A. Muller, and J. C. Hone, "Grains and grain boundaries in highly crystalline monolayer molybdenum disulphide", Nature Materials **12**, 554–561 (2013).

[108] H. F. Liu, S. L. Wong, and D. Z. Chi, "CVD growth of MoS_2-based two-dimensional materials", Chemical Vapor Deposition **21**, 241–259 (2015).

[109] H. Kim, G. H. Han, S. J. Yun, J. Zhao, D. H. Keum, H. Y. Jeong, T. H. Ly, Y. Jin, J.-H. Park, B. H. Moon, S.-W. Kim, and Y. H. Lee, "Role of alkali metal promoter in enhancing lateral growth of monolayer transition metal dichalcogenides", Nanotechnology **28**, 36LT01 (2017).

[110] L. Yuan and L. Huang, "Exciton dynamics and annihilation in WS_2 2D semiconductors", Nanoscale **7**, 7402–7408 (2015).

[111] K. M. McCreary, A. T. Hanbicki, S. Singh, R. K. Kawakami, G. G. Jernigan, M. Ishigami, A. Ng, T. H. Brintlinger, R. M. Stroud, and B. T. Jonker, "The effect of preparation conditions on Raman and photoluminescence of monolayer WS_2", Scientific Reports **6**, 35154 (2016).

[112] M. Amani, D.-H. Lien, D. Kiriya, J. Xiao, A. Azcatl, J. Noh, S. R. Madhvapathy, R. Addou, S. KC, M. Dubey, K. Cho, R. M. Wallace, S.-C. Lee, J.-H. He, J. W. Ager, X. Zhang, E. Yablonovitch, and A. Javey, "Near-unity photoluminescence quantum yield in MoS_2", Science **350**, 1065–1068 (2015).

[113] K. M. McCreary, M. Currie, A. T. Hanbicki, H.-J. Chuang, and B. T. Jonker, "Understanding variations in circularly polarized photoluminescence in monolayer transition metal dichalcogenides", ACS Nano **11**, 7988–7994 (2017).

[114] K. M. McCreary, A. T. Hanbicki, S. V. Sivaram, and B. T. Jonker, "A- and b-exciton photoluminescence intensity ratio as a measure of sample quality for transition metal dichalcogenide monolayers", APL Materials **6** (2018).

[115] G Plechinger, J Mann, E Preciado, D Barroso, A Nguyen, J Eroms, C Schüller, L Bartels, and T Korn, "A direct comparison of CVD-grown and exfoliated MoS_2 using optical spectroscopy", Semiconductor Science and Technology **29**, 064008 (2014).

[116] M. S. Kim, S. J. Yun, Y. Lee, C. Seo, G. H. Han, K. K. Kim, Y. H. Lee, and J. Kim, "Biexciton emission from edges and grain boundaries of triangular WS_2 monolayers", ACS Nano **10**, 2399–2405 (2016).

[117] M. M. Perera, M.-W. Lin, H.-J. Chuang, B. P. Chamlagain, C. Wang, X. Tan, M. M.-C. Cheng, D. Tománek, and Z. Zhou, "Improved carrier mobility in few-layer MoS_2 field-effect transistors with ionic-liquid gating", ACS Nano **7**, 4449–4458 (2013).

[118] A. Azcatl, X. Qin, A. Prakash, C. Zhang, L. Cheng, Q. Wang, N. Lu, M. J. Kim, J. Kim, K. Cho, R. Addou, C. L. Hinkle, J. Appenzeller, and R. M. Wallace, "Covalent nitrogen doping and compressive strain in MoS_2 by remote N_2 plasma exposure", Nano Letters **16**, 5437–5443 (2016).

[119] W. H. Chae, J. D. Cain, E. D. Hanson, A. A. Murthy, and V. P. Dravid, "Substrate-induced strain and charge doping in CVD-grown monolayer MoS_2", Applied Physics Letters **111** (2017).

[120] S. Kataria, S. Wagner, T. Cusati, A. Fortunelli, G. Iannaccone, H. Pandey, G. Fiori, and M. C. Lemme, "Growth-induced strain in chemical vapor deposited monolayer MoS_2: experimental and theoretical investigation", Advanced Materials Interfaces **4** (2017).

[121] Z. Liu, M. Amani, S. Najmaei, Q. Xu, X. Zou, W. Zhou, T. Yu, C. Qiu, A. G. Birdwell, F. J. Crowne, R. Vajtai, B. I. Yakobson, Z. Xia, M. Dubey, P. M. Ajayan, and J. Lou, "Strain and structure heterogeneity in MoS_2 atomic layers grown by chemical vapour deposition", Nature Communications **5**, 5246 (2014).

[122] G. Plechinger, P. Nagler, J. Kraus, N. Paradiso, C. Strunk, C. Schüller, and T. Korn, "Identification of excitons, trions and biexcitons in single-layer WS_2", physica status solidi (RRL) - Rapid Research Letters **9**, 457–461 (2015).

[123] A. Hanbicki, G. Kioseoglou, M. Currie, C. S. Hellberg, K. McCreary, A. Friedman, and B. Jonker, "Anomalous temperature-dependent spin-valley polarization in monolayer WS_2", Scientific Reports **6**, 18885 (2016).

[124] M. Currie, A. T. Hanbicki, G. Kioseoglou, and B. T. Jonker, "Optical control of charged exciton states in tungsten disulfide", Applied Physics Letters **106** (2015).

[125] "Defects activated photoluminescence in two-dimensional semiconductors: interplay between bound, charged and free excitons", Scientific Reports **3**, 2657 (2013).

[126] Y. You, X.-X. Zhang, T. C. Berkelbach, M. S. Hybertsen, D. R. Reichman, and T. F. Heinz, "Observation of biexcitons in monolayer WSe_2", Nature Physics **11** (2015).

[127] L. Sortino, M. Gülmüs, B. Tilmann, L. de S. Menezes, and S. A. Maier, "Radiative suppression of exciton–exciton annihilation in a two-dimensional semiconductor", Light: Science & Applications **12** (2023).

[128] J. Kunstmann, T. B. Wendumu, and G. Seifert, "Localized defect states in MoS_2 monolayers: electronic and optical properties", physica status solidi (b) **254**, 1600645 (2017).

[129] C. Hu, C. Yuan, A. Hong, M. Guo, T. Yu, and X. Luo, "Work function variation of monolayer MoS_2 by nitrogen-doping", Applied Physics Letters **113** (2018).

[130] S. Y. Lee, U. J. Kim, J. Chung, H. Nam, H. Y. Jeong, G. H. Han, H. Kim, H. M. Oh, H. Lee, H. Kim, Y.-G. Roh, J. Kim, S. W. Hwang, Y. Park, and Y. H. Lee, "Large work function modulation of monolayer MoS_2 by ambient gases", ACS Nano **10**, 6100–6107 (2016).

[131] W. Zhou, X. Zou, S. Najmaei, Z. Liu, Y. Shi, J. Kong, J. Lou, P. M. Ajayan, B. I. Yakobson, and J.-C. Idrobo, "Intrinsic structural defects in monolayer molybdenum disulfide", Nano Letters **13**, 2615–2622 (2013).

[132] I. D. Marion, D. Čapeta, B. Pielić, F. Faraguna, A. Gallardo, P. Pou, B. Biel, N. Vujičić, and M. Kralj, "Atomic-scale defects and electronic properties of a transferred synthesized MoS_2 monolayer", Nanotechnology **29**, 305703 (2018).

[133] Z. Wu, Z. Luo, Y. Shen, W. Zhao, W. Wang, H. Nan, X. Guo, L. Sun, X. Wang, Y. You, and Z. Ni, "Defects as a factor limiting carrier mobility in WSe_2: a spectroscopic investigation", Nano Research **9**, 3622–3631 (2016).

[134] C. Kastl, R. J. Koch, C. T. Chen, J. Eichhorn, S. Ulstrup, A. Bostwick, C. Jozwiak, T. R. Kuykendall, N. J. Borys, F. M. Toma, S. Aloni, A. Weber-Bargioni, E. Rotenberg, and A. M. Schwartzberg, "Effects of defects on band structure and excitons in WS_2 revealed by nanoscale photoemission spectroscopy", ACS Nano, acsnano.8b06574 (2019).

[135] A. Senkić, J. Bajo, A. Supina, B. Radatović, and N. Vujičić, "Effects of CVD growth parameters on global and local optical properties of MoS_2 monolayers", Materials Chemistry and Physics **296**, 127185 (2023).

[136] J. D. Cain, F. Shi, J. Wu, and V. P. Dravid, "Growth mechanism of transition metal dichalcogenide monolayers: the role of self-seeding fullerene nuclei", ACS Nano **10**, 5440–5445 (2016).

[137] C. Cong, J. Shang, X. Wu, B. Cao, N. Peimyoo, C. Qiu, L. Sun, and T. Yu, "Synthesis and optical properties of large-area single-crystalline 2D semiconductor WS_2 monolayer from chemical vapor deposition", Advanced Optical Materials **2**, 131–136 (2014).

[138] Z. Wu, W. Zhao, J. Jiang, T. Zheng, Y. You, J. Lu, and Z. Ni, "Defect activated photoluminescence in WSe_2 monolayer", The Journal of Physical Chemistry C **121**, 12294–12299 (2017).

[139] N. Saigal and S. Ghosh, "Evidence for two distinct defect related luminescence features in monolayer MoS_2", Applied Physics Letters **109** (2016).

[140] Y. Zhang, Z. Wang, J. Xi, and J. Yang, "Temperature-dependent band gaps in several semiconductors: from the role of electron–phonon renormalization", Journal of Physics: Condensed Matter **32** (2020).

[141] T. Takagahara, "Localization and homogeneous dephasing relaxation of quasi-two-dimensional excitons in quantum-well heterostructures", Physical Review B **32**, 7013–7015 (1985).

[142] J. Lee, E. S. Koteles, and M. O. Vassell, "Luminescence linewidths of excitons in GaAs quantum wells below 150 k", Physical Review B **33**, 5512–5516 (1986).

[143] M. Selig, G. Berghäuser, A. Raja, P. Nagler, C. Schüller, T. F. Heinz, T. Korn, A. Chernikov, E. Malic, and A. Knorr, "Excitonic linewidth and coherence lifetime in monolayer transition metal dichalcogenides", Nature Communications **7**, 13279 (2016).

[144] L. C. Andreani, F. Tassone, and F. Bassani, "Radiative lifetime of free excitons in quantum wells", Solid State Communications **77**, 641–645 (1991).

[145] R. Kaupmees, M. Grossberg, M. Ney, A. Asaithambi, A. Lorke, and J. Krustok, "Tailoring of bound exciton photoluminescence emission in WS_2 monolayers", Physica status solidi (RRL) – Rapid Research Letters **14** (2020).

[146] D. Rudolph, L. Schweickert, S. Morkötter, L. Hanschke, S. Hertenberger, M. Bichler, G. Koblmüller, G. Abstreiter, and J. J. Finley, "Probing the trapping and thermal activation dynamics of excitons at single twin defects in GaAs–AlGaAs core–shell nanowires", New Journal of Physics **15**, 113032 (2013).

[147] Z. R. Kudrynskyi, X. Wang, J. Sutcliffe, M. A. Bhuiyan, Y. Fu, Z. Yang, O. Makarovsky, L. Eaves, A. Solomon, V. T. Maslyuk, Z. D. Kovalyuk, L. Zhang, and A. Patanè, "Van der Waals $SnSe_{2(1-x)}S_{2x}$ alloys: composition-dependent bowing coefficient and electron–phonon interaction", Advanced Functional Materials **30** (2020).

[148] K. P. O'Donnell and X. Chen, "Temperature dependence of semiconductor band gaps", Applied Physics Letters **58**, 2924–2926 (1991).

[149] D. H. Lee, S.-J. Choi, H. Kim, Y.-S. Kim, and S. Jung, "Direct probing of phonon mode specific electron–phonon scatterings in two-dimensional semiconductor transition metal dichalcogenides", Nature Communications **12**, 4520 (2021).

[150] R. Esteban-Puyuelo and B. Sanyal, "Role of defects in ultrafast charge recombination in monolayer MoS_2", Physical Review B **103**, 235433 (2021).

[151] L. Li and E. A. Carter, "Defect-mediated charge-carrier trapping and nonradiative recombination in WSe_2 monolayers", Journal of the American Chemical Society **141**, 10451–10461 (2019).

[152] L. Li, R. Long, T. Bertolini, and O. V. Prezhdo, "Sulfur adatom and vacancy accelerate charge recombination in MoS_2 but by different mechanisms: time-domain ab initio analysis", Nano Letters **17**, 7962–7967 (2017).

[153] D.-H. Lien, S. Z. Uddin, M. Yeh, M. Amani, H. Kim, J. W. Ager, E. Yablonovitch, and A. Javey, "Electrical suppression of all nonradiative recombination pathways in monolayer semiconductors", Science **364**, 468–471 (2019).

[154] L. Yuan, T. Wang, T. Zhu, M. Zhou, and L. Huang, "Exciton dynamics, transport, and annihilation in atomically thin two-dimensional semiconductors", The Journal of Physical Chemistry Letters **8**, 3371–3379 (2017).

[155] H. Shi, R. Yan, S. Bertolazzi, J. Brivio, B. Gao, A. Kis, D. Jena, H. G. Xing, and L. Huang, "Exciton dynamics in suspended monolayer and few-layer MoS_2 2D crystals", ACS Nano **7**, 1072–1080 (2013).

[156] Z. Chi, H. Chen, Z. Chen, Q. Zhao, H. Chen, and Y.-X. Weng, "Ultrafast energy dissipation via coupling with internal and external phonons in two-dimensional MoS_2", ACS Nano **12**, 8961–8969 (2018).

[157] Y. Rosenwaks, M. C. Hanna, D. H. Levi, D. M. Szmyd, R. K. Ahrenkiel, and A. J. Nozik, "Hot-carrier cooling in GaAs: quantum wells versus bulk", Physical Review B **48**, 14675–14678 (1993).

[158] R. Leheny, J. Shah, R. Fork, C. Shank, and A. Migus, "Dynamics of hot carrier cooling in photo-excited GaAs", Solid State Communications **31**, 809–813 (1979).

[159] S. D. Conte, C. Trovatello, C. Gadermaier, and G. Cerullo, "Ultrafast photophysics of 2D semiconductors and related heterostructures", Trends in Chemistry **2**, 28–42 (2020).

[160] P. D. Cunningham, K. M. McCreary, A. T. Hanbicki, M. Currie, B. T. Jonker, and L. M. Hayden, "Charge trapping and exciton dynamics in large-area CVD grown MoS_2", The Journal of Physical Chemistry C **120**, 5819–5826 (2016).

[161] A. Soni, D. Kushavah, L.-S. Lu, W.-H. Chang, and S. K. Pal, "Ultrafast exciton trapping and exciton–exciton annihilation in large-area CVD-grown monolayer WS_2", The Journal of Physical Chemistry C **125**, 23880–23888 (2021).

[162] F. Ceballos, Q. Cui, M. Z. Bellus, and H. Zhao, "Exciton formation in monolayer transition metal dichalcogenides", Nanoscale **8**, 11681–11688 (2016).

[163] S. Kar, Y. Su, R. R. Nair, and A. K. Sood, "Probing photoexcited carriers in a few-layer MoS_2 laminate by time-resolved optical pump–terahertz probe spectroscopy", ACS Nano **9**, 12004–12010 (2015).

[164] Z. E. Eroglu, D. Contreras, P. Bahrami, N. Azam, M. Mahjouri-Samani, and A. Boulesbaa, "Filling exciton trap-states in two-dimensional tungsten disulfide (WS_2) and diselenide (WSe_2) monolayers", Nanomaterials **11**, 770 (2021).

[165] K. Zhang, S. Feng, J. Wang, A. A. nad Ning Lu, R. Addou, N. Wang, C. Zhou, J. Lerach, V. Bojan, M. J. Kim, L.-Q. Chen, R. M. Wallace, M. Terrones, J. Zhu, and J. A. Robinson, "Manganese doping of monolayer MoS_2: the substrate is critical", Nano Letters **15** (2015).

[166] J. Wang, F. Sun, S. Yang, Y. Li, C. Zhao, M. Xu, Y. Zhang, and H. Zeng, "Robust ferromagnetism in Mn-doped MoS_2 nanostructures", Applied Physics Letters **109** (2016).

[167] Q. Li, X. Zhao, L. Deng, Z. Shi, S. Liu, Q. Wei, L. Zhang, Y. Cheng, L. Zhang, H. Lu, W. Gao, W. Huang, C.-W. Qiu, G. Xiang, S. J. Pennycook, Q. Xiong, K. P. Loh, and B. Peng, "Enhanced valley Zeeman splitting in Fe-doped monolayer MoS_2", ACS Nano **14** (2020).

[168] W. Hu, C. Wang, H. Tan, H. Duan, G. Li, N. Li, Q. Ji, Y. Lu, Y. Wang, Z. Sun, F. Hu, and W. Yan, "Embedding atomic cobalt into graphene lattices to activate room-temperature ferromagnetism", Nature Communications **12** (2021).

[169] K. Bogaert, S. Liu, J. Chesin, D. Titow, S. Gradečak, and S. Garaj, "Diffusion-mediated synthesis of MoS_2/WS_2 lateral heterostructures", Nano Letters **16**, 5129–5134 (2016).

[170] F. Chen, L. Wang, X. Ji, and Q. Zhang, "Temperature-dependent two-dimensional transition metal dichalcogenide heterostructures: controlled synthesis and their properties", ACS Applied Materials & Interfaces **9**, 30821–30831 (2017).

[171] J. JIANG, T. XU, J. LU, L. SUN, and Z. NI, "Defect engineering in 2D materials: precise manipulation and improved functionalities", Research **2019** (2019).

[172] Y. Chen, D. O. Dumcenco, Y. Zhu, X. Zhang, N. Mao, Q. Feng, M. Zhang, J. Zhang, P.-H. Tan, Y.-S. Huang, and L. Xie, "Composition-dependent Raman modes of $Mo_{1-x}W_xS_2$ monolayer alloys", Nanoscale **6**, 2833–2839 (2014).

[173] H. Yu, H. Yan, H. Li, Z. Li, Y. Bai, H. Zhu, and S. Yin, "Spatially graded millimeter sized $Mo_{1-x}W_xS_2$ monolayer alloys: synthesis and memory effect", ACS Applied Materials & Interfaces **13**, 44693–44702 (2021).

[174] A. Azizi, Y. Wang, G. Stone, A. L. Elias, Z. Lin, M. Terrones, V. H. Crespi, and N. Alem, "Defect coupling and sub-angstrom structural distortions in $W_{1-x}Mo_xS_2$ monolayers", Nano Letters **17**, 2802–2808 (2017).

[175] R. Yang, L. Liu, S. Feng, Y. Liu, S. Li, K. Zhai, J. Xiang, C. Mu, A. Nie, F. Wen, B. Wang, G. Zhang, Y. Gong, Z. Zhao, Y. Tian, and Z. Liu, "One-step growth of spatially graded $Mo_{1-x}W_xS_2$ monolayers with a wide span in composition (from x = 0 to 1) at a large scale", ACS Applied Materials & Interfaces **11**, 20979–20986 (2019).

[176] K. Ding, Q. Fu, H. Nan, X. Gu, K. Ostrikov, and S. Xiao, "Controllable synthesis of $WS_{2(1-x)}Se_{2x}$ monolayers with fast photoresponse by a facile chemical vapor deposition strategy", Materials Science and Engineering: B **269**, 115176 (2021).

[177] H. S. Kang, J. H. Kang, S. Lee, K. Lee, D. H. Koo, Y.-S. Kim, Y. J. Hong, Y.-J. Kim, K. Kim, D. Lee, and C.-H. Lee, "Bowing-alleviated continuous bandgap engineering of wafer-scale $WS_{2x}Se_{2(1-x)}$ monolayer alloys and their assembly into hetero-multilayers", NPG Asia Materials **14**, 90 (2022).

[178] H. Sun, X. Zhou, X. Wang, L. Xu, J. Zhang, K. Jiang, L. Shang, Z. Hu, and J. Chu, "P–n conversion of charge carrier types and high photoresponsive performance of composition modulated ternary alloy $WS_{2x}Se_{2(1-x)}$ field-effect transistors", Nanoscale **12**, 15304–15317 (2020).

[179] Q. Feng, N. Mao, J. Wu, H. Xu, C. Wang, J. Zhang, and L. Xie, "Growth of $MoS_{2(1-x)}Se_{2x}$ (x = 0.41–1.00) monolayer alloys with controlled morphology by physical vapor deposition", ACS Nano **9**, 7450–7455 (2015).

[180] X. Zhang, X.-F. Qiao, W. Shi, J.-B. Wu, D.-S. Jianga, and P.-H. Tan, Chemical Society Reviews **44** (2015).

[181] X. Zhang, S. Xiao, H. Nan, H. Mo, X. Wan, X. Gu, and K. K. Ostrikov, "Controllable one-step growth of bilayer MoS_2–WS_2/WS_2 heterostructures by chemical vapor deposition", Nanotechnology **29**, 455707 (2018).

[182] Y. Gong, J. Lin, X. Wang, G. Shi, S. Lei, Z. Lin, X. Zou, G. Ye, R. Vajtai, B. I. Yakobson, H. Terrones, M. Terrones, B. K. Tay, J. Lou, S. T. Pantelides, Z. Liu, W. Zhou, and P. M. Ajayan, "Vertical and in-plane heterostructures from WS_2/MoS_2 monolayers", Nature Materials **13**, 1135–1142 (2014).

[183] S. Tongay, W. Fan, J. Kang, J. Park, U. Koldemir, J. Suh, D. S. Narang, K. Liu, J. Ji, J. Li, R. Sinclair, and J. Wu, "Tuning interlayer coupling in large-area heterostructures with CVD-grown MoS_2 and WS_2 monolayers", Nano Letters **14** (2014).

[184] Y. Niu, S. Gonzalez-Abad, R. Frisenda, P. Marauhn, M. Drüppel, P. Gant, R. Schmidt, N. S. Taghavi, D. Barcons, A. J. Molina-Mendoza, S. M. De Vasconcellos, R. Bratschitsch, D. Perez De Lara, M. Rohlfing, and A. Castellanos-Gomez, "Thickness-dependent differential reflectance spectra of monolayer and few-layer MoS_2, $MoSe_2$, WS_2 and WSe_2", Nanomaterials **8** (2018).

[185] A. Berkdemir, H. R. Gutiérrez, A. R. Botello-Méndez, N. Perea-López, A. L. Elías, C.-I. Chia, B. Wang, V. H. Crespi, F. López-Urías, J.-C. Charlier, H. Terrones, and M. Terrones, "Identification of individual and few layers of WS_2 using Raman spectroscopy", Scientific Reports **3**, 1755 (2013).

[186] P. Rivera, J. R. Schaibley, A. M. Jones, J. S. Ross, S. Wu, G. Aivazian, P. Klement, K. Seyler, G. Clark, N. J. Ghimire, J. Yan, D. G. Mandrus, W. Yao, and X. Xu, "Observation of long-lived interlayer excitons in monolayer $MoSe_2$–WSe_2 heterostructures", Nature Communications **6**, 6242 (2015).

[187] M. Baranowski, A. Surrente, L. Klopotowski, J. M. Urban, N. Zhang, D. K. Maude, K. Wiwatowski, S. Mackowski, Y. C. Kung, D. Dumcenco, A. Kis, and P. Plochocka, "Probing the interlayer exciton physics in a $MoS_2/MoSe_2/MoS_2$ van der Waals heterostructure", Nano Letters **17**, 6360–6365 (2017).

[188] J. Zhang, L. Du, S. Feng, R.-W. Zhang, B. Cao, C. Zou, Y. Chen, M. Liao, B. Zhang, S. A. Yang, G. Zhang, and T. Yu, "Enhancing and controlling valley magnetic response in MoS_2/WS_2 heterostructures by all-optical route", Nature Communications **10** (2019).